Chapter 1

Introduction

X-ray was discovered by W. Röntgen in 1896 in the time that quantum mechanics was being developed. The properties of X-rays have been widely studied since then and main applications in material studies and medical examinations have been realized, largely due to its short wavelength and high penetration power. However, the development of X-ray sources on synchrotron accelerators in the 1970s has brought the X-ray science and technology into a new era. Based on the continuous characteristics of synchrotron radiation, an energy-tunable X-ray source was quickly applied in X-ray diffraction and X-ray absortion spectroscopy for atom-specific measurements.[1] With the synchrotron based X-ray techniques, complicate protein structures can be solved with sub-angstrom resolution and the chemical residues can be determined with ppm sensitivity in concentration.

Röntgen's first X-ray image, the image of Anna Bertha's hand, is the most famous event in X-ray history. Today, imaging with X-ray plays an irreplaceable role among all its applications because it is the most direct way for observing the object in real space. Furthermore, the X-ray imaging has made a significant progress in the last decade since the fabrication of X-ray lens, the zone plate, was greatly improved by the e-beam lithography technologies. Without the availability of zone plate, the resolution of X-ray image is limited around one micron by the crystal size of scintillator. However, with the zone plate the image can be magnified and the resolution is limited by the numerical aperture (NA) of zone plate. In couple with the improvement of the zone plate, the optical designs further improve the spatial resolution. For example, a resolution of 15 nm using soft X-rays by combining two zone plates has been demonstrated [2]. In our work, a resolution of 30nm using hard X-rays by utilizing the third diffraction order of a zone plate was achieved [3]. The computer tomography (CT) by X-rays was also demonstrated with 60nm resolution in three dimensional [4].

In the last ten years, a new generation of low emittance synchrotron facilities has been constructed which makes semi-coherent X-ray sources available. Even more powerful is the fourth-generation synchrotron source, X-ray free electron laser (X-FEL), is coming in place in the next few years in USA, Japan, and Germany which will provide coherent sources in the hard X-ray range. Using these new sources, the phase imaging in X-ray radiography and X-ray microscopy is becoming the focus in imaging science and techniques. The importance of phase imaging in X-ray region is

that the signal of the phase shift of wave can be increased by 2 to 3 order of magnitude from the absorption case as an intrinsic property of material. In consequence, the phase contrast method can greatly reduce the dose of X-rays in taking image. Thus, this method is the promising way for the observation of biology samples in vivo. In all aspects, the progress of X-ray imaging has been truly remarkable in last decade.

The phase contrast mechanism was mainly achieved by the Zernike phase contrast in the X-ray microscopy and defocus series image in X-ray radiography. The phase capability in the X-ray microscopy with partial coherent source has not been explored thoroughly before because of the rare availability of hard X-ray microscope and synchrotron source. The National Synchrotron Radiation Research Center of Taiwan had the first hard X-ray microscope installed on a hard X-ray beamline BL01B in September 2004 and the consequent commissioning of the microscope was quite successful to demonstrate a 60 nm spatial resolution. In this thesis, the capability of this X-ray microscope has been fully studied, along with the development of methods of phase retrieval by defocus series and Zernike phase contrast. The phase tomography is further studied to explore the technical limitations of phase imaging using hard X-rays.

The main focus of this thesis is the study of the phase imaging in the full-field type transmission X-ray microscope (TXM). In chapter 1, the background, the progress of phase imaging, the progress of TXM and the current issue of phase imaging are introduced. In chapter 2, NSRRC's TXM is introduced, including optical components, their functions, and the capabilities such as the energy tunability, third order image, dark field and tomography. In chapter 3, the two phase retrieval methods, transport of intensity equation (TIE) and self-consistent wave propagation (SCWP), are introduced. The pros and cons for the two phase retrieval algorithms are discussed and compared. A new approach by combining these two phase retrieval algorithms is presented, and the formulism of phase retrieval method in TXM is deduced with simulation and the experimental results. In chapter 4, Zernike phase contrast method is implemented in our experimental setup, which, in our view, is the most exciting achievement in this study. An algorithm to retrieve the pure phase information form Zernike phase contrast image is proposed. This method provides a way to the realization of the phase tomography as demonstrated experimentally. In chapter 5, conclusions and future work on the applications of TXM to the biology samples are discussed.

1.1 Matter, Light and their Interactions

1.1.1 The complex index of refraction of X-rays

The interaction of X-rays and matter can be described as wave absorption and phase retardation governed by the interaction of the electrons in the matter and electromagnetic wave. The details of the physical principle can be found in reference [5]. Here we give a brief review of the process and explain the optical parameter, the complex refraction index, which will be the base of our future discussions.

The expression for the total scattering cross section of a free electron, given by Thomas [6], is defined as the scattered powered divided by the input power,

$$\sigma_e = \frac{8\pi}{3} r_e^{\;2} \tag{1.1}$$

where r_e is the classical electron radius and σ_e is the cross-section of a free electron, which is independent of the energy of electromagnetic wave. The differential scattering cross-section for a free electron per unit solid angle can be obtained as following equation,

$$\frac{d\sigma_e}{d\Omega} = r_e^{\;2} \sin\Theta \tag{1.2}$$

Here Θ is the angle between the scattering vector and the plane of the incident wave front. We start with the equation of single electron moving in the electromagnetic field,

$$m\ddot{x} + m\gamma\dot{x} + m\omega_s^{\;2}x = -e(E_i + v \times B_i) \tag{1.3}$$

where m is the mass of electron, γ is the damping factor, $\omega_s^{\;2}$ is the spring constant of restoring force which has the resonant frequency ω_s. The right hand side of the equation is the Lorentz force. For the multi-electron atom one can apply the same equation but E field with different phase for each electron. Thus, the electric field of single component E_i can be rewritten as:

$$E_i(r,t) = E_i e^{-i(\omega t - k_i \cdot \Delta r_s)} \tag{1.4}$$

The equation can be solved as the following.

$$x_s(t) = \frac{1}{\omega^2 - \omega_s^{\;2} + i\gamma\omega} \frac{e}{m} E_i e^{-i(\omega t - k_i \cdot \Delta r_s)} \tag{1.5}$$

$$a_s(t) = \frac{-\omega^2}{\omega^2 - \omega_s^{\;2} + i\gamma\omega} \frac{e}{m} E_i e^{-i(\omega t - k_i \cdot \Delta r_s)} \tag{1.6}$$

3

where k_i is the wave vector and Δr_s is the position of the i electron. The scattered electrical field from a multi- electron atom can then be written as

$$E(r,t) = \frac{e}{4\pi\varepsilon_0 c^2} \sum_{s=1}^{Z} \frac{a_{t,s}(t - r_s/c)}{r_s} \tag{1.7}$$

Combine (1.7) and (1.6), and assign $a_T = a\sin\Theta$, we have

$$E(r,t) = \frac{-e^2}{4\pi\varepsilon_0 mc^2} \sum_{s=1}^{Z} \frac{\omega^2 E_i \sin\Theta}{\omega^2 - \omega_s^2 + i\gamma\omega} \frac{1}{r_s} e^{-i[\omega(t-rs/c)-k_i \cdot \Delta r_s]} \tag{1.8}$$

After some approximation and rearrangement, we obtain

$$E(r,t) = \frac{-r_e E_i \sin\Theta f(\Delta k,\omega)}{r} e^{-i\omega(t-rs/c)} \tag{1.9}$$

where the $f(\Delta k,\omega)$ is the *complex atomic scattering factor*, written as

$$f(\Delta k,\omega) = \sum_{s=1}^{Z} \frac{\omega^2 e^{-u\Delta k \cdot \Delta r_s}}{\omega^2 - \omega_s^2 + i\gamma\omega} \tag{1.10}$$

In the same definition that derived (1.1) and (1.2), for a multi-electron atom the scattering factor becomes

$$\sigma_e(\omega) = \frac{8\pi}{3} r_e^2 |f|^2 \tag{1.11}$$

$$\frac{d\sigma_e(\omega)}{d\Omega} = r_e^2 |f|^2 \sin\Theta \tag{1.12}$$

In (1.10) becasue $|\Delta k \cdot \Delta r_s|$ is small for the wavelength larger than the hydrogen atom radius (0.529Å) or the forward scattering dominates, the *complex atomic scattering factor* is further simplified to (1.13). Here we introduce the oscillator strength g_s for the electron associated with a given resonance ω_s. The atomic scattering factor can be written as (1.13).

$$f^0(\omega) = \sum_{s=1}^{Z} \frac{g_s \omega^2}{\omega^2 - \omega_s^2 + i\gamma\omega} \tag{1.13}$$

The Thomas-Reiche-Kuhn sum rule states that the sum over all the oscillator strength must come out to be equal to the total number of electrons in the atom. Which is a approximation to use the transition probability g_{kn}. Here, we have scattering factor is proportional the Z square.

$$\sum_{s=1}^{Z} g_{kn} = Z \tag{1.14}$$

For the purpose of describing the propagation of a wave field in a medium, we decompose the complex atomic scattering factor into its real and imaginary parts:

$$f^0(\omega) = f_1^0(\omega) - if_2^0(\omega) \tag{1.15}$$

We start from solving the wave equation after the E field is known in (1.9), recall that the wave equation.

$$\left(\frac{\partial^2}{\partial t^2} - \frac{1}{\mu_0 \varepsilon_0} \nabla^2\right) E_T(r,t) = \frac{-1}{\varepsilon_0}\left[\frac{\partial J_T(r,t)}{\partial t}\right] \tag{1.16}$$

With the assumption that the current density is contributed equally for all similar atoms, we have the current density can be expressed as the following,

$$J_0(r,t) = -en_a \sum_s g_s v_s(r,t) \tag{1.17}$$

where n_a is the average density of atoms, and the v_s can be obtained as (1.6) and (1.7).

$$v_s(t) = \frac{1}{\omega^2 - \omega_s^2 + i\gamma\omega} \frac{e}{m} \frac{\partial E(r,t)}{\partial t} \tag{1.18}$$

After combining (1.18), (1.17) and (1.16), we have

$$\left[\left(1 - \frac{e^2 n_a}{\varepsilon_0 m}\sum \frac{g_s}{\omega^2 - \omega_s^2 + i\gamma\omega}\right)\frac{\partial^2}{\partial t^2} - \frac{1}{\mu_0 \varepsilon_0}\nabla^2\right] E_T(r,t) = 0 \tag{1.19}$$

Compare to the standard form of the wave equation:

$$\left[n^2(\omega)\frac{\partial^2}{\partial t^2} - \frac{1}{\mu_0 \varepsilon_0}\nabla^2\right] E_T(r,t) = 0 \tag{1.20}$$

We have the n(ω) as

$$n(\omega) \equiv \left(1 - \frac{e^2 n_a}{\varepsilon_0 m}\sum \frac{g_s}{\omega^2 - \omega_s^2 + i\gamma\omega}\right)^{1/2} \tag{1.21}$$

For ω^2 is large compared to $\dfrac{e^2 n_a}{\varepsilon_0 m}$, the equation can be approximated as

$$n(\omega) \equiv 1 - \frac{1}{2}\frac{e^2 n_a}{\varepsilon_0 m}\sum \frac{g_s}{\omega^2 - \omega_s^2 + i\gamma\omega} \tag{1.22}$$

After substituting (1.15) into (1.22) and with $r_e = \dfrac{e^2}{4\pi\varepsilon_0 mc^2}$

$$n(\omega) = 1 - \frac{2\pi c^2 n_a r_e}{\omega^2}(f_1^0(\omega) - if_2^0(\omega)) = 1 - \frac{n_a r_e \lambda^2}{2\pi}(f_1^0(\omega) - if_2^0(\omega)) \tag{1.23}$$

Compare to the customary way for reflection index in X-ray:

$$n(\omega) = 1 - \delta + i\beta \qquad (1.24)$$

where δ and β is the reflection index in real and imaginary part. We have the δ and β in the following terms.

$$\delta = \frac{n_a r_e \lambda^2}{2\pi} f_1^0(\omega) \qquad (1.25)$$

$$\beta = \frac{n_a r_e \lambda^2}{2\pi} f_2^0(\omega) \qquad (1.26)$$

1.1.2 The absorption and phase shift

The wave propagation can be written for the temporally stationary case:

$$E(r,t) = E_0 e^{-i(\omega t - kr)} \qquad (1.27)$$

where k is the wave vector,

$$k = k_0 n(\omega) = k_0(1 - \delta + i\beta) \qquad (1.28)$$

with k_0 the wave vector in vacuum. Thus, (1.27) becomes

$$E(r,t) = E_0 e^{-i(\omega t - k_0 r)} e^{i(k_0 \delta)r} e^{-(k_0 \beta)r} \qquad (1.29)$$

The first term is original wave in the vacuum, and the following terms are due to the phase retardation and absorption of wave in the medium. The intensity of wave can be express as

$$I(r,t) = E(r,t)E^*(r,t) = E_0^2 e^{-(2k_0 \beta)r} \qquad (1.30)$$

The amount of the phase retardation is given by

$$k_0 \delta r = \frac{2\pi\delta r}{\lambda} \qquad (1.31)$$

The amount of absorption is given as follow

$$1 - \exp(-2k_0\beta r) = 1 - \exp(-\frac{4\pi\beta r}{\lambda}) \qquad (1.32)$$

In the macroscopic view (hundreds of atoms), the interaction of X-rays and matter is suitably described by these two parameters β and δ. This approach is valid for wavelength larger than radius of hydrogen atom or for the case that the forward scattering dominates.

1.1.3 The free space wave equation

The basic transportation of the wave in free space was known by Christiaan

Huygens in seventeen century. This well known formula is called the Huygens principle or Huygens–Fresnel principle [7], which recognizes that each point of an advancing wave front is in fact the center of a fresh disturbance and the source of a new train of waves; and that the advancing wave as a whole may be regarded as the sum of all the secondary waves arising from points in the medium already traversed. In the mathematic from, this can be written as:

$$\psi(P_0) = \frac{1}{i\lambda} \iint_C \psi(P_1) \frac{\exp(ikr_{01}\pi)}{r_{01}} \cos\theta \, ds \qquad (1.33)$$

where ψ is the wave in space as function of a three dimensional points, P_0 and P. In equation (1.33), the wave at point P_0 can be calculated by summing the all wave vectors from surface C, the close surface which encloses the point P_0.

In principle, the wave transportation can be calculated by the above integration; however, it is not realistic to calculate an image in a point-by-point integration even using the processing power of today's computer. The approximation for calculation was then introduced by Fresnel as shown in equation (1.34). The Huygens–Fresnel principle is further simplified while the paraxial approximation is applied.

$$\psi(x,y,z_2) = \frac{i\exp(-2\pi i z_{12}/\lambda)}{\lambda z_{12}} \iint \psi(X,Y,z_1) \exp\{-\frac{i\pi}{\lambda z_{12}}[(x-X)^2 + (y-Y)^2]\} dX dY$$

$$(1.34)$$

The notation is changed from P to Cartesian coordinate (x,y,z) and the spherical secondary wavelets of the Huygens-Fresnel principle have been replaced by wavelets with parabolic wavefronts. In this way, the image can be calculated with the convolution theorem as written in equation (1.35).

$$\psi(x,y,z) = A\psi(X,Y,0) \otimes \exp\{-\frac{i\pi}{\lambda z}[X^2 + Y^2]\} \qquad (1.35)$$

where $\exp\{-\frac{i\pi}{\lambda z}[X^2 + Y^2]\}$ is the propagator in real space. Thus, the propagation of wave can be simulated by Fast Fourier Transform (FFT) in the computer.

The transportation of wave involves not only the intensity but also the phase of the wave from one plane to the other. It is the phase information to be applied for obtaining phase imaging, which will be introduced in the later sections.

1.2 The X-ray Phase Imaging – a literature survey

The phase of a wave can not be seen directly. Actually, the phase considering here stands for the wave front, and the phase imaging is a technique to reveal the wave front in the image. The phase of the wave is relative, but not an absolute value. Its unit is in radian. The phase imaging is a map of the wave front in two or three dimensions.

In 1972, Gerchberg and Saxton proposed the first phase retrieval algorithm describing an iterative method to solve the phase from image and diffraction plane [8]. Fienup proposed a similar way to solve the phase by only the information of diffraction plane with constrains of the known support [9]. The two methods are both utilized in transmission electron microscope (TEM), from which the diffraction image and image of real space both can be easily acquired.

The direct way of solving the phase information in real space was not realized until M. R. Teague proposed the first solution of the transport of intensity equation (TIE) in 1983 [10]. The studies of TIE were then followed by Gureyev, Roberts, and Nugent. [11], proving that the uniqueness of the solution of TIE only if the intensity is non-zero. The X-ray phase image experiment was then estimated by the K. A. Nugent in 1996 [12] with the phase retrieval by using a scanning type X-ray microscope. The experiment of TIE was applied to visible light by A. Barty, et al. in 1998 [13]. The first phase tomography with spatial resolution of several microns was achieved by P. Cloetens, et al. at ESRF in 1999 [14]. Numerous theorems and experiments of TIE were followed since then [10-13]. Another iterative methods of phase retrieval were proposed [14,15] for TEM and TXM and these methods are good for the phase recovery of small object (high spatial frequency). This kind of methods does not have a unified name. We call it the self-consistent wave propagation (SCWP), which will be explained in chapter 3.

In the past two decades, the X-ray phase imaging has been an interesting problem as the theorem and the coherent sources both have made substantial progresses. The phase retrieval for low resolution image by X-rays [16] and that for high resolution image by electrons were demonstrated [15]. What has not been shown until now is the X-ray phase imaging with high resolution. Using the new nano resolution X-ray microscope installed at NSRRC, the phase imaging is explored as a major part of the thesis research.

1.3 The Progress of X-ray Microscope

As the availability of synchrotron light sources increases in last two decades, many types of synchrotron based microscopes have been developed. The photon-in and photon-out X-ray microscope can be roughly divided into two categories: the full field type transmission X-ray microscope (TXM) and scanning transmission X-ray microscope (STXM). Other types of X-ray microscopes include the X-ray scanning photoelectron microscope (SPEM) [17] and photo electron emission microscope (PEEM) [18], which are based on photon-in and electron-out process.

A TXM requires optics to magnify the image or beam spot. Until now, there are mainly two kinds of X-ray lenses which can successfully magnify the images; they are zone plate (ZP) [19-23] and compound refractive lens (CRL) [24]. These optical elements are possibly made due to the advance in nanofabrication technologies. At present, the CRL still surfers from low transmission, spherical aberration, and optical distortions. However, the CRL has an advantage in high energy focusing which can be as high as 27 keV [25]. However, the CRL based microscope can only reach a resolution up to 400nm in image and tomography [26]. On the other hand, the ZP based microscope has shown resolution less than 100nm at 11 keV. [4] The ZP requires high aspect ratio for the outmost zone, which currently can be reached around 25 by a double stack zone plate [27]. Recently, the CRL fabricated by the micro-machining process is demonstrated and the shape of hyperbolic type is shown [28], which can be the candidates for future X-ray microscope.

The Fresnel zone plate is well known as a diffractive optics. It was first used to focus X-rays in the soft X-ray region using STXM by J. Kirz [22,29] and using TXM by G. Schmahl [21]. The highest resolution of TXM in the soft X-ray region is 15nm [2] and the STXM reaches the resolution up to 20nm. In the hard X-ray region, our TXM at NSRRC has shown 30nm resolution [3]. Over all, the ZP based microscopes dominate the present field of X-ray microscopy because of better resolution and aberration control of image. More details will be presented in chapter 2.
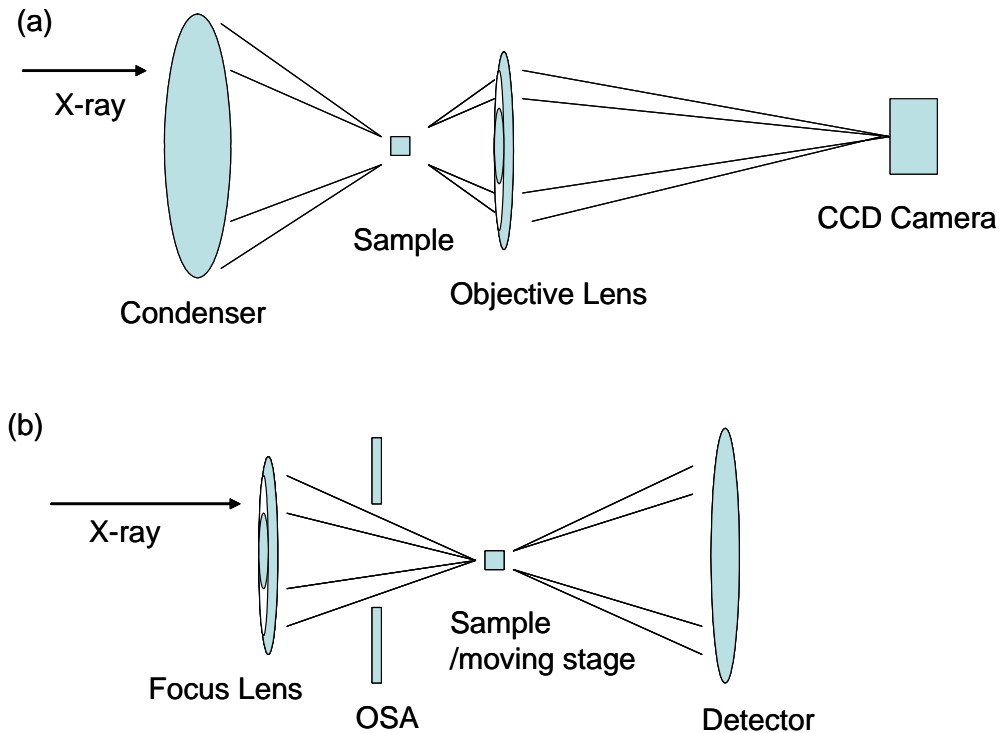
Figure 1-1 The schematic view of (a) TXM and (b) STXM. The TXM is mainly composed of the condenser, objective lens and a 2D detector. (It usually is a CCD camera) The STXM is composed of the objective lens, an order sorting aperture (OSA), a moving stage and detector. (The detector usually is a diode or segmented detector.)

There are several major differences between the TXM and STXM as shown in figure 1-1. First, the objective lens is put in back of the sample in TXM and is in the front of the sample in STXM. Second, TXM usually has higher spatial resolution than the STXM. Although the resolution of TXM and STXM are both limited by the width of outer most zones, the requirement of beam quality is different. For TXM, each point on the sample can be taken as an independent source, thus, the resolution depends on the illumination condition. The resolution is therefore enhanced by partial coherent illumination in TXM. However, for STXM, the condition is much strict; to get a diffraction-limited spot requires a perfect spatial coherent source. Most X-ray sources are spatially incoherent.

From user points of view, another important difference is the dose limit. STXM can have about 10 times higher efficiency than TXM. Experimentally, the zone plate has only about 10% diffraction efficiency [20-23]. Under the same condition, the STXM has higher efficiency for collecting the photons after the sample and therefore requires less dose in STXM than in TXM.

1.4 Current Issue - towards living cell tomography

Hard X-ray microscopes offer the advantages of high penetration and high resolution which set between the optical microscope and electron microscope. Thus, one of the important applications is the biological imaging because of the dual merits of penetration and resolution, which makes three dimensional in vivo study possible.

We simulated the possibility of using X-ray microscope to observe a live cell. A biological cell is packed in a water-filled micro tube as depicted as figure 1-2(a). The biological cell is in the middle of a micro-tube with diameter of 15μm. The cell is filled with water, cell organ, and nucleus. The parameters used for the simulation are tabulated in the table 1-1. The X-ray energy in the simulation is 8 keV.

Table 1-1. The parameters for a simulated study of biology sample in the micro-tube.

Item name	Material	δ	β
Micro Tube shell	SiO_2	1.23×10^{-5}	1.2×10^{-8}
Cell outer shell	Air	0	0
Cell inner shell	Ice/water	4.1×10^{-6}	4.0×10^{-9}
Sub-cell Organ	organic	4.6×10^{-6}	4.56×10^{-9}
Nucleus	organic	4.6×10^{-6}	4.56×10^{-9}

The images of 1-2 (b) to (d) show the projection images with the white noise on the detector from 0 to 1%. The count of projection image is normalized to 1; the highest count for display of the projection image is 1 and the lowest count for display is 0.98. The figure (b) indicates that the projection of the cell with zero noise by the absorption contrast (which mainly depends on β). We can see that the contrast is very poor. If the noise in the detector is around 1% or more, it is hard to observe the absorption contrast, as shown in the figure 1-2(c) and (d) which are the simulated image by 0.1% of noise and 1% of noise, respectively.
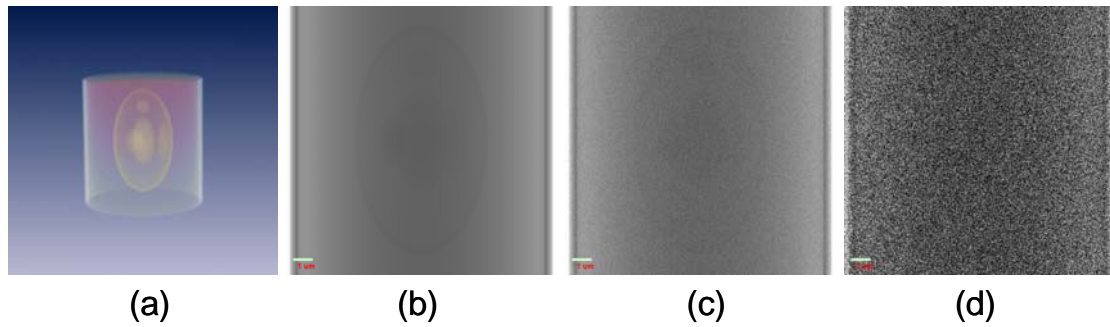
| (a) | (b) | (c) | (d) |

Figure 1-2 The simulated projection images of a cell in the micro-tube. (a) the artistic view of the cell in the micro cell (b) the projection image of pure absorption contrast with no noise (c) pure absorption with 0.1% root-mean-squared (RMS) noise (d) with 1% noise.

In table 1-1 we note that the nature of the most material has larger δ than β. So the phase contrast will largely enhance the image of biological object. In the hard X-ray region, the ratio for δ/β is generally 100 to 1000, which means that the phase contrast is 100 to 1000 times larger than the absorption contrast. It also means that the radiation damage can be 100 to 1000 times less than the absorption contrast, as shown in figure 1-3. The phase contrast (dash line) allows lower minimum dose than the absorption contrast by a factor of 10^5; this is mainly because the dose is not only proportional to flux, but also proportional to photon energy. This explains why the phase contrast becomes important in the X-ray microscope. The details of how to obtain the phase images will be described in chapter 3 and chapter 4.
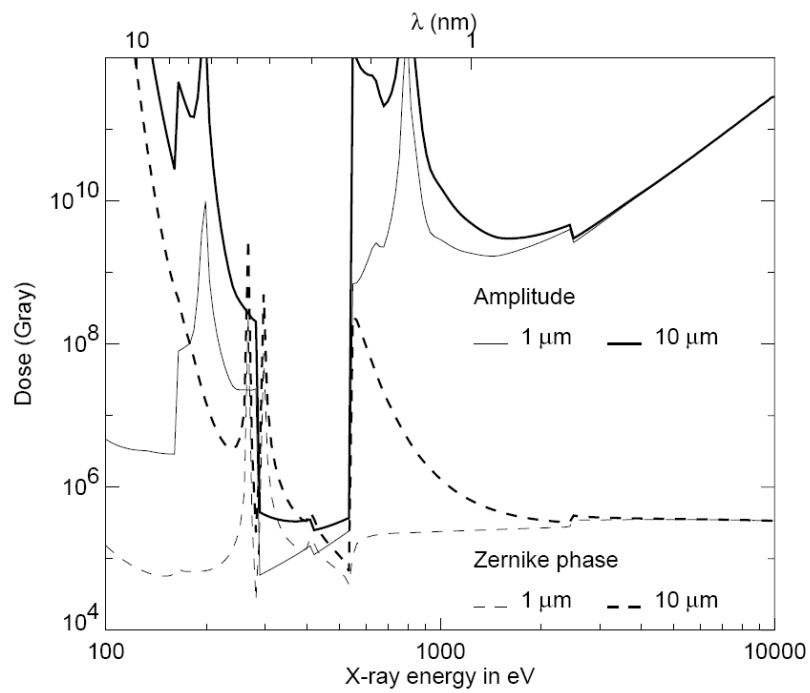
Figure 1-3 Radiation dose calculated for minimal exposure imaging (signal:noise=5:1) of 50 nm protein structures in 1 and 10 μm thick ice layers (ρ= 0:92). Both amplitude (solid lines) and Zernike phase contrast (dash line) cases (3π/2 phase plate with no absorption) are shown. (Courtesy of Janos Kirz etal.)
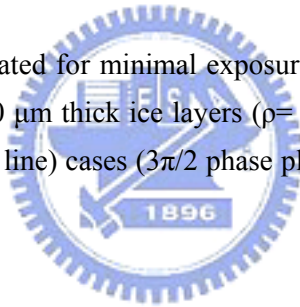
Chapter 2

Transmission X-ray Microscope at NSRRC

The NSRRC's TXM was planned to be the main end station of a newly installed X-ray source of superconducting wavelength shifter at the Taiwan Light Source. Through a collaborative design work, the TXM was fabricated by Xradia and installed in September 2004, which was the first zone plate based hard X-ray microscope on a synchrotron beamline operated at 8-11 keV. Soon after a spatial resolution of 60 nm was demonstrated [1]. In this chapter, the components, optical principles and capabilities of the TXM are introduced in the following sections.

2.1 Storage Ring and Superconducting Wavelength Shifter

The Taiwan Light Source (TLS) is a 1.5 GeV synchrotron which was commissioned in October 1993 as the first third generation synchrotron in Asia. In order to enhance the hard X-ray intensity, the superconducting wavelength shifter (SWLS) was developed with three pairs of racetrack superconducting coils to generate a maximum magnetic field of 5 Tesla at the central pole. This insertion device was installed at the downstream of the straight section for beam injection. The beamline BL01B [2] is equipped with a toroidal focusing mirror and a double crystal monochromator using two Ge(111) crystals. The beamline provides monochromatic photon beams with energies tunable from 5 keV to 20 keV with an expected photon flux about 7×10^{11} photons/sec/200mA with an average energy resolution ($\Delta E/E$) of 1 $\times 10^{-3}$ The beam spot at is about 1 mm $\times$ 0.3 mm at the end of the beamline. An average photon flux of 5×10^{11} photons/sec/300mA has been measured. The optical layout and the measured flux of BL01 are shown in the figure 2-1 and figure 2-2.
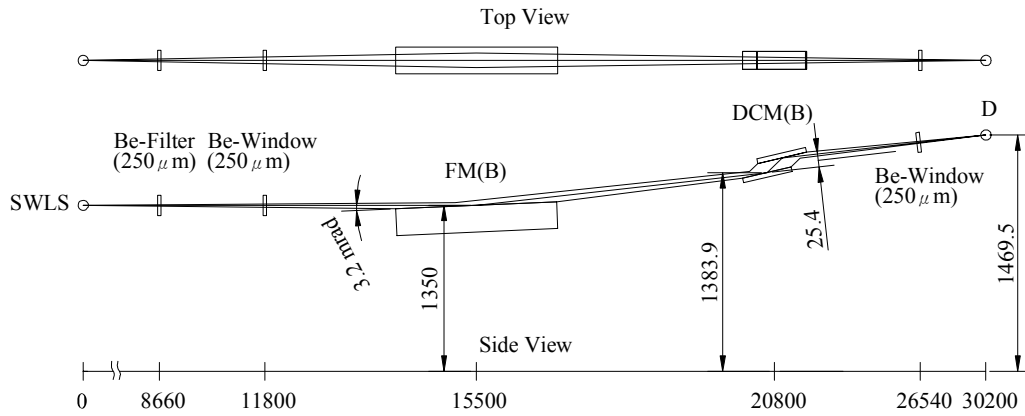
Figure 2-1 The optical layout of BL01B. The beamline is consisted of two optical components. One is the focusing mirror (FM(B)), and another is double crystal monochromator (DCM). The numbers written below are the distance from the source, the unit is mm.
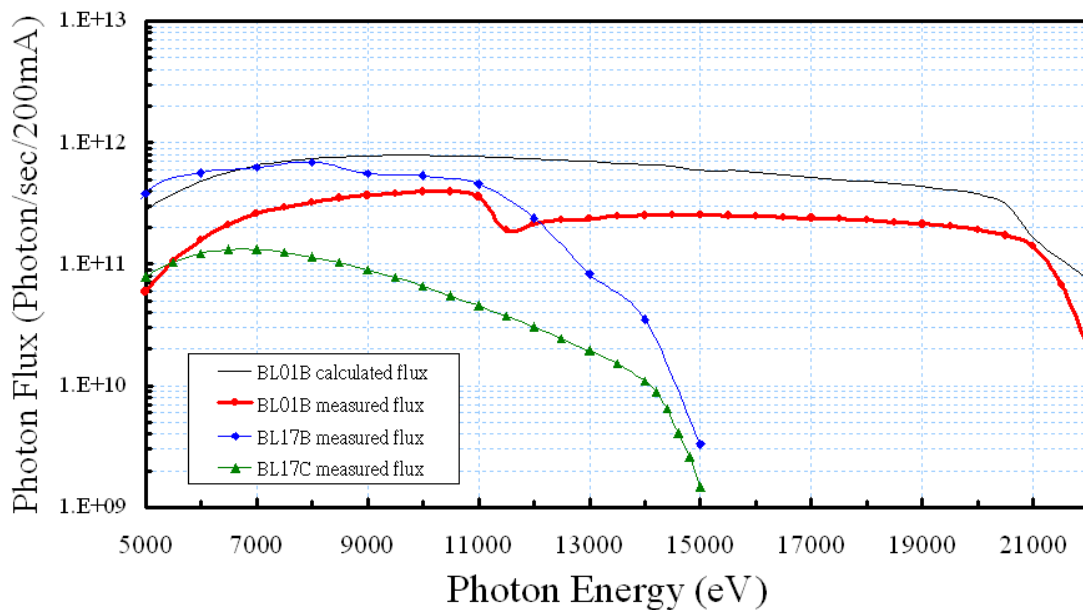

Figure 2-2 The spectrum of measured flux for BL01B (SWLS), BL17B (wiggler) and BL17C (wiggler).

The beamline of BL01B is designed as a flux-rich and medium spectrum resolution. Optically, only one focusing mirror was used for focusing the spot on the sample, and with the double crystal monochromator (DCM) of Ge (111), which gives the resolving power up to 1000. This beamline is about 30 meters long from the front end to the end station. The spectrum of flux is shown in the figure 2-2. For the old beamline, BL17C and BL01B, which have the flux decreasing dramatically after 11

keV. This is a clear comparison between the superconducting wavelength shifter (SWLS) and wiggler.

2.2 NSRRC's TXM

The development of high resolution transmission x-ray microscope (TXM) has been actively pursued since synchrotron sources became available. The zone plate based TXM has already achieved a spatial resolution of 15 nm when it is operated in the soft x-ray region (100 eV – 1 keV) [3]. However, such a resolution has been a big challenge in the hard x-ray region due to the difficulty of zone plate fabrication [4].

The TXM in NSRRC was first considered for the hard X-ray region. The design and construction of the microscope was done in September 2004 under collaboration between NSRRC and Xradia Inc. [6]. When the TXM was commissioned, it had demonstrated a resolution of 60 nm in the energy range of 8 to 11 keV, the highest spatial resolution in the world at that time [1,5].

The optical layout

The TXM system consists mainly of several optical components: the condenser, the zone plate, the scintillator and detector unit. The schematic of the TXM is shown in figure 2-3 and the real system in figure 2-4. The optical components will be described in the following.
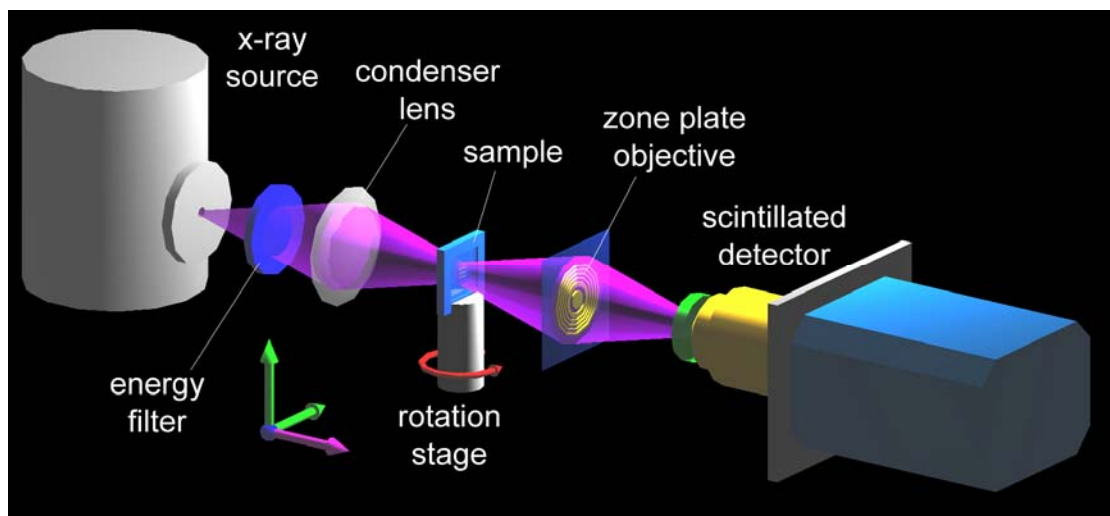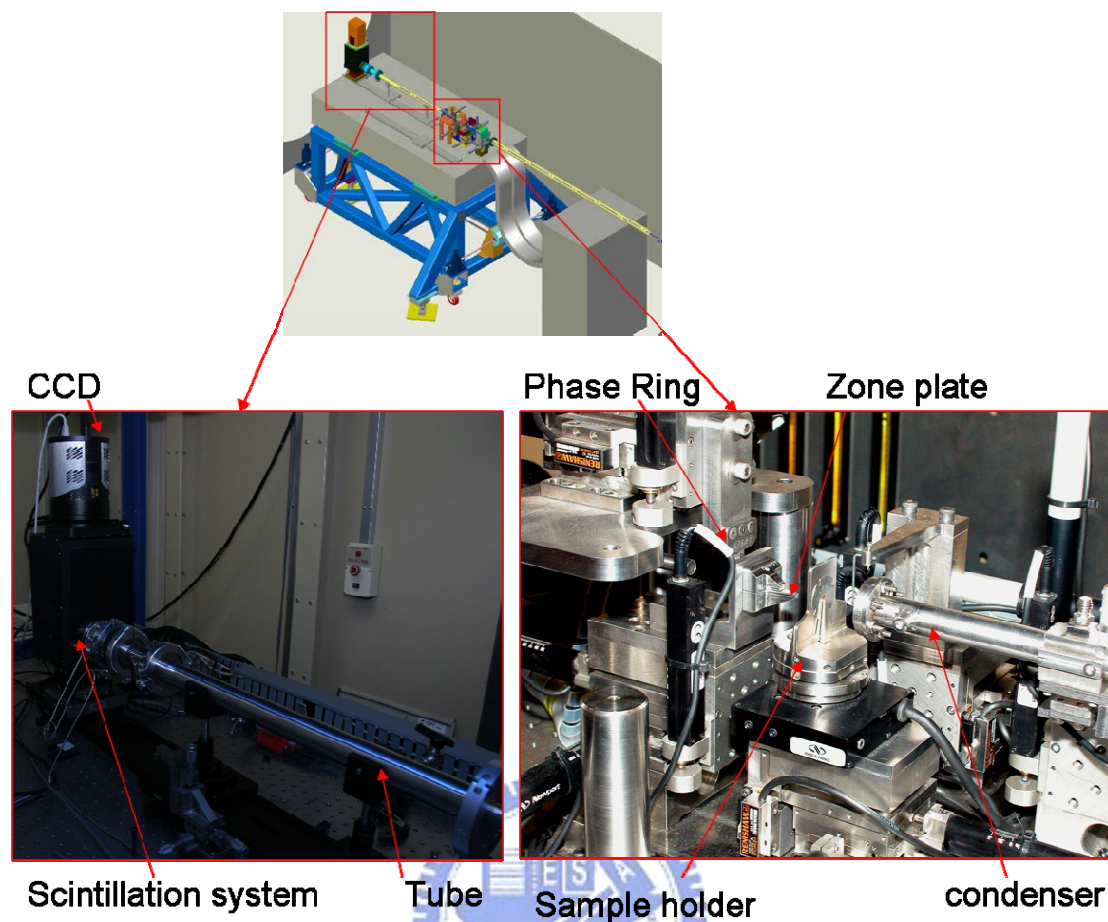

Figure 2-3 The schematic drawing of the TXM.

Figure 2-4 The images of TXM in BL01B hutch.

The X-rays, after the focusing mirror and Ge (111) double crystal monochromator, are further shaped by a capillary condenser. The condenser is circularly symmetric single reflection glass capillary whose profile is custom made according to the characteristic of the incident beam. The capillary has a length of 15 cm with its entrance aperture about 300 μm and an end opening about 200 μm in diameter. The estimated reflection angle is 0.5 mrad respect to the beam propagation direction. The measured reflection angle from the condenser is from 0.87 mrad to 1.13 mrad. A gold bead of 100 μm is attached at the end of the condenser so that a hollow cone beam of illumination is generated. The beam is focused at the sample position. The zone plate is placed downstream at its focus length, 27 mm in this case, and the zone plate of 75 to 85 μm diameter is well illuminated by the cone beam from the capillary condenser.

Due to difference of emittance of synchrotron source in horizontal and vertical directions, the synchrotron source has an elliptical shape with its major axis in the horizontal direction. It is hard to balance the vertical and horizontal illumination. The

way we use to match the source is only to adjust the beam line so that the position of vertical and horizontal focus are at the same position after the condenser for optimizing the flux.

The optical system of the microscope is composed of capillary condensers, a sample manipulation/positioning system, objective zone plates, and a scintillator, a 20X objective, and a composite CCD imaging system. With the high brilliance SWLS source, the microscope has the detector counts about 100 counts/pixel/sec, where each pixel corresponds to 16 nm on its side at the object plane.

Condenser

The condenser is made of a single reflection capillary [7,8]. The total internal refection gives the reflection up to 90% for 8 keV at 0.5 mrad as shown in the figure 2-5. For a condenser which is made of the single reflection of glass, the limitation of the critical angle is about 4 mrad for the roughness is about 10 nm. The shape of the capillary is hyperbolic type and made by the capillary puller in Xradia Inc. The optical layout of the condenser is shown as the figure 2-6, and the out look of the condenser is shown as the figure 2-7. Currently, there are all three condensers in this microscope, they are absorption condenser, phase condenser, and third order condenser. They are developed for different usages, the phase contrast and the third order, which is described in the later sections.

The foot print of the x-ray beam is about 1mm × 0.3 mm (horizontal × vertical) on the entrance of the condenser. The entrance of the condenser is about 0.3mm which is well fitted in the vertical but loss flux in the horizontal.
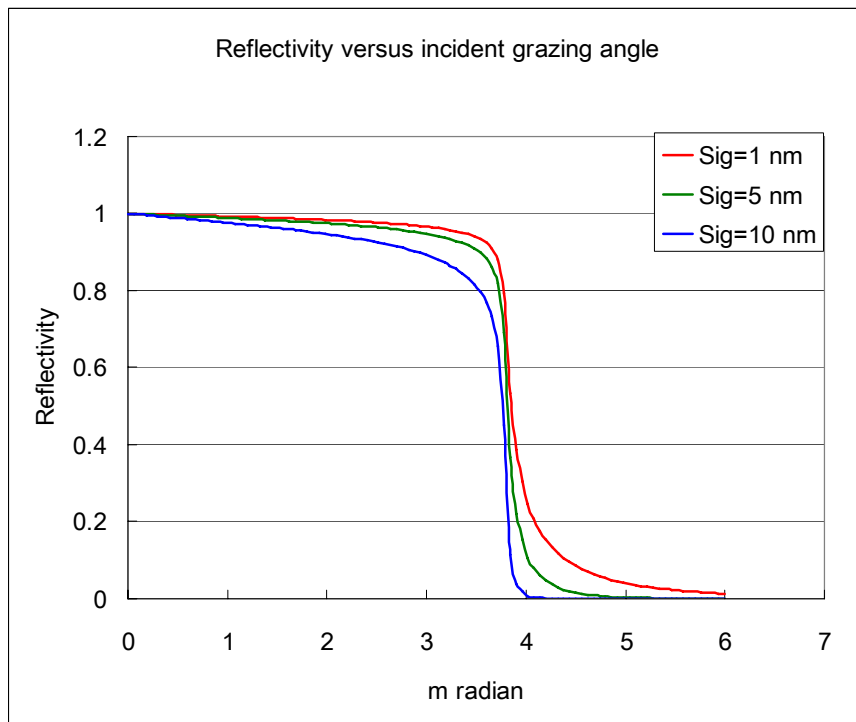
Figure 2-5 The reflectivity versus incident grazing angle for the glass (SiO_2) capillary for photon energy of 8 keV. The red, green and blue lines are for the roughness (Sig.=Sigma) of 1 nm, 5nm and 10nm. (Data from CXRO, center of x-ray optics)
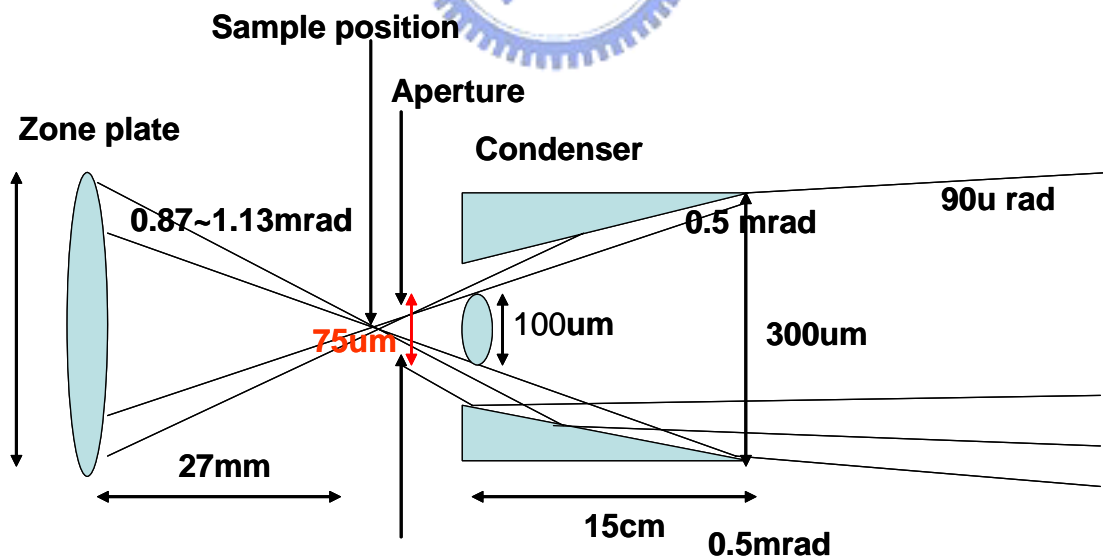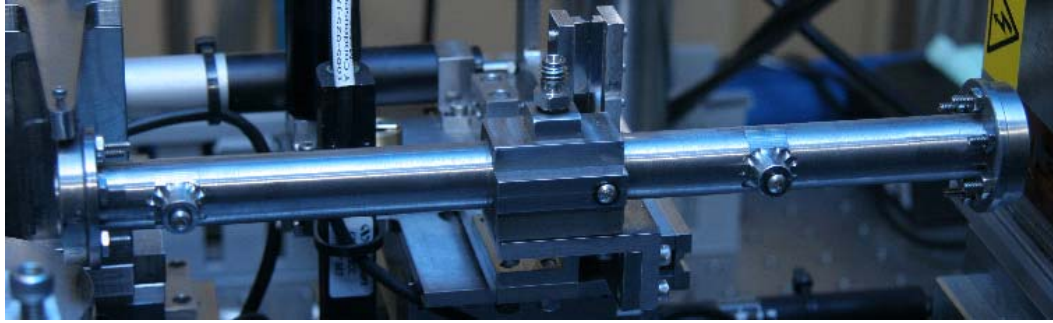

Figure 2-6 The optical layout of the condenser.

(a)

(b)

Figure 2-7 The capillary condenser use to focus X-ray. (a) the metal shell of the condenser (b) the glass capillary condenser.

Zone plate

Fresnel zone plate has a resolution up to diffraction-limited resolution [9,10],

$$\delta_m = 1.22 \frac{dr}{m} \qquad\qquad (2.\ 1)$$

where dr is the outermost zone width and m is the diffraction order of the zone plate. The zone plate used in this study is made of gold by electroplating on the silicon nitride membrane. Using a zone plate with a 50 nm outermost zone width, we should be able to achieve 60 nm spatial resolution if the mechanical and thermal stability is well engineered. However, the thickness of gold has to be about 890nm to achieve a phase shift of $\pi/2$ in the hard X-ray region of our interest. To fabricate a zone plate of such a high aspect ratio (~18) remains to be a big challenge in nano fabrication.

However, manufacturing a zone plate for operating in hard x-ray region is significantly challenge because a very high aspect ratio (defined as the ratio of the thickness to the zone width) for the outer most zones is required. For example, to achieve spatial resolution of 60 nm at 8 keV, the zone plate which made of gold requires that the width of outmost zone is smaller than 50 nm. The optimized thickness of zone plate is about 1.8 μm to reach the phase shift of π at 8 keV. The aspect ratio of outmost zone of zone plate is, therefore, about 36. However, the current achievable aspect ratio for gold zone plate is about 18 when the TXM is installed. Apparently, the required ideal aspect ratio for a 50 nm zone plate is far beyond the current fabrication capability. (At the time of writing, the aspect ratio is already 25) [11].

A typical image of the zone plate used in this study is shown in the figure 2-8. The measured efficiency of first order diffraction is above 10%. Three zone plates are used for adapting different energies from 8 keV to 11 keV, which will be discussed later.

The image properties of the TXM mostly depend on the quality of the zone plate. The principle of image in TXM can be taken as one magnification by thin lens. The details of the principle will be discussed in chapter 3.
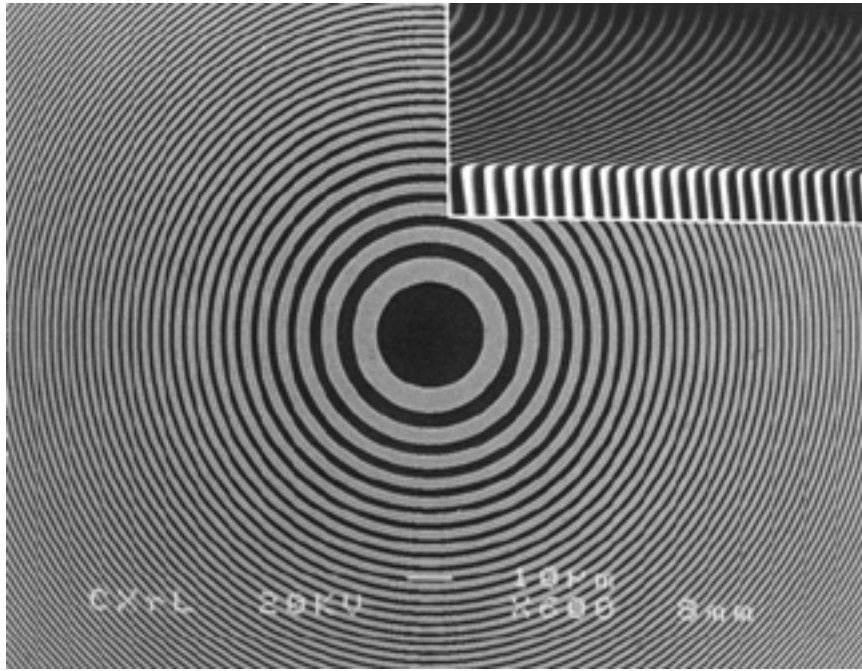
Figure 2-8 The SEM image of zone plate. The intersection shows the high aspect ratio of ~18.

Scintillator & CCD detector system

The scintillator converges x-ray to the visible light. The key issue for the scintillator is resolution (corresponding to the grain size of scintillator) and the efficiency. The scintillator is made of CsI with the quantum efficiency up to 40% at 8 keV[6]. A visible-light objective lens is placed after the scintillator to magnify the image on the scintillator, and a mirror with 45 degree is placed to reflect the image on to a CCD, which a prevention from x-ray striking on the CCD. The CCD is PIXIS 1024, which has 1024×1024 pixels with a fast readout rate of 20 MBit/second, made by Princeton Instrumentation. Figure 2-9 shows the real system and the optical layout.
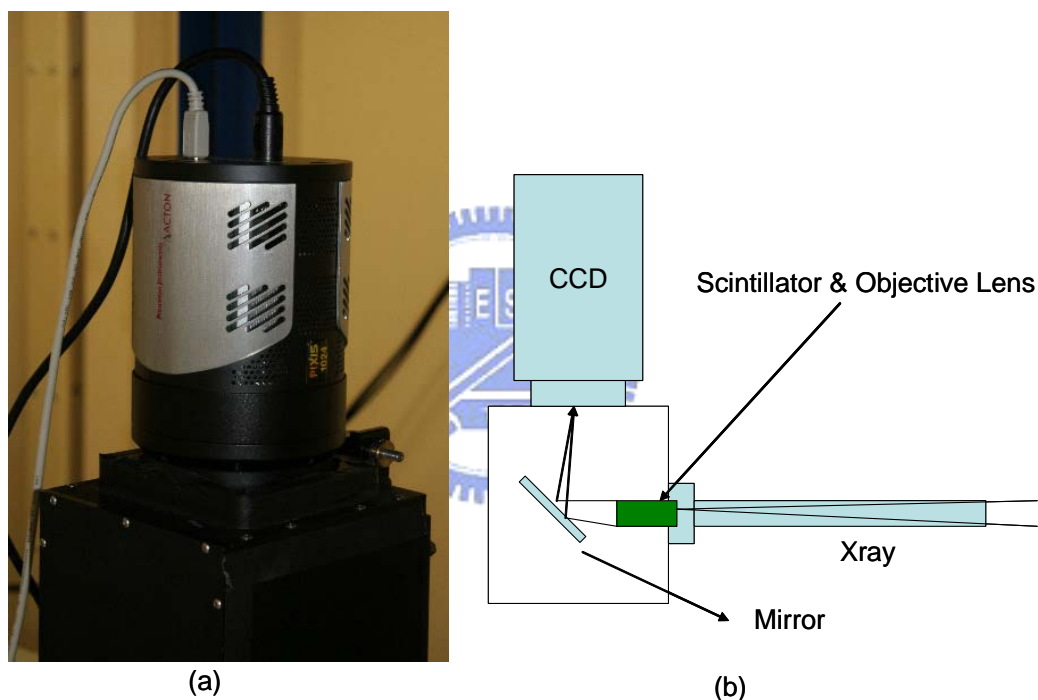

(a)   (b)

Figure 2-9 (a) The CCD ,(b) the schematic of the internal design of the microscope.

The whole system of the microscope is composed of capillary condensers, a sample manipulation/positioning system, an objective zone plates, a scintillator, a 20X objective, and a composite CCD imaging system. Using BL01B beamline with the SWLS source, the microscope obtains the detector counts about 100 counts/pixel/sec, where each pixel corresponds to 16 nm on its side at the object plane.

2.3 Absorption Contrast Image

Element-specific contrast imaging

For a TXM with an energy tunable source, it is possible to obtain image of specific element by scanning through its absorption edge. To implement this function, three zone plates of different diameter are used in the TXM to accommodate the change of focus distance with different energy. Following the formula of the focal length, $f=2rdr/\lambda$, where "f" is the focal length, the "r" is the radius of the zone plate, "dr" is the width of the outmost zone of the zone plate and "λ" is the wave length of the incident wave, these zone plates with different diameters are made as listed below.

Table 2-1 Specification of the three zone plates in NSRRC's TXM

Diameter (μm)	85	75	70
Fit Energy (keV)	8.5	9.5	10.5
Focus length (mm)	29.2	28.8	29.6

Since their focus lengths are designed as almost the same (around 3cm), the magnification of the microscope is given by dividing the image distance by objective distance then times the magnification of the optical lens in front of the CCD, which is 20 in our case. The value of magnification is 780 to 880 in 8 to 11 keV range, having about 12% variations for different energies, as shown in figure 2-10. With this design, the sample can be imaged by different energies with reasonably close magnification if two energies are chosen correctly. For 100 eV energy difference, the variation of magnification is about 1%. Therefore, it is possible to have almost the same magnification with different energies by using two different zone plates. In this way, the element-specific contrast image can be obtained.
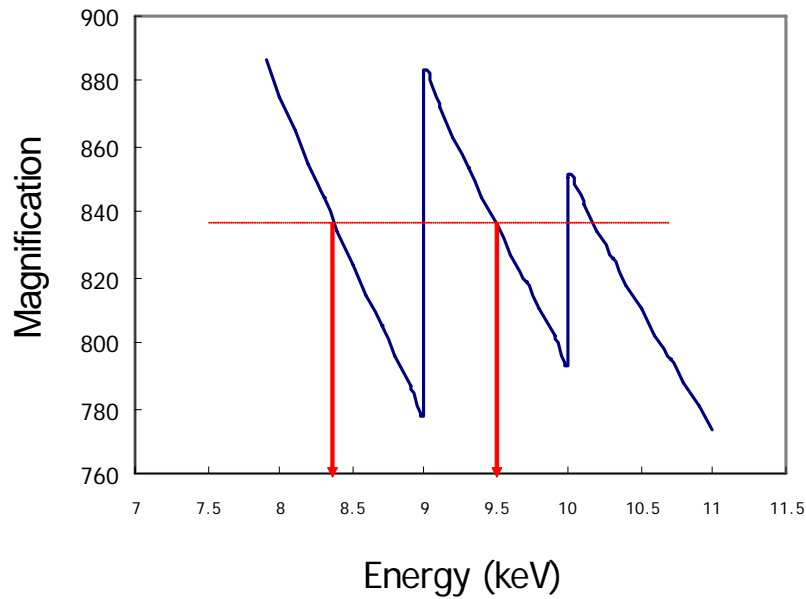
Figure 2-10 The calculated magnification versus energy from 8-11 keV range.

We demonstrated the element-specific image by imaging the copper interconnects in an IC chip. The K-edge of Cu is 8979 eV. We choose to take the two absorption images at 8.4 keV and 9.5 keV with two different zone plates that both energies have the same magnification (about 830 times, as indicated in figure 2). The two images are shown in Figures 2-11 (a) and (b) for 8.4 keV and 9.5 keV, respectively.

After the image shift is corrected by software, the intensity difference between these two images is given in figure 2-11 (c). The image contrast of figure 2-11 is given by the counts of 8.4 keV minus the counts of 9.5 keV for each pixel. The bright regions indicate the distribution of copper rich in the chip. The copper enhanced image gives clearly interconnects.
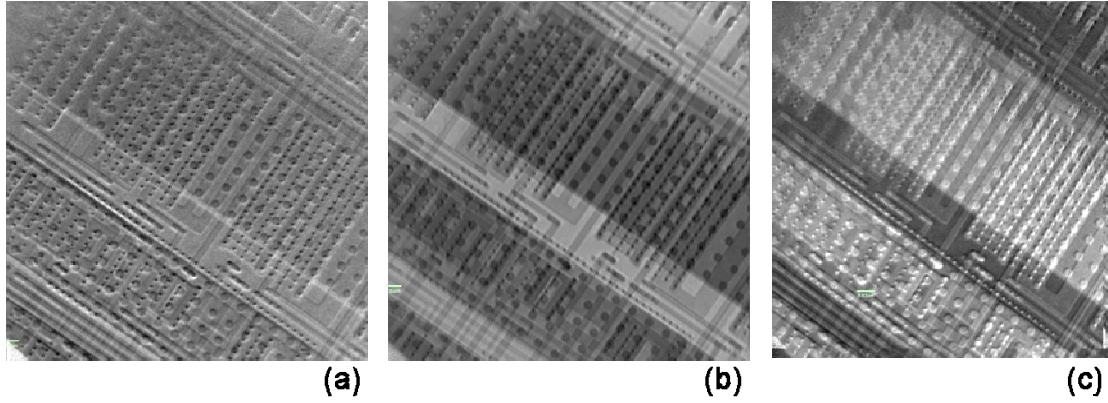
Figure 2-11 Image taken at 8.4 keV (a) and 9.5 keV (b) with different zone plate but the same magnification (c) The differential contrast shows copper-rich area.

2.4 Third Order Image

The resolution of TXM is given by 1.22dr/m as discussed before. By using a higher order diffraction of the zone plate (such as the third order diffraction [10,12]), the resolution of the x-ray microscope can be increased significantly. However, in these studies zone plates were used as a condensed lens which did not provide sufficient numerical aperture to match those of the zone plate objective, leading to significant compromise to the resolution improvement of using higher order diffraction.

The function of a pure phase zone plate ZP(x, y) in equation (2.2) is expanded with a modification according to that given by G. Schneider.[13]

$$ZP(x, y) = \exp(-i\pi(\frac{1}{2} + \frac{2}{\pi} \sum_{m=1,3,5...}^{\infty} C_m \sin[\frac{m\pi(x^2 + y^2)}{\lambda f}])) \qquad (2.2)$$

In this expression, the cross-section of zone plate is made in the rectangular shape, and can be regarded as composed by different order of lens with focus length of f/m. The C_m in the equation (2.2) is equal to 1/m for a rectangular shape of zone plate. The term 1/2 represents the zeroth order of the zone plate, and m=1, 3, 5… represent for the first, the third, the fifth order, and so on, respectively. The higher is the diffraction order, the shorter is the focus length, and the larger is numerical aperture (NA). The spatial resolution σ of the zone plate is given by σ=$K_1\lambda/NA$,[3] where the K_1 is range from 0.3~0.61, depending on the illumination condition. This TXM has a hollow cone illumination with partial coherency. The K_1 is calculated to be 0.36 by the

illumination angle with perfect coherency in our transmission x-ray microscope. However, we have obtained a suitable value of 0.45 by experimental results using first order diffraction, which will be discussed later.

The NA of a zone plate can be written as the $NA_{zoneplate} = \frac{m\lambda}{2\Delta r}$ [1], where λ is the wavelength, Δr is the outermost width of the zone plate and m=1, 3, 5 etc, the order of zone plate diffraction. Under the ideal coherency illumination, the K_1 is set to be 0.3 such that the spatial resolution of third order image for hollow cone illumination is given by $\sigma=0.61\Delta r/m$. For a partially coherent illumination in our x-ray microscope, the value of K_1 is determined to be 0.45. The resolution of third order diffraction may be estimated to be $\sigma=0.9\Delta r/m$.   In this x-ray microscope, m, the diffraction order, is 3 and Δr is 50 nm; therefore, the ideal resolution of hollow cone-beam system is close to 15 nm spatial resolution.

In principle, the spatial resolution can be improved to be m times by using higher diffraction order m at the expense of diffraction efficiency which is inversely proportional to m^2 for a zone plate with rectangular shape of zone plate. Therefore, the diffraction efficient of third order is about one order of magnitude lower than that of first order, which means the exposure time is longer and the resolution suffers more from the noise and thermal drift problem.
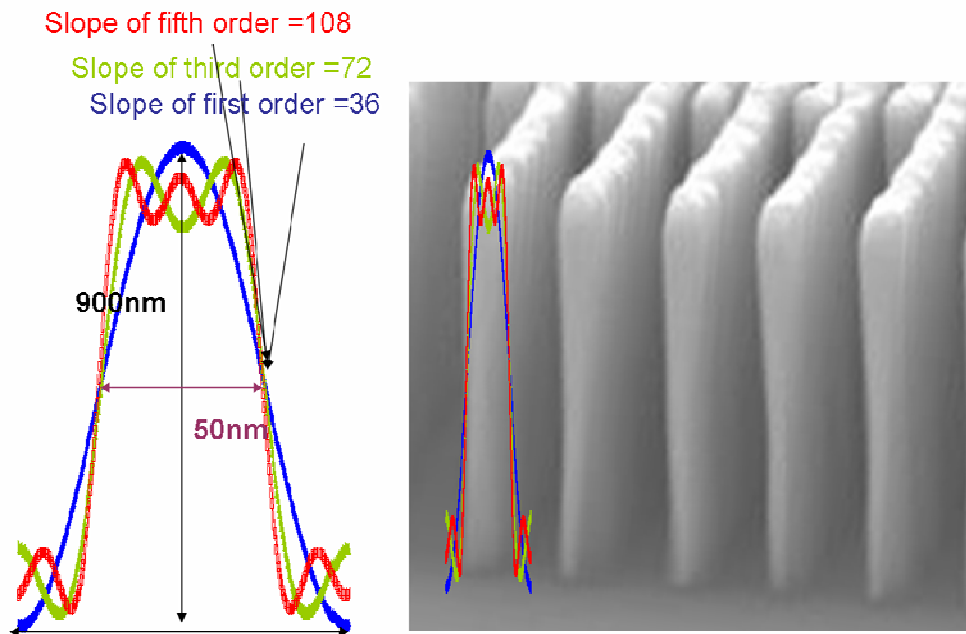
Figure 2-12 Left is the profile of the outmost zone of the zone plate. The vertical and horizontal axes are both in nanometer but in different scale. The blue, green and red lines indicate the profile of the first order, third order and fifth order of the zone plate, respectively. The red line is the mixture between the first order and third order. Right is a SEM image showing the cross section of a zone plate which has similar aspect ratio of the zone plate which used in the experiment. The comparison shows that the slope of zone plate is sharper than required.
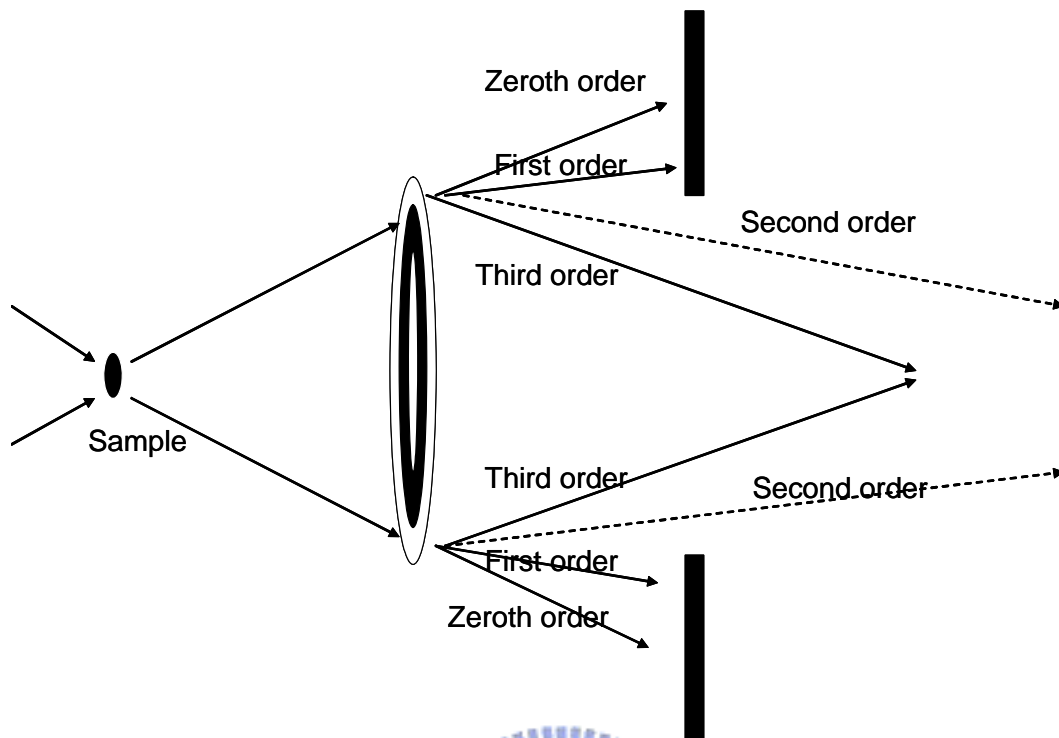
Figure 2-13 The setup for third order imaging.

The shape profile of zone plate's zones directly determines the diffraction efficiency of each diffraction order. In equation (2.2), the C_m is the coefficient of frequency; it also represents the weight of each diffraction number. According to the real fabrication process, the C_m can be altered and is no longer the same as written in the equation, $1/m$. Therefore, it is important to know the requirement of shape of zone plate to generate the third order image. The profile of cross-section of zone plate is simulated by the equation (2.2) with largest m=1,3,5, and C_m= $1/m$ as indicated in equation (2.2). As illustrated in figure 2-13, for higher order is added, the sharper is the edge of zone plate. It means the higher order appears only if the edge of the zone is sharp enough. The requirement for the zone plate to generate third order image is the slope of the edge of outmost zone is larger than the slope of first order. The higher order terms are generated by the high frequency parts of the zone plate. Assuming the required thickness of zone plate is h, the outmost zone width is Δr. In order to generate third order diffraction, the slope of the outmost of zone plate should be larger than the slope of first order, which can be approximated by the derivative of equation (2.5), The profile of zone plate in first order and third order, which can be written as $4h/\lambda f$. This value can be further simplified to $2h/dr$ if the $f=2rdr/\lambda$ is substituted. For third order, the required slope is twice as the first order.

29

$$ZP_1(r) = h(\frac{1}{2} + \frac{2}{\pi}C_1 \sin[\frac{m\pi r^2}{\lambda f}]) \qquad (2.3)$$

$$ZP_{1,3}(r) = h(\frac{1}{2} + \frac{2}{\pi}\sin[\frac{\pi r^2}{\lambda f}] + \frac{2}{\pi}\frac{1}{3}\sin[\frac{3\pi r^2}{\lambda f}]) \qquad (2.4)$$

$$\frac{\partial ZP_{1,3}(r)}{\partial r} = h(\frac{4r}{\lambda f}\cos[\frac{\pi r^2}{\lambda f}] + \frac{4r}{\lambda f}\cos[\frac{3\pi r^2}{\lambda f}])\mid_{max. at \frac{\pi r^2}{\lambda f}=0} \qquad (2.5)$$

The slopes of first order and the third are shown in the figure 2-12. The slope can be estimated by the two parameters; the zone plate thickness h is 900nm and the outmost zone width Δr is 50nm. The slope to reach the requirement for first order is 36. Hence, the slope of edge of outmost zone is required to be higher than 36 to obtain the image of third order. To obtain fifth order of diffraction, the maximum slope should exceed 72, which is the slope of third order, as indicated in figure 2-12.

In order to achieve a third order imagining field free of other diffraction orders at the imaging plane, a suitable hollow cone illumination is used to match the numerical aperture of third order as shown in figure 2-13. The cone angle is from 2.7~3.3 mrad that is generated by a capillary-based condenser. The radius of zone plate is 42.5 μm and the distance between sample and zone plate is close to one-third of the designed focal length of first order, which is about 9 mm.   The illumination of hollow cone covers in the middle parts of the zone plate in order to get uniform illumination. The distance between zone plate and scintillator is almost the same as that for first order setup. Thus, the magnification is three times lager than the magnification in first order. A pinhole is used to block the zeroth order, first order image and other undesired beams of higher orders. The schematics of the third order image setting up are depicted as figure 2-13.

The elliptical beam from the DCM is firstly focused by capillary condenser on the sample position. The focus spot is about 15 μm in diameter. The capillary utilize single internal reflection with reflection angle about 1.5mrad. With a gold bead attached in the end of the capillary, the hollow cone beam is made to mach the diameter of the zone plate, 85 μm.   The spot size of condenser is around 15 μm. The hollow cone beam with tilt angle of 2.7-3.3 mrad is well fitted for the size of zone plate. The effective focus distance of third order of zone-plate is about 9 mm - one third of the focus length of first order- while the first order is 27mm for 8 keV. The cone angle for the first order is from 0.87-1.13 mrad. The field of view is 5 μm × 5 μm in third order and the image distance is 1.2 meters. Thus, the optical magnification is derived by the image distance divided by object distance, which is close to focus

length, is about 135 times. The image on the scintillator is magnified 20 times by an optical objective. The final magnification from sample to CCD is about 2700.   As shown in figure 2-13 , the zero order and first order of the zone-plate are blocked by a pinhole of 900 μm diameter before the detector, and the third order image is then decoupled and detected by scintillator of CsI with better than 1 μm resolution. The pixel resolution on the object plane is equal to the 1 μm on the scintillator divided by the optical magnification of the microscope, which is 135. Therefore, the pixel resolution on the object plane is 7.5 nm. The relative motion between sample stage and zone-plate holder is measured by a capacitor sensor, which has a peak to peak value of 15nm. Thus, the resolution of TXM is limited by the optical properties, σ=0.9Δr/m, which is 15 nm in this case.

The zone plate is made of gold electroplated on the silicon nitride membrane. The thickness of zone plate is 900nm, generating the phase shift of π/2 at 8 KeV. In fact, π is the optimal retardation of phase zone-plate for a perfect Fresnel Zone plate, as indicated in the equation (2.2); however, the fabrication of thick zone-plate is limited by the aspect ratio that current fabrication process can reach, which is 18 in this case.(In the time of writing, the aspect ratio is close to 25 for double stack zone plate [11]) The width of outmost zone and thickness of the zone-plate are compromised between the resolution and diffraction efficiency. The efficiency of first order diffraction of the zone plate is measured to be above 10% and the third order efficiency is around 1%. The way to measure efficiency is to measure the intensity of and focus spot and non-focus spot (without zone plate). After summing the intensity in the area of focus spot and the intensity in the area of non-focus spot, the loss of flux in percentage can be calculated. The efficiency is obtained.

The testing sample is a Siemens star of 150 nm thick, which is also called the spoke pattern. The finest structure of this spoke pattern is 30 nm, which is made by electroplated gold on the silicon nitride membrane. This test sample gives the absorption of 6%.[14] The pattern has narrower line width in the inner part than in the outer part. To measure the modulation transfer function (MTF) [3,15] of the microscope is to observe the contrast inverse or blurring at certain line width. The image of first order and third order of this testing sample are taken to estimate the spatial resolution of images of first order and third order. The images of first order are shown in the figure 2-14 (a), (b) while the image of third order is shown in 2-14 (c). The figure 2-14 (d) is the image taken by SEM. The figure 2-14 (b) is the magnified view of the boxed area in figure 2-14(a). Figure 2-14 (b) and 2-14(c) shows the same areas with field of view of 4.5 μm in order to have a clear comparison to show the

enhancement of the spatial resolution. The inner line of the spoke pattern is clearly resolved in the image of third order but is fuzzy in the image of first order. The line plot of third order image shows that the half pitch of 30 nm is clearly resolved.   In order to understand the MTF of the images, the modulation is calculated by the Michelson fringe visibility, which is given by $v = \dfrac{I_{max} - I_{min}}{I_{max} + I_{min}}$. For this test pattern, absorption is 6%, the Michelson fringe visibility is about 3%. The Michelson visibility is measured in the different portion in the image 2-14(b) and 2-14(c) for different spatial frequency. After obtaining the visibility, the data is normalized with maximum visibility. The MTFs are plotted for both third and first order image as shown in figure 2-15. The horizontal axis is the frequency in lines per micron, and the vertical axis is the normalized modulation. The maximum value of the vertical axis is normalized to 6% of absorption. The cut-off frequency for the first order is found at 22.5 lines per micron, which is close to 45nm and this gives the formula σ=0.9Δr/m. However, the cut-off frequency of the third order can not be measured in this plot, since the modulation is not reach the bottom of the vertical axis. The cut-off frequency is obviously beyond the 33 lines/μm, which is the spatial resolution of 30 nm. A reasonable estimation is to extend the line of the MTF. The intercept of MTF with the noise background is the resolution of the microscope, which is about 38 lines/μm, which is the spatial resolution of 25nm. The exposure time for image of third order is about 10 minutes and the exposure time of a decent image of first order is about 60 seconds. The diffraction efficiency is a factor of 10 drop between first order and third order, which is well agreed with the theoretical prediction.
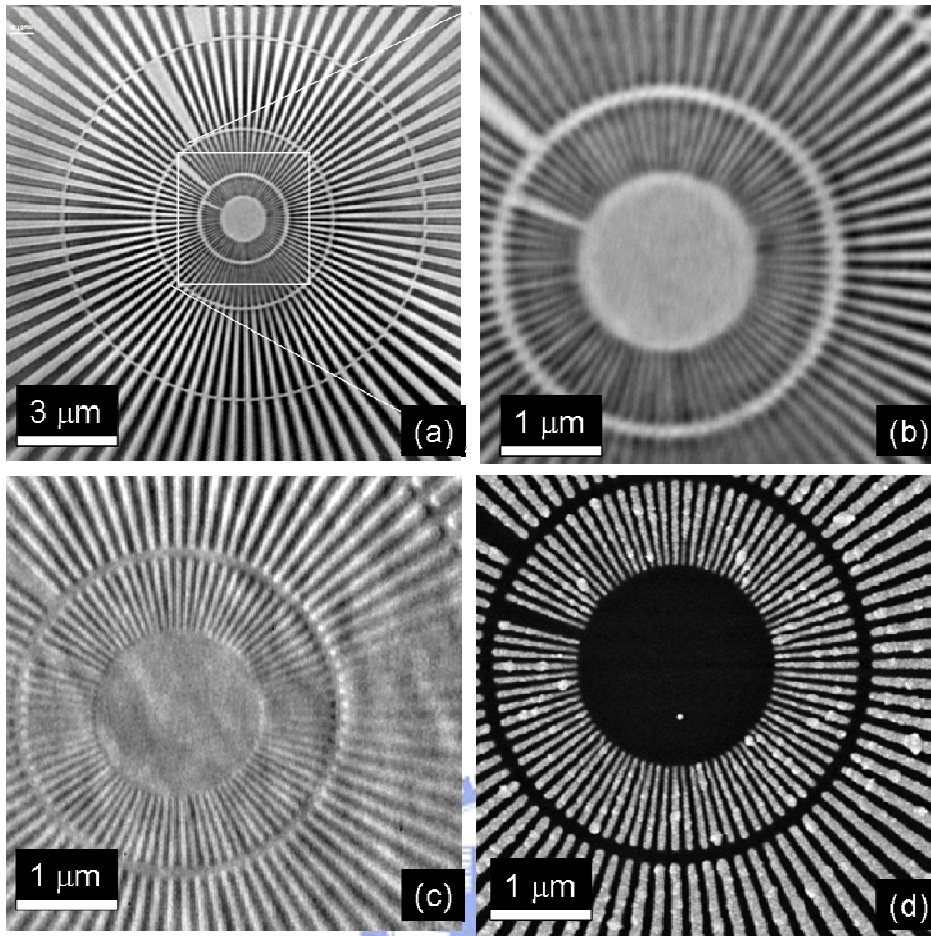
Figure 2-14 The spoke pattern are imaged under different image mode:　(a) by first order and
(b) enlarged view from the square box of first order.(c) by third order (d) by SEM. The area
marked by white square in the 2-14 (a) is the field of view of third order image. The finest
structure is in the center of the siemens star.　The image of third order exhibits more details
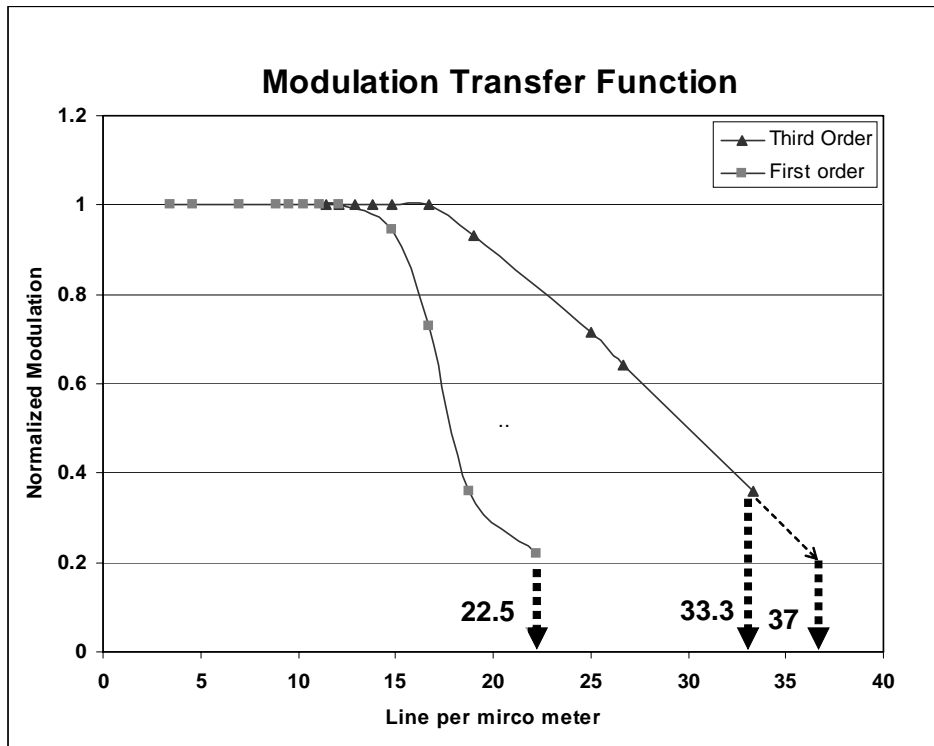than the first order.

33

Figure 2-15 The modulation transfer functions for third order and first order image. The resolution for first order (third order) is found to be 22.5 lines/μm (37 line/μm), which corresponds to a spatial resolution of 45nm (27nm).

The reasons for not achieving the ideal resolution σ=0.9Δr/m for third order are mostly likely attributed to be the thermal drift, which can be several tens of nanometers in hour. The evidence is that one can see the strip in the figure 2-14(c), which is sharp in the vertical and blur in the horizontal. The other causes may come from the mechanical instability of the microscope, imperfection of the zone plate, the imperfection of illumination of hollow cone beam generated by the source, and noise. The third order suffers more from thermal drift and noise due to longer exposure time and lower count rate.

In summary, the image of third order of zone plate in transmission x-ray microscope is demonstrated at 8 keV with better than 30nm resolution. With capillary condenser which generates the hollow cone beam. The hollow cone beam serves to decouple the lower order of image. The spatial resolution of third order image of 30nm is demonstrated.

34

2.5 Dark Field Image

Principle

The dark field of X-ray microscope [16,17] can be formed while the principle light, the zero frequency of the optical system, does not enter the detector. The way to implement the dark field is to block the principle light in the optical system so that the higher spatial frequency is enhanced in image. There are two typical optical set-ups to implement the dark field imaging in TXM. In the first case, as shown in figure 2-16 (a), based on hollow cone illumination a dark field is obtained by setting a ring-shape beam stop at the back focal plane. The other way to implement the dark field is to use the high angle illumination condenser, as shown in figure 2-16 (b), to make the principle light out of the objective zone plate range so that only X-rays of high frequency of the diffraction and the scattering from the sample will enter the detector system.

The first method is the usual way to implement the dark field in soft X-ray microscope. For hard X-rays, it is difficult to fabricate the ring stop with required thickness. For example, in order to block 99 percent of 8 keV X-rays, the gold layer needs to be 10 μm thick, which is hard to achieve by electroplating. The other issue is that the ring shape does not match the beam shape in the back focal plane which is elliptical for a synchrotron source.

For the second method, it requires that the condenser has high NA (numerical aperture) than the NA of the objective lens. For zone plate, $NA_{zoneplate} = \dfrac{m\lambda}{2\Delta r}$, where the m is the diffraction order of zone plate, λ is the wavelength, and Δr is the width of outmost zone of zone plate. In principle, zone plates of different NAs can be made for condenser and objective lens. It is also possible to employ higher order diffraction using same zone plates; however, the efficiency is generally too low.

In our study, we chose to use capillary as high NA condenser. The capillary is made of glass-based material with the critical angle ~3mrad at 8 keV. [5] The zone plate with the outmost zone 50nm has NA ~1.5mrad. Thus, the capillary condenser and the zone plate system is good for generating the dark field in our TXM.
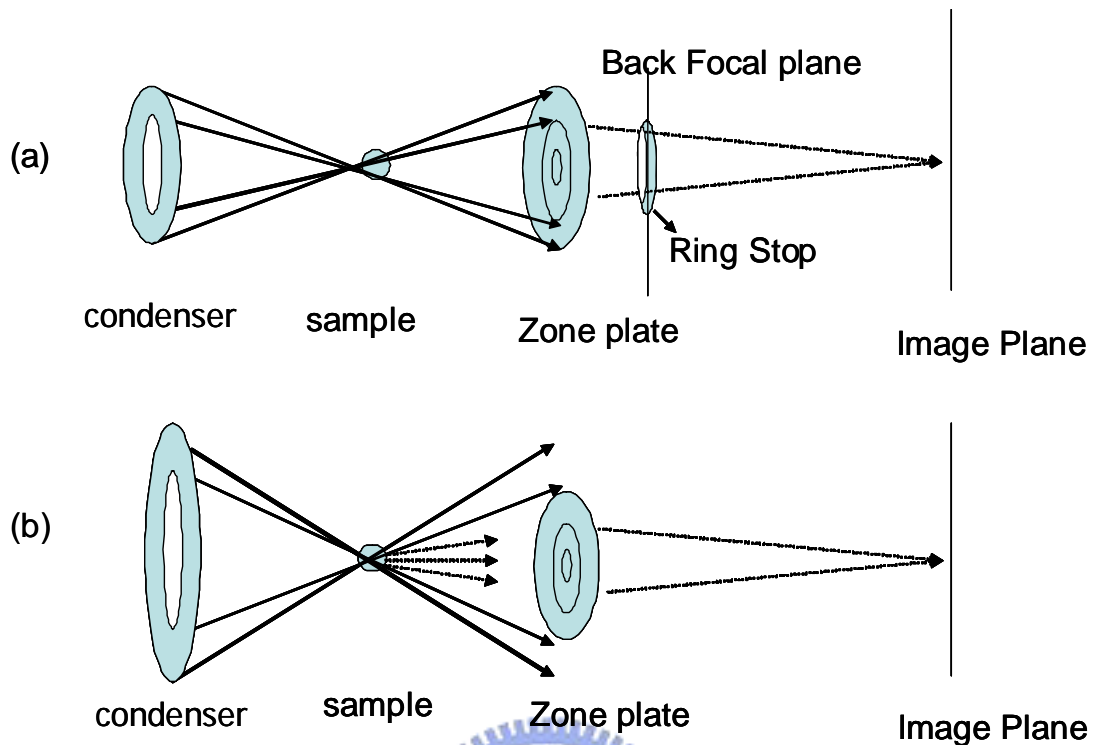
Figure 2-16 Two methods to implement the dark field in TXM.

The characteristics of the image can be understood in the frequency domain. The image is formed by the convolution of input signal and the system response. The method of high angle illumination as illustrated in figure 2-16(a) has the frequency response shown in the figure 2-17. The vertical axis is intensity (not in scale), and horizontal axis is for the frequency (not in scale). The solid blue line indicates the system response. The bright field information of a Seimens star of 30nm is plotted as a dotted blue line which is flat in low frequency, and decreases while the spatial frequency is close to 30nm. The solid blue line indicates the bright field image in frequency domain, which is a convolution of system response and bright field information of Seimens star. Followed with the same idea, the dark field image is also the convolution of the system response and the dark-field information from the sample, which is indicated as dotted red line. The dark field information of the dark field is different from that of the bright field because the signal comes from the higher order diffraction and scattering from the sample. Thus, a peak at high frequency can be found, and the position of the peak varies with the illumination angle. The intensity of the peak is not in scale with the intensity of bright field. Actually, the signal from the dark field is weak compare

36

in comparison with to that of the bright field. The dark field image in frequency domain is plotted as red solid line.

The frequency response of the dark field image is low in the low spatial frequency and increase at high frequency then decrease quickly while close to the system response. The dark field seems to have better performance of frequency than the bright field; however, in real case, the long exposure time leads to the vibration and thermal drift, which are always lower down the spatial resolution. In our experiment result, the dark field image doesn't always increase the spatial resolution practically.
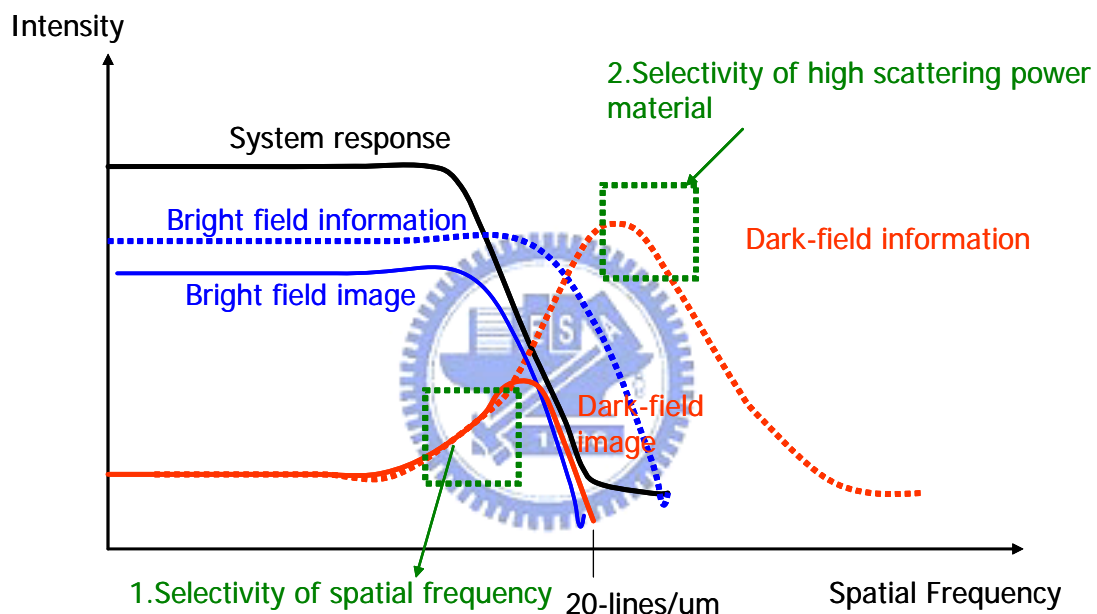
Figure 2-17 Comparison of frequency response for the dark field and bright field images.

The frequency response of the dark field has two major features. One is the selectivity of the high spatial frequency and the other one is the selectivity of the high scattering material. For the selectivity of the high spatial frequency, one can see the different response with spatial frequency, which in turn can be applied to distinguish the different size of objects. For the selectivity of the high scattering power material, it is mainly depends on the scattering power of the material, which can be used to distinguish the high Z and low Z materials. In the following sections, the two features will be demonstrated experimentally.

37

Experiments

(1) The Seimens star

The Seimens star is used to test the frequency response of the dark field image. The Seimens star is made of gold electroplated on the silicon nitride membrane. The half pitch period of inner most zones is 30 nm. Figure 2-18 (a) is the bright field of the Siemens star, there are two red circles indicates the half pitch period of 30 nm and 50 nm, respectively. The image shows the absorption contrast with reasonable uniform contrast after the flat field process.   In figure 2-18 (b) is the dark field image of the Siemens star. The area on the sample is almost the same with the image of bright field. The image is brighter in horizontal than vertical because that the characteristic of source. The image of dark field is not processed by the flat field, so that some defects on the scintillator and non-uniform illumination are observed.
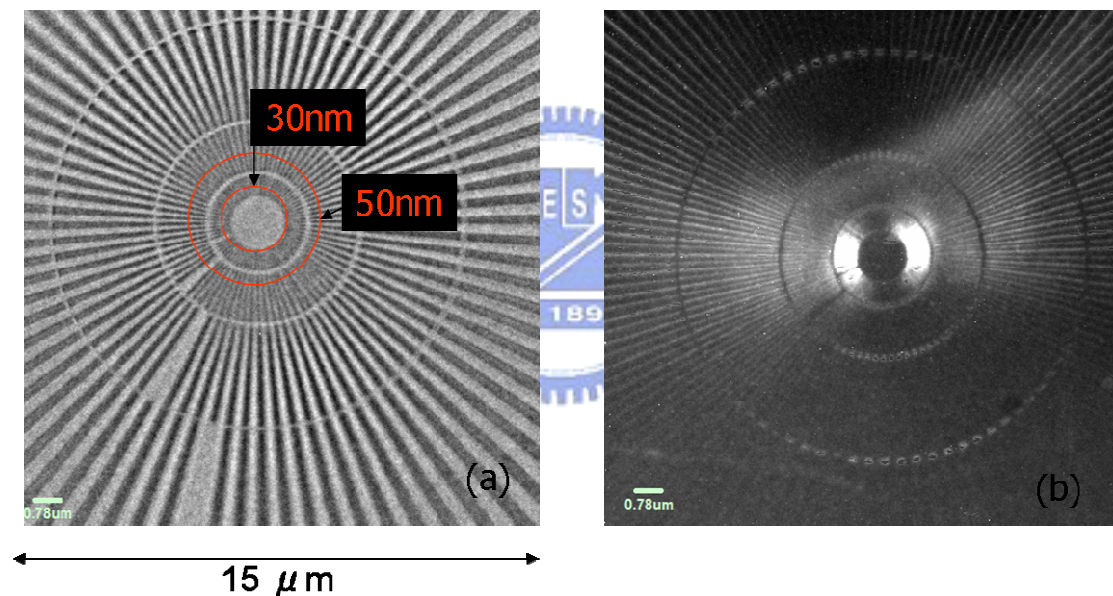

Figure 2-18 The TXM image of a Siemens star in (a) bright field and (b) dark-field. The half pitches period of 30 nm and 50 nm are indicated. The dark field image can be recognized in 50 nm and is completed swelled out at 30~50nm region.

The dark field image shows the edge of the bright field, which is good verification that high frequency is enhanced and low frequency is suppressed. The inner most part of the dark field image is swelled out- which means the resolution does not enhance in the dark field. The high spatial frequency signal becomes a white noise background.

In order to have better under standing of the frequency response, 2D Fourier transform is applied to the two images shown in figure 2-18. The corresponding power spectra are shown in figure 2-19. The center is for zero frequency, the high frequency is away from the center. The figure 2-19(a) shows a flat response with low frequency, with a hole in center, which is a discontinuity of frequency of Siemens's star because the low frequency part of the Siemens's star is not shown in the field of view. Figure 2-19 (b) is the modulus of Fourier transform of the dark field image, which shows the higher response at high frequency. This is good verification of the argument mentioned in section 2.
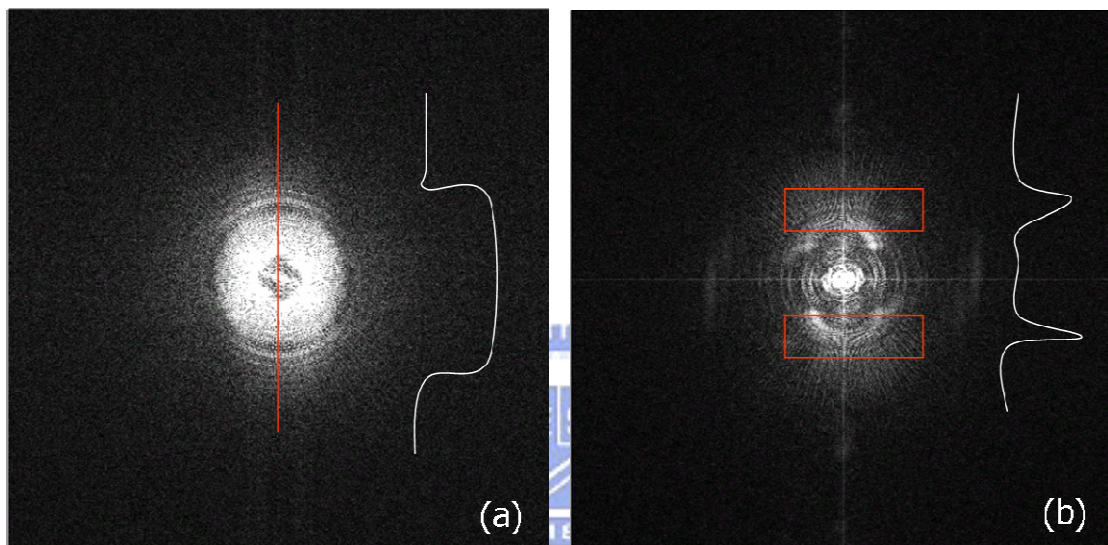
Figure 2-19 Power spectra of Siemens star from (a) bright field and (b) dark-field.

(2) The used zone plate

A used zone plate with collapse zone is used to demonstrate the selectivity of spatial resolution in the dark field image. This zone plate is made of gold with thickness of 900nm. Out most zones of zone plate is 50nm. The imaged area is near the edge of a zone plate. At the edge of the zone plate, there are support zones outside the zone plate. The support zones of the zone plate are used for supporting and adjusting the condition of electroplating, which is thicker than the outer most zones. The width of support zones is thicker than that of out most zones. The contrast difference of support zones in bright field and dark field are obvious. In figure 2-20 (a), the bright field of the zone plate, the support zones shows no contrast difference between the out most zones. However, in figure 2-20 (b), the dark field image shows a contrast difference between the support zones and the out most zones. The support zones in the dark field region become darker because that the support zone is wider

(less spatial frequency) than the out most zone, which is the selectivity of the spatial frequency.
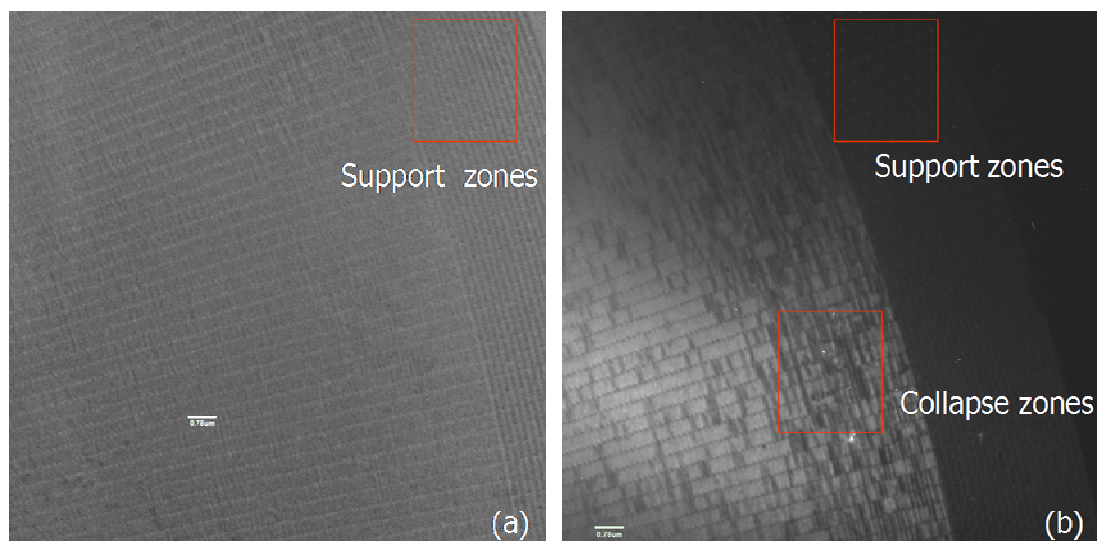

Figure 2-20 The dark field of used zone plate in (a) bright field and (b) dark-field.

We take the used zone plate as the sample is because the collapse zone is a good demonstration for the dark field. In the collapse zone, the structure of the zone plate is no longer at the position as it should be but falls on the other zones. Therefore, the effective width is larger while the zone is collapsed. Actually, the collapse zone does not vanish and still causes the absorption. This is the reason why, as shown in figure 2-20 (a) and (b), the collapse zone is clearly revealed as the dark area in the dark field and has no contrast in the bright field.

(3) The tungsten plug as the inter connection in memory chip

The tungsten plug is used to demonstrate the material selectivity. The memory chip contains multi-layer structures which are composed of tungsten, alloy of copper and alumni. In figure 2-21, we have demonstrated the high contrast ratio of tungsten plug. The alloy of copper and alumni is not seen because their low scattering power with 10.5 keV X-rays. The result demonstrates material selectivity feature in dark field imaging.
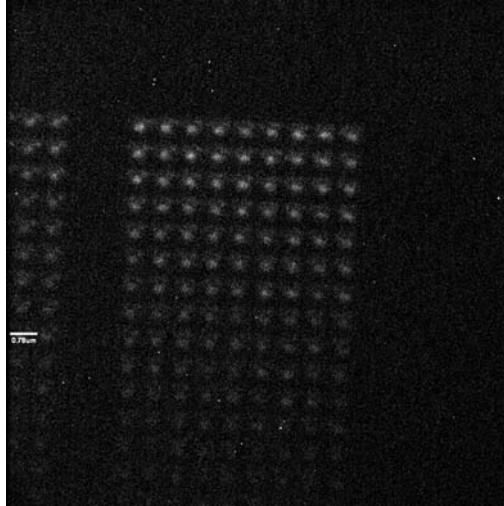
Figure 2-21. The dark field image of a tungsten plug in the memory chip.

Summary

We have demonstrated the dark field in the TXM by high angle illumination condenser at photon energy from 8 to 11 KeV. The frequency response for dark field is analyzed and studied by images of Siemens's star. Two major functions of the dark field are found and estimated. One of the functions is the selectivity of spatial frequency which is verified by the used zone plate, in which the collapse zone is unclear in bright field but clearly observed in dark field mode. The other function is the selectivity of the material, which is verified by investigating the tungsten plug in memory chip- a high contrast of tungsten plug is obtained in the dark field image.

2.6 Tomography

The computer aided tomography (CAT) or computed tomography (CT) scan tomography, which is known as computer axial tomography scan, was invented by Godfrey Newbold Hounsfield in Hayes, England at Thorn EMI Central Research Laboratories using X-rays[18]. Hounsfield conceived his idea in 1967, and it was announced in 1972. It is claimed that the CT scanner was "the greatest legacy" of the Beatles; the massive profits from their record sales enabled EMI to fund CT research. Allan McLeod Cormack of Tufts University independently invented a similar process and they shared a Nobel Prize in medicine in 1979 [19].

2.6.1 The principle of x-ray tomography.

The mathematical basis for tomography was originally developed by Radon in 1917 [20]. After the first CT scanner in 1972 by G.N. Hounsfield and Alan McCormack [21], a major breakthrough in the field of CT, the filtered back-projection (FBP) algorithm was invented by Bracewell and Riddle [21], which is the algorithm now used by almost all commercially available CT scanners. More literature survey can be found at these references [22].

2.6.1.1 Projections

The Filtered Back Projection algorithm [21] utilize Fourier theory to solve a closed form solution to the problem of finding the linear attenuation coefficient at various points in the cross-section of an object. A fundamental result linking Fourier transforms to cross-sectional images of an object is the Fourier slice theorem [23, 24]. In this chapter, we discuss only how the projection is generated by the parallel beam both in theoretical and computer programming. The figure 2-22 illustrates how attenuation and phase retard are calculated for cross-section-projection of an object. The Fourier slice theorem does not actually involve in how the matter interacts with light. The Fourier slice theorem begins with a simple mathematics that sums all the value of the path as illustrated in equation (2.6).

$$p_\theta(t) = \int_{(\theta,t)line} f(x,y)ds = \sum_{(\theta,t)line} f(x,y) \qquad (2.6)$$
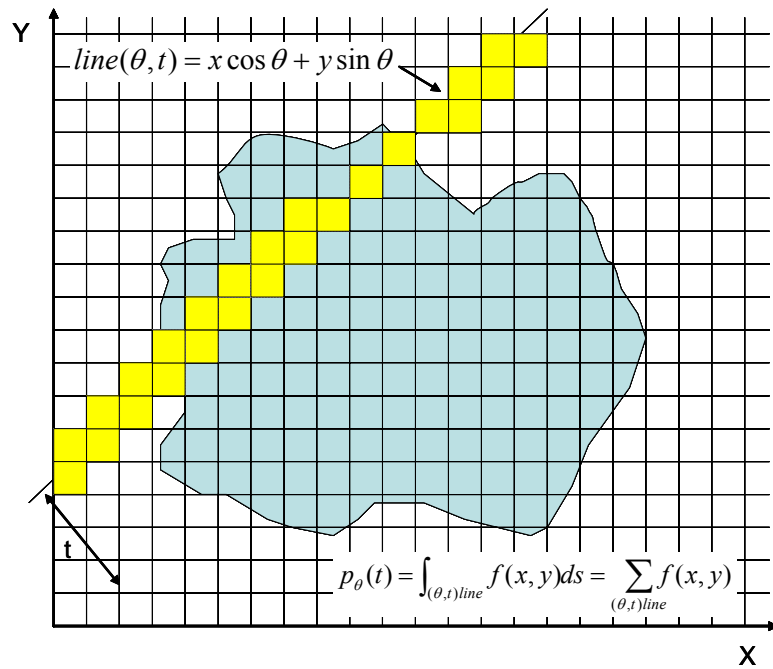
$$line(\theta,t) = x\cos\theta + y\sin\theta$$

Figure 2-22 The schematic of projections of the object.

$p_\theta(t)$, the line integration along the line(θ,t), can be calculated as written in Equation (2.6). In computing, the integration can be approximated by summing all the mesh values on the line as shown in yellow blocks in figure 2-22.

The equation (2.6) can be written using a delta function as:

$$p_\theta(t) = \int\limits_{-\infty}^{\infty}\int\limits_{-\infty}^{\infty} f(x, y)[\delta(x\cos(\theta) + y\sin(\theta) - t)]dxdy \qquad (2.7)$$

This function is known as the Radon transform of *f(x,y)*, where the t stands for the shift, and the θ is the projection angle. The simulation results are shown in the figure 2-23. The rotation center is at the middle of the image.
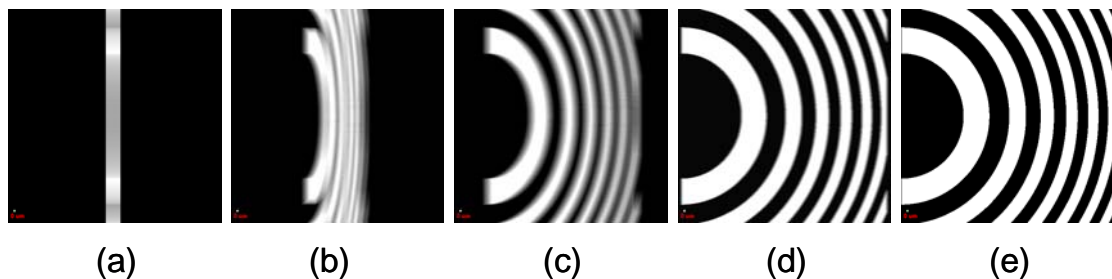

(a)　　　(b)　　　(c)　　　(d)　　　(e)

Figure 2-23 Simulation of projections of a half-zone plate. (a) to (e) are the projections in -90, -75 ,-45 ,-15, and 0 degrees, respectively.

43

2.6.1.2 Fourier Slice Theorem

An important and result linking Fourier theory to the projections was developed by Bracewell [21], Ramachandran and Lakshminarayanan [25,26]. The following proof is a result of Kak and Slaney [23]. The 2D Fourier transform is defined as:

$$F(u,v) = \int\limits_{-\infty}^{\infty}\int\limits_{-\infty}^{\infty} f(x,y)e^{-j2\pi(ux+vy)}\,dxdy \qquad (2.8)$$

where u and v are the spatial frequencies, measured in radian/length unit. From the definition of the 1D Fourier transform, the Fourier Transform of the projection data at any angle can be given as equation (2.9):

$$S_\theta(\omega) = \int\limits_{-\infty}^{\infty} P_\theta(t)e^{-j2\pi\omega t}\,dt \qquad (2.9)$$

Where, ω is in radian per unit length.

We define a new coordinate system (t,s) defined by the rotation of the (x,y) system by the angle of rotation such that,

$$\begin{bmatrix} t \\ s \end{bmatrix} = \begin{bmatrix} \cos\theta & \sin\theta \\ -\sin\theta & \cos\theta \end{bmatrix}\begin{bmatrix} x \\ y \end{bmatrix} \qquad (2.10)$$

In the (t,s) co-ordinate system, a projection would then be defined as

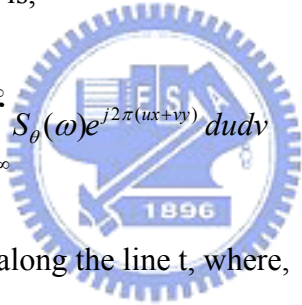$$P_\theta(t) = \int\limits_{-\infty}^{\infty} f(t,s)\,ds \qquad (2.11)$$

Substitute Equation (2.11) into (2.9),

$$S_\theta(\omega) = \int\limits_{-\infty}^{\infty} [\int\limits_{-\infty}^{\infty} f(t,s)\,ds]e^{-j2\pi\omega t}\,dt \qquad (2.12)$$

This can be transformed into the (x,y) coordinate system using the result of equation (2.10) to get the following result:

$$S_\theta(\omega) = \int\limits_{-\infty}^{\infty}\int\limits_{-\infty}^{\infty} f(x,y)\, e^{-j2\pi\omega(x\cos(\theta)+y\sin(\theta))}\, dxdy \qquad (2.13)$$

The right hand side of equation (2.13) represents the two-dimensional Fourier transform of the density *f(x,y)* and left hand side is the 1D Fourier transform of the projections. Therefore, taking the 1D Fourier transform of the projections of an object at an angle θ is equivalent to obtaining the two dimensional Fourier transform of the density *f(x,y)* along the line "t" inclined at an angle θ. Therefore if we take these projections at many angles, we can get this 2D Fourier transform of the projections at many such lines inclined at various angles. If the number of angles is large enough, we will get many lines of 2D Fourier transforms of the object. If the inverse Fourier transform of all these lines is found, we get the object's densities *f(x,y)* for all (x,y) in the object's cross-section. That is,

$$f(x,y) = \int\limits_{-\infty}^{\infty}\int\limits_{-\infty}^{\infty} S_\theta(\omega) e^{j2\pi(ux+vy)}\, dudv \qquad (2.14)$$

represents the back projection along the line t, where,

$$S_\theta(\omega) = F(\omega\cos\theta, \omega\sin\theta) = F(u,v) = F(\omega,\theta) \qquad (2.15)$$

This is the Fourier Slice Theorem, and in essence provides a justification for using the Fourier theory in the CT algorithms.

2.6.1.3 The Filtered Back Projection (FBP) algorithm

Proof of the filtered back projection algorithm follows equation (2.11). The following proof is done by Kak and Slaney [23]. If the coordinate system in the frequency domain (u,v) which is in Cartesian coordinates is changed to the polar coordinates system, we have to make the following substitutions:

$$u = \omega\cos\theta, v = \omega\sin\theta \qquad (2.16)$$

where, ω = radius and the θ= angle in radians and the differentials change as

$$dudv = \omega d\omega d\theta \tag{2.17}$$

$$f(x, y) = \int_0^{2\pi}\int_0^{\infty} F(\omega, \theta)e^{j2\pi\omega(x\cos\theta + y\sin\theta)}\, \omega d\omega d\theta \tag{2.18}$$

(2.18) can be further simplified because of its symmetry.

$$f(x, y) = \int_0^{\pi}\int_{-\infty}^{\infty} [F(\omega, \theta)e^{j2\pi\omega(x\cos\theta + y\sin\theta)}\, |\omega|d\omega]d\theta \tag{2.19}$$

From (2.9) and (2.12), we can say that in this case, F(ω, θ) inside the integral is the same as S(ω) of equation (2.8). Therefore,

$$f(x, y) = \int_0^{\pi}\int_{-\infty}^{\infty} [S_\theta(\omega)|\omega|e^{j2\pi\omega(x\cos\theta + y\sin\theta)}\, d\omega]d\theta \tag{2.20}$$

This is the algorithm of filtered-back projection. The |ω| stands for the frequency filter which is reason that the "filtered" is named.

In the figure 2-24 are examples for the reconstruction filtered-back projection, which is the cross-section of reconstructed model of zone plate. From figure 2-24, it shows that the more projection images used for reconstruction, the better the resolution and less noise in the reconstructed tomography. It is straight forward that the required number of projected images is the same as the pixel number, which are completely filling the high frequency of the reconstructed slice. However, in the experiment, only finite number of images can be recorded due to practical reason; the number of projection is always less than the pixel number of image. This limitation comes from various reasons, the stability of the experiment, time budget, or the dose limit.
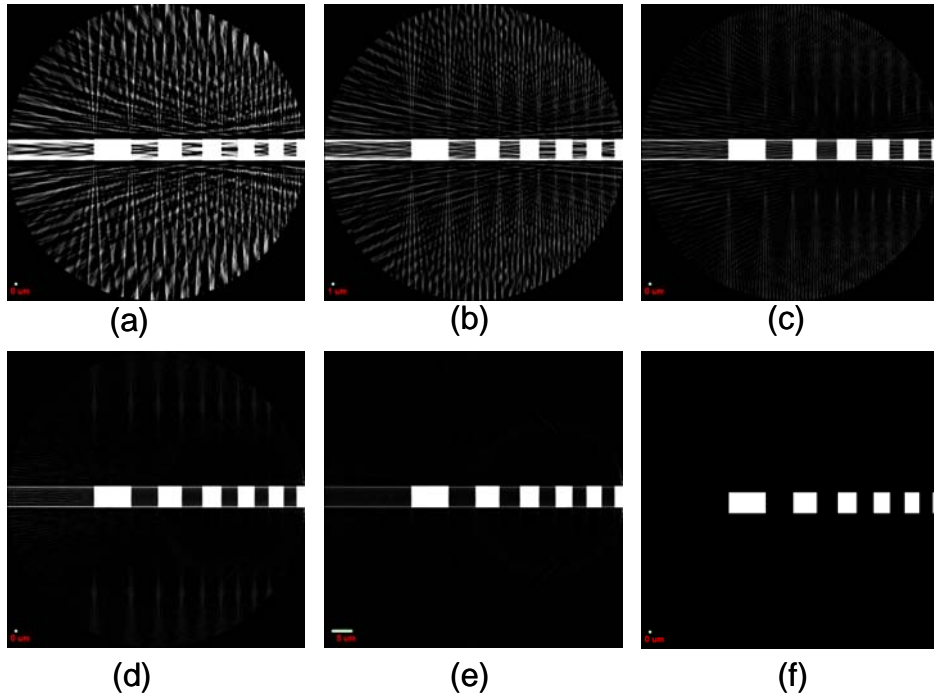
Figure 2-24 The reconstructed slice of tomography (a)-(e) and the original slice (f) by number of projections. The model is the middle layer in a zone plate, whose projection images are shown in figure 2-23. The pixels of image are 512×512, and the slices are reconstructed from 32 (a), 64(b), 128(c), 256(d), 512(e) projections. The gray scale (display range/color map) is set to 30% of the original slice to enhance the noise visually.

Note that FBP assumes the projected intensity obeying a linear summation rule that is equal to sum value along the line and FBP is not related to the interaction between light and matter. The reason that FBP is also good for phase reconstruction is the phase can be accumulated in the macroscopic view, but the phase wrap (over 2π) case is not applicable in the FBP.

2.6.2 Nano Tomography

2.6.2.1 Synchrotron Radiation (SR)-based micro tomography

The conventional tomography by the general SR-based tomography is sourced by SR, with no optics to enhance the resolution [27]. The SR-based tomography is also known as micro tomography because the resolution of the tomography is around several microns, as usually limited by the pixel size of the scintillator. Comparing to the conventional tomography with laboratory source, the SR-based tomography has brighter and higher coherent x-ray source. This tomography is good for large scale object with millimeter in size and micrometer in resolution. This application is useful for non-destructive investigation for both solid material samples and biological tissues.

The setup of SR-based tomography is as shown as the figure 2-25. A series of projected x-ray images can be recorded, usually, after the sample is rotated every one degree. Generally, the resolution of tomography depends on the number of the projection images in the axial direction as explained in previous section.
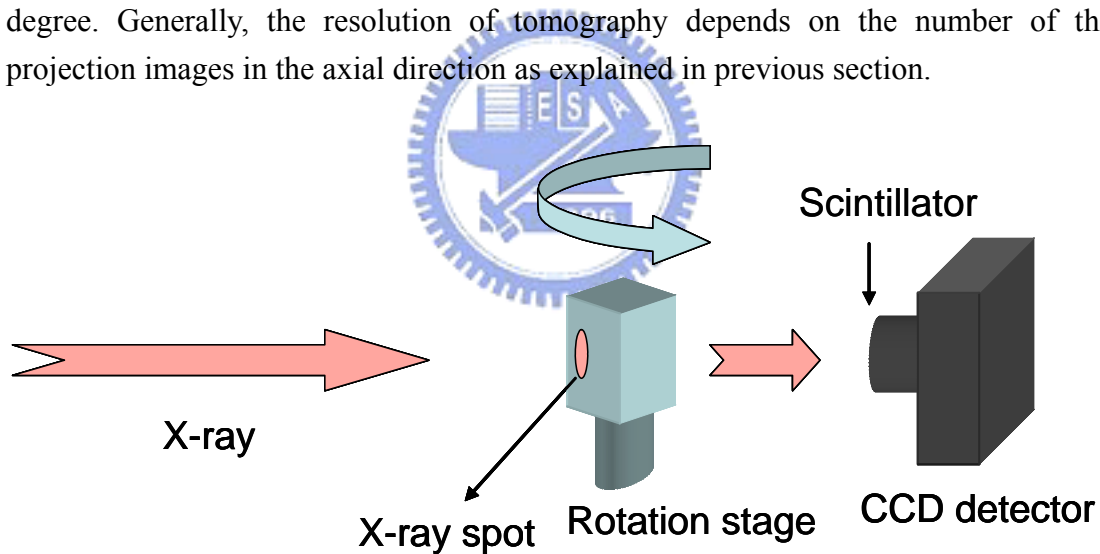

Figure 2-25 The setup for SR-based tomography.

The contrast of the SR-based tomography is mainly based on the absorption contrast, which is mainly because of the size of the object is big enough to give the contrast of the image. It is always possible to tune the energy to obtain the adequate absorption contrast of the sample to get enough signal of the sample unless there is a special concern about the dose. It is also possible to do the phase tomography by calculating diffraction fringes, which will be discussed in chapter 3.

2.6.2.2 Nano tomography by TXM

The nano-tomography means the resolution of the tomography reaches several tens of nanometer. This is because the use of the x-ray lens to magnify the x-ray image that overcomes the limitation of the pixel size of scintillator. As described in pervious section, the resolution of the x-ray microscope is around 60nm or better [5]. Thus, the nano-tomography can be done by taking a series projected images from the high resolution x-ray microscope. The basic principle is just the same as the conventional tomography but with the difficulty in alignment, which arises from the rotation center alignment, vibration, wobble, and thermal drift.

The tomography requires the good qualities of images for quantitative computation. Although computer can perform automatic data acquisition for tomography, it is difficult to make the sample stable in nanometer scale for a long period due to the vibration and the wobble of rotation stage, the misaligned in horizontal and vertical direction could be several microns. The alignment of image becomes important, since the tomography requires each images are accurately aligned to obtain a quantitative reconstruction. This requires an automatic alignment process in software which is developed to calculate the center of rotation of the sample from each angle. The alignment of data is processed by a phase correlation method [28], which is a modified method from the cross correlation method [29]. The tomography data set can be automatically aligned and reconstructed by software.

The following paragraphs are the first nano-tomogrpahy at the resolution of 60 nm, which is demonstrated by imaging the tungsten plug in the integrated circuit (IC). The issue often encountered is the tungsten plug is defect in its center, which is called "key hole" formed in the electroplating process of tungsten. The "key hole" can cause the breakdown of the circuit. The tomography data sets are reconstructed from 141 images, from -70 to +70 degrees, which is taken under 10.5 keV, above the absorption edge of the tungsten (10.2 keV). The projection images are shown as figures 2-26 (a) to (e). The image is then sent to the phase correction method [29] to find the common area. The field of view is 15 μm. The image is then processed by the phase correlation method to get a common area for reconstruction as shown in the figures 2-27 (a) to (e). After determining the rotation center, the projection images are processed by filter-back routine projection for reconstruction.   The exposure time for zero-degree image is one minute, and increases according to the angle between the normal of sample and input beam.
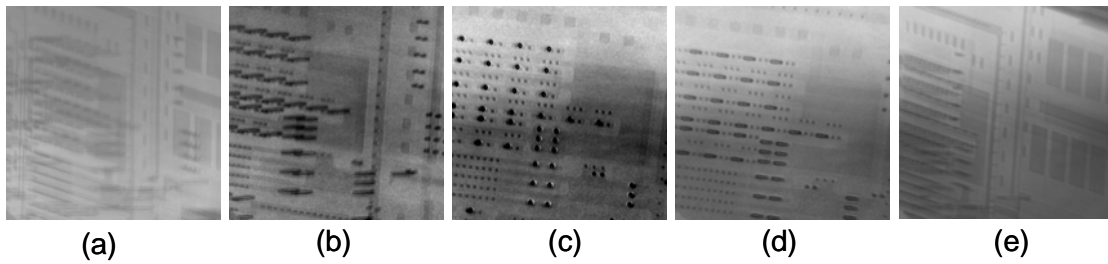
Figure 2-26 The projection images from IC before process. The projection angles of image (a) to (e) are -70, -30, 0, 30 and 70 respectively. The field of view is 15 × 15 μm and the pixel number is 512 × 512.
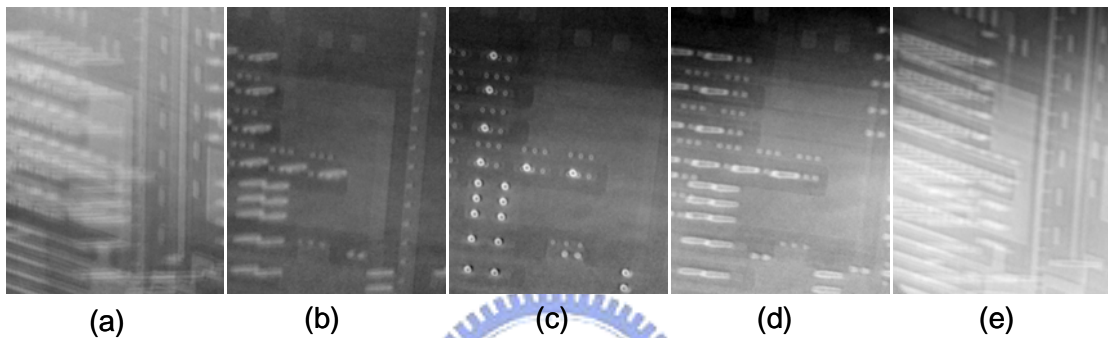

Figure 2-27 The projection images from after align and reference processes. The projection angles of images from (a) to (e) are -70, -30, 0, 30 and 70 respectively. The field of view is 9.6 × 12.6 μm and the pixel number is 327 × 431.
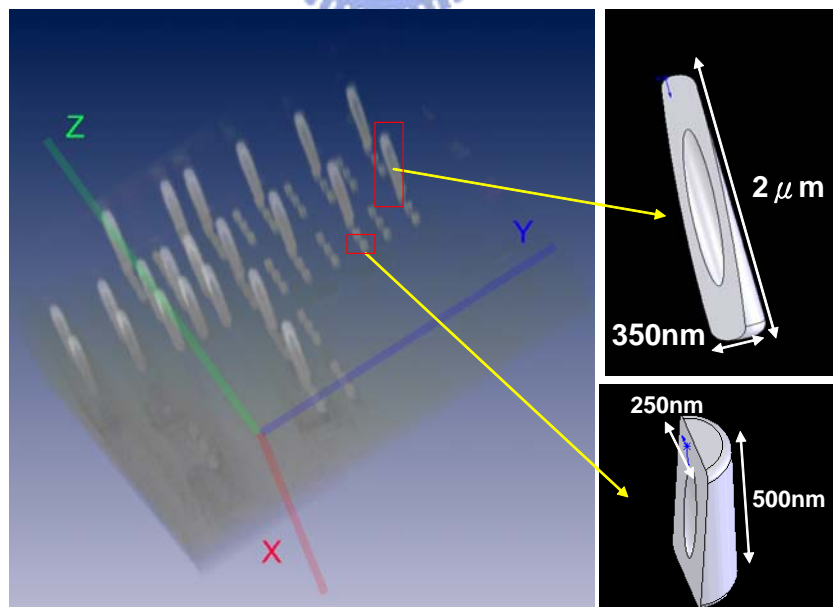

Figure 2-28 3D rendering of tungsten plug with "key hole" and the diagrams showing the structure of the key hole- right up, the tungsten plug with 350 nm- diameter. Right bottom, the tungsten plug with 250 nm-diameter.

The reconstructed tomography is shown in figure 2-28 and the cross-section diagram indicates the tungsten plugs of 350-nm and 250-nm contains a "key hole". Figure 2-29 shows the 3D rendered image with the lower absorption removed. The low absorption is generated by wire made of alloy of copper and aluminum. Therefore, the figure 2-29 shows a clear tungsten distribution.
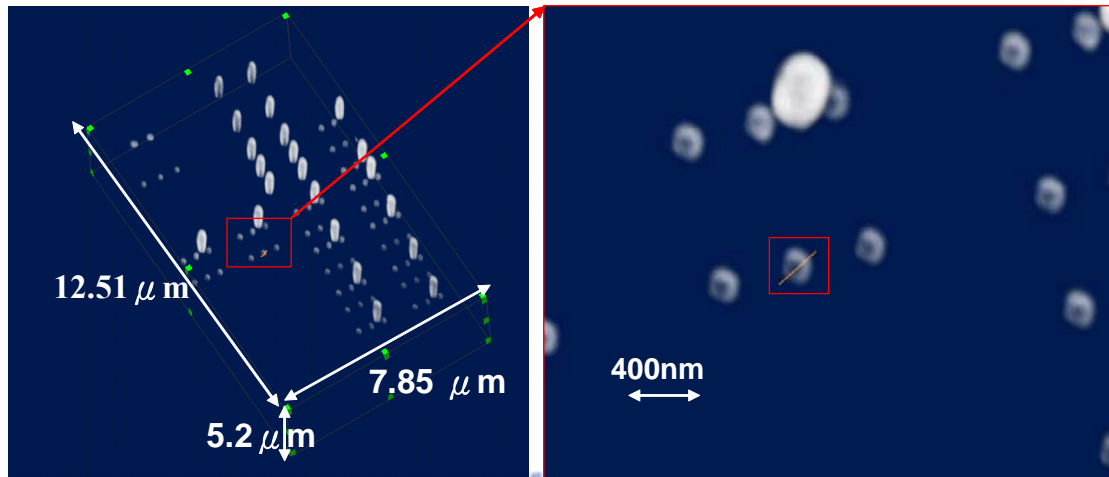

Figure 2-29 The 3D rendering of tungsten plug is plotted with higher threshold. The wire made of copper-aluminum alloy is removed from the rendering; the tungsten distribution is shown. The red region of left picture is the region of right picture. The red region in the right picture is the tungsten plug, which is displayed in 4-6.

The tomography data sets consist of an area of 12.51 μm × 7.85 μm × 5.2 μm. A magnified tomography is shown in the right part of figure 2-29, on which the red boxed region indicates the area to be analyzed. The region contents a 250 nm tungsten plug with a keyhole inside. The original data in this area was cropped and interpolated for smoothing the data. The interpolated data is shown in figure 2-30.
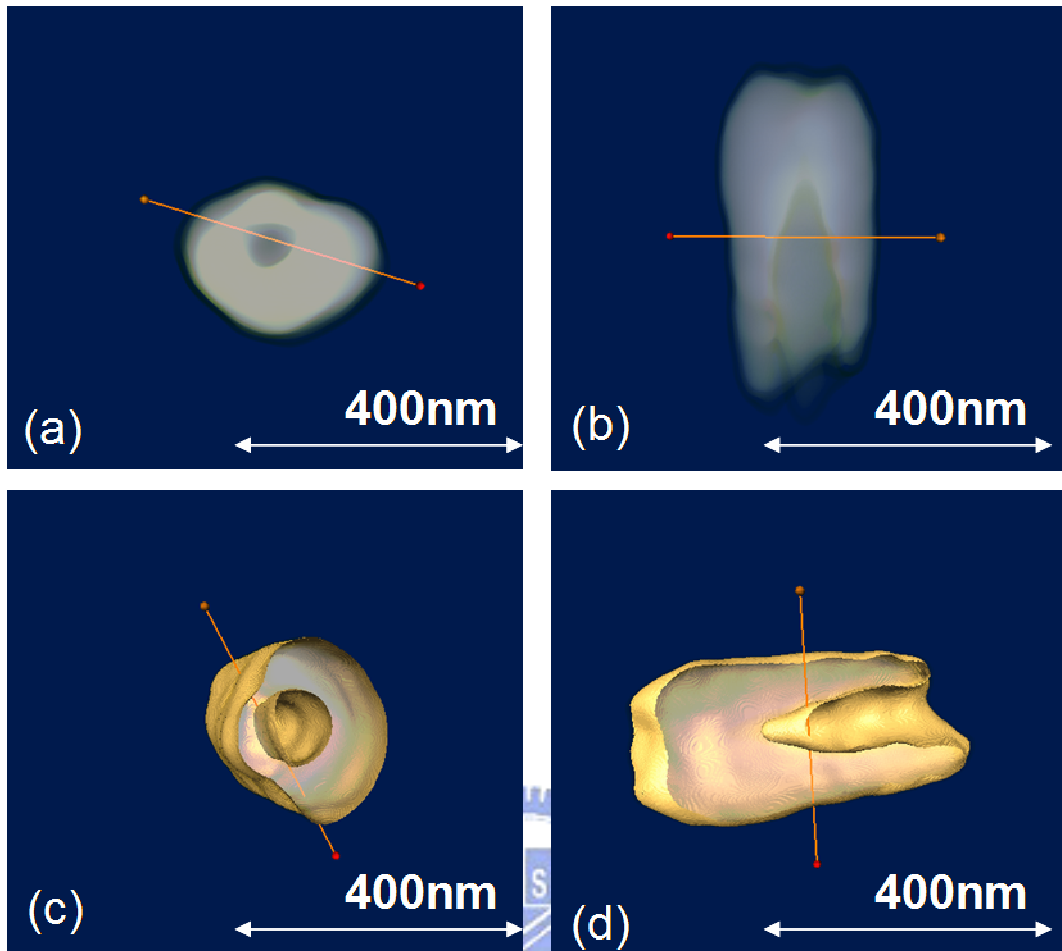
Figure 2-30 The top-view(a)(c) and side view (b)(d) of the tungsten plug displayed in voxel mode (a),(b) and iso-surface (c)(d) mode. The orange line indicates the region of cross-section plot which is shown in 2-31.

The four pictures in figure 2-30 are the top view and side view displayed by the voxel mode and iso-surface mode. A three dimensional line plot is used to measure the three dimensional resolution which is shown as the orange line in figure. The line plot is shown in figure 2-31. The vertical axis is the relative absorption, which is converted from the original tomography data set. The maximum absorption is set to 100 and minimum absorption is set to 0. The horizontal axis is the distance, which is 400nm in the line plot. The plot shows the cross section of the "key hole", with two maximums of the absorption indicating the walls of the tungsten plug. The first maximum and second maximum is at 60 nm and 210 nm. The resolution of tomography data set can be judged from the absorption goes from 20% to 80% in 62 nm, and the period is in 124 nm. We conclude the half pitch resolution of tomography is around 60 nm. The diameter of this "key hole" is estimated from 50 nm to 80 nm as shown in the figure 2-31. In average, the size of key hole is about 75 nm.
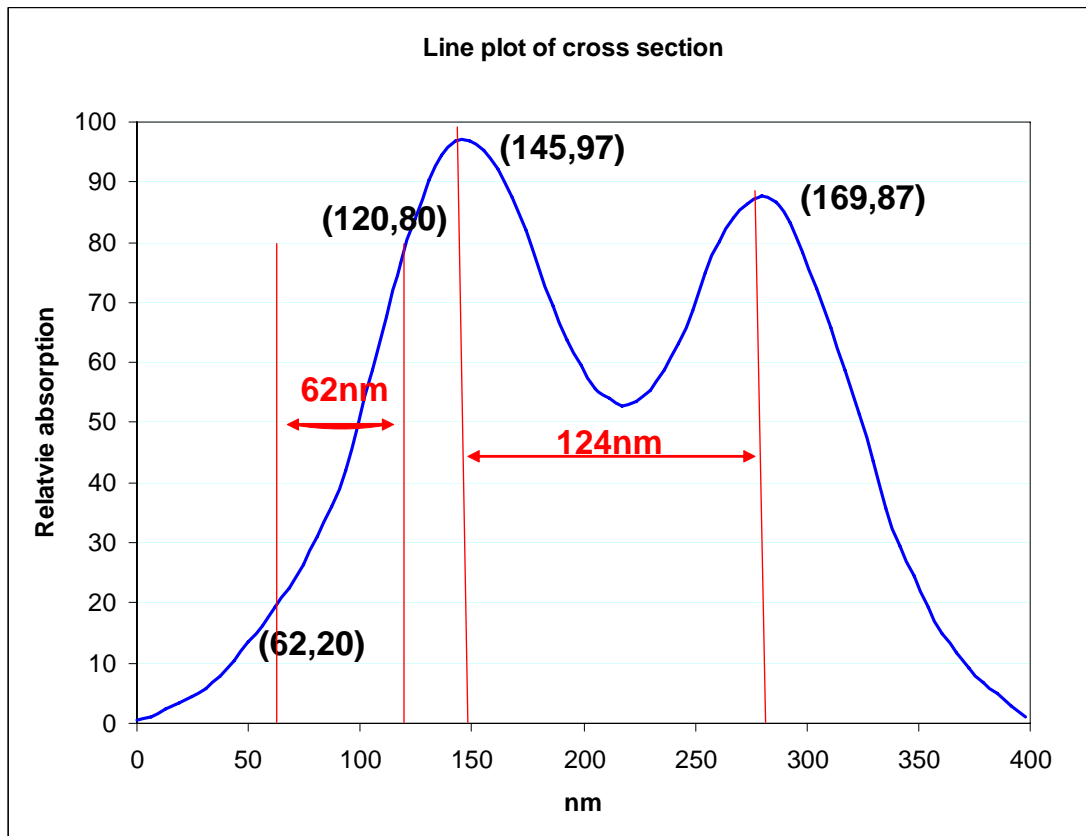
Figure 2-31 The cross-section plot of orange line in the 2-30. The resolution is estimated closed to 60nm. The resolution of the TXM in three dimension is not determined by the reciprocal space is because the noise level is hard to judge.

2.7 Summary

In this chapter, the basic structure and optical components in TXM are introduced different image modes of TXM are demonstrated. This TXM reaches the resolution below 30nm and with the energy tunable source from 8 keV to 11 keV, which is provided by NSRRC super conduction wavelength shifter. This TXM also has the functions that optical microscope have such as dark field mode. We also demonstrate the capability of 3D tomography in this microscope.

Chapter 3

Phase Retrieval of Wave Propagation in TXM

Phase imaging technique based on the real part of refractive index of X-rays has emerged as a possible solution to the otherwise low contrast materials such as biological cells and polymers. Using image processing methods to retrieve quantitative phase information was reported previously for visible light [1], X-ray radiography [2] and electron microscopy [3,4] with achievable resolution range typically limited to micron size. In this chapter, the approach is applied to treat images recorded from the zone plate type Transmission X-ray Microscopy (TXM) [5-7] which can be applied to specimens of feature size from micron down to tens of nanometer. We have developed a methodology that uses two phase retrieval techniques in a complementary fashion to achieve high resolution. The study shows that application of phase retrieval is much more complicated in TXM than that of in-line lensless phase contrast imaging [2] due to the magnification effect of zone plate. Our approach takes advantage of the strength of the Transport Intensity Equation (TIE) [2,8-9] and the Self-Consistent Wave Propagation[3,4] (SCWP) methods and their characteristic response to spatial variation. In general, SCWP is known to retrieve phase more effectively in higher frequency range of an image, while TIE works best with object of larger scale (low frequency). Our approach therefore uses TIE to compose the first guess of the SCWP, and then use SCWP to perform the iterative calculation to converge to a final result. The retrieved results of our experiments using TXM are shown to compare directly with simulation.

The capability of retrieving phase information quantitatively is particularly important considering the recent progress in x-ray microscopy. The high penetration of x-rays has given x-ray microscopy unparalleled capability to examine micro- and nano-structures buried deep inside large specimens without suffering limitation imposed by diffraction. Using state-of-the-art nanofabrication for production of diffractive x-ray optics, we demonstrate that these zone plate lenses can be used to magnify multi-keV x-rays at a resolution level of 30nm [6]. Parallel to the improvement of lateral resolution, the high coherence of the synchrotron x-rays also enables the phase contrast imaging feasible without substantial loss of intensity. In fact, the use of synchrotron x-rays to produce phase contrast and high resolution images contributed to the revolution of x-ray micro-radiology in the past decade. [10]

For X-ray imaging, the phase information is generally extracted in a qualitative

approach.   Few attempts [2,9,11] to extract quantitative phase value (real part of the refractive index) are so far limited to micron level of image resolution. These approaches do not automatically apply to nano-meter resolution x-ray imaging or to zone plate optics. For high resolution x-ray the imaging, that can now routinely be performed at sub-100nm level, phase contrast is even more important due to the loss of absorption contrast for small features.   For small objects in the sub-100nm range composed of soft (low Z) materials, phase contrast is typically 100 to 1000 times larger than absorption contrast. This increased contrast for phase imaging not only improves the image quality but also reduces the radiation dose to the sample and minimizes radiation damage for sensitive samples.

We start with the introduction of the TIE and SCWP methods in sections 3.1 and 3.2. The contrast transfer function (CTF) is discussed by the direct method (Gerchberg-Saxton. Algorithm [12]) to solve the phase of a wave by intensity variation in an iterative way and comparison between the TIE and SCWP is demonstrated in section 3.3. A proposed method for obtaining quantitatively the phase image in the transmission X-ray microscope is proposed and experimentally demonstrated in the section 3.4, followed by a summary in the section 3.5.

3.1 Transport of Intensity Equation (TIE)

The TIE is the equation that describes the phase of wave with known intensities which are recorded in different positions. The history of this equation has been briefly introduced in the chapter 1. The derivation the TIE from the wave equation in free space is shown below.

The TIE starts from the waves.

$$\psi(\vec{r}_\perp, z) = A(\vec{r}_\perp, z)e^{i\varphi(\vec{r}_\perp, z)} \tag{3.1}$$

$$\psi^*(\vec{r}_\perp, z) = A(\vec{r}_\perp, z)e^{-i\varphi(\vec{r}_\perp, z)} \tag{3.2}$$

$$\psi^*\psi = A(\vec{r}_\perp, z)^2 = I(\vec{r}_\perp, z) \tag{3.3}$$

Where $\vec{r}_\perp$ is a position vector in the plane perpendicular to the z direction (wave propagation direction), and k is the wave number. $A(\vec{r}_\perp, z)$ is the amplitude of the wave, $\varphi(\vec{r}_\perp)$ is the phase or wave front.

With the paraxial approximation, the amplitude $A(\vec{r}_\perp, z)$ satisfies the linear paraxial equation and $A(\vec{r}_\perp, z)$ can be described by $\sqrt{I(\vec{r}_\perp, z)}$.

$$(2ik\partial_z + \nabla_r^2)\sqrt{I(\vec{r}_\perp, z)} \exp[i\varphi(\vec{r}_\perp, z)] = 0 \tag{3.4}$$

where ∇_r^2 is the Laplacian operator, only in the $\vec{r}_\perp$ direction; $I(\vec{r}_\perp, z)$ represents the intensity distribution and $\varphi(\vec{r}_\perp, z)$ is its phase. The left-hand side of equation (3.4) is multiplied by $\psi^*(\vec{r}_\perp, z)$ and the left-hand side of the complex conjugate of equation (3.4) is multiplied by $\psi(\vec{r}_\perp, z)$.

Therefore,

$$\psi^*(\vec{r}_\perp, z)(2ik\frac{\partial}{\partial z} + \nabla_r^2)\psi(\vec{r}_\perp, z) = 0 \tag{3.5}$$

$$\psi(\vec{r}_\perp, z)(-2ik\frac{\partial}{\partial z} + \nabla_r^2)\psi^*(\vec{r}_\perp, z) = 0 \tag{3.6}$$

Subtracting the two equations (3.3) and (3.4) and rearranging the terms for left hand side, the equation becomes:

$$-2ik(\psi^* \frac{\partial}{\partial_z}\psi + \psi \frac{\partial}{\partial_z}\psi^*) = \psi^* \nabla_r^2 \psi + \psi \nabla_r^2 \psi^* \qquad (3.7)$$

Rearranging terms, the left hand side becomes:

$$-2ik \frac{\partial I}{\partial_z} = \psi^* \nabla_r^2 \psi + \psi \nabla_r^2 \psi^* \qquad (3.8)$$

After substitution the (3.1) and (3.2) in to the right hand side of (3.8), the TIE (3.9) can be obtained as follows:

$$\nabla_r \cdot [I(\vec{r}_\perp, z)\nabla_r \varphi] = -k \frac{\partial\ I(\vec{r}_\perp, z)}{\partial_z} \qquad (3.9)$$

The TIE gives implication that the phase of the wave can be determined from the gradient of intensity of wave along the wave propagation direction.

The intensity is assumed to be non-zero everywhere in the image plane in order to give a unique solution for phase [13]. If the image plane includes points of zero value, where the phase is undefined at these points, the discontinuity yields a multi-valued solution to the TIE.
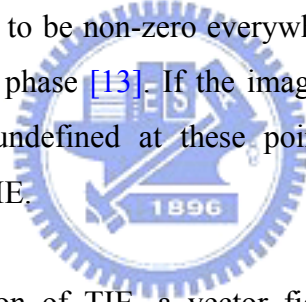
Continuing on the solution of TIE, a vector field can be decomposed into a continuous scalar field $\varphi(r)$ and a vector potential $\upsilon(r)$ as follows.

$$I(\vec{r}_\perp, z)\nabla_r \varphi(\vec{r}_\perp, z) = \nabla_r \xi(\vec{r}_\perp, z) + [\nabla_r \times \upsilon(\vec{r})]_\perp \qquad (3.10)$$

Teague[14] assumes the rotational term $[\nabla_r \times \upsilon(\vec{r})]_\perp = 0$. Thus the function to be rewritten as

$$I(\vec{r}_\perp, z)\nabla_r \varphi(\vec{r}_\perp, z) = \nabla_r \xi(\vec{r}_\perp, z) \qquad (3.11)$$

Here we introduces an auxiliary function ξ that satisfies $\nabla \xi = I\nabla \varphi$ and it leads TIE approximates as an in-homogeneous Poisson type equation. Paganin and Nugent[15] suggested associating with Poynting vector, the TIE reduces to Possion equation.

$$\nabla_r^2 \xi(\vec{r}_\perp, z) = -k \frac{\partial\, I(\vec{r}_\perp, z)}{\partial_z} \qquad (3.12)$$

The auxiliary function ξ can be solved by (3.12), and the phase φ is determined from another Poisson type equation. Substituting $\nabla\xi$ into equation (3.11) yields the relationship between φ and ξ in the Poisson type equation (3.11). After simplifying the notation and expanding the divergence, we write the equation as the follows:

$$\nabla_r{}^2\varphi = \nabla_r(\frac{\nabla_r\xi}{I}) = \frac{1}{I}\nabla_r{}^2\xi + \nabla_r(\frac{1}{I}) \bullet \nabla_r\xi \qquad (3.13)$$

The equation is then substitute by (3.12)

$$\nabla_r{}^2\varphi = \frac{1}{I}(-k\frac{\partial I}{\partial Z}) + \nabla_r(\frac{1}{I}) \bullet \nabla_r\xi \qquad (3.14)$$

This equation is then can be solved by the (Fast Fourier transform) FFT of the computer. The ξ is first solved by the FFT as the following equation.

$$\xi = \frac{-1}{4\pi^2} F^{-1}\{\frac{1}{q^2} F\{-k\frac{\partial I}{\partial Z}\}\} \qquad (3.15)$$

Where the q is the index in the reciprocal domain, which is also know as frequency domain. After ξ is solved, the solution is substitute into the (3.14) for the solution of φ, as written below, the FFT solution for the TIE.

$$\varphi = \frac{-1}{4\pi^2} F^{-1}\{\frac{1}{q^2} F\{(-(\frac{1}{I})\frac{k\partial I}{\partial Z} + \nabla(\frac{1}{I}) \bullet \nabla(\frac{-1}{4\pi^2} F^{-1}\{\frac{1}{q^2}F\{-k\frac{\partial I}{\partial Z}\}\})\}\} \qquad (3.16)$$

In the experiment, the I and $\frac{\partial I}{\partial_z}$ is obtained by taking three images along the propagation direction, which are denoted as I_1, I_2, and I_3. The I_2 is in the middle of I_1 and I_2. The readily solved TIE can be rewritten as the following equations.

$$\varphi = \frac{-1}{4\pi^2} F^{-1}\{\frac{1}{q^2} F\{(-(\frac{1}{I_2})\frac{k(I_3-I_1)}{Z_{31}} +$$

$$4\pi^2(F^{-1}\{q_x(F\{\frac{1}{I_2}\})\} \bullet F^{-1}\{q_xF\{\frac{-1}{4\pi^2}F^{-1}\{\frac{1}{q^2}F\{-k\frac{k(I_3-I_1)}{Z_{31}}\}\}\}\} +$$

$$F^{-1}\{q_yF\{(\frac{1}{I_2})\}\} \bullet F^{-1}\{q_yF\{\frac{-1}{4\pi^2}F^{-1}\{\frac{1}{q^2}F\{-\frac{k(I_3-I_1)}{Z_{31}}\}\}\}\})\}\}$$

(3.17)

The Z_{31} is the distance between I_1 and I_3. The distance from I_1 to I_2 should be equal the distance I_2 to I_3. In order to approximate the derivative of intensity along the propagation direction, the distance should small. However, in the experiment, the signal to noise ratio (SNR) should be high enough to get the difference between I_1, I_2 and I_3 ; the distance should not be too small. Therefore, there is a trade off between the moving distances, which will be explained in later section.

3.2 Self Consistent Wave Propagation (SCWP)

The SCWP is an algorithm of finding the phase by iterative propagation of the wave from sample plane to image plane. The history of this equation is briefly introduced in the chapter 1. This method is currently used in the TEM [3,4] ad TXM [7].

The propagation of waves in free space can be described as the convolution of wave and the propagators. Recalling the section 1.1.2, we have the equation that describes the wave propagating in the free space. The $\psi_2(x,y,z_2)$ is the wave in the z=z_2 and the propagator P_g is $P_g = \exp\{-\frac{i\pi}{\lambda z}[X^2+Y^2]\}$.

$$\psi(x,y,z) = A\psi(X,Y,0) \otimes \exp\{-\frac{i\pi}{\lambda z}[X^2+Y^2]\}$$

(3.18)

This convolution can be done by FFT using a computer. The convolution theorem gives as following.

$$F_{qx,qy}(g(x,y) \otimes h(x,y)) = G(q_x,q_y)H(q_x,q_y)$$

(3.19)

Where the $G(q_x,q_y)$ and $H(q_x,q_y)$ is the Fourier transform of the $g(x,y)$ and $h(x,y)$.

$$\psi(x,y,z) = F^{-1}\{\psi(q_x,q_y)P_g(q_x,q_y)\} \tag{3.20}$$

Where the $P_g(q_x,q_y) = \exp(i\pi\lambda z(q_x^2 + q_y^2))$ (3.21)

This assumes that the microscope is free from other aberrations. This implies that if the $\psi(x,y,z)$ is known, the $\psi(x,y,0)$ can be found by the inverse propagation, which replaces the z in (3.21) as –z. The scheme of SCWP is shown in the figure 3-1 and explained below.
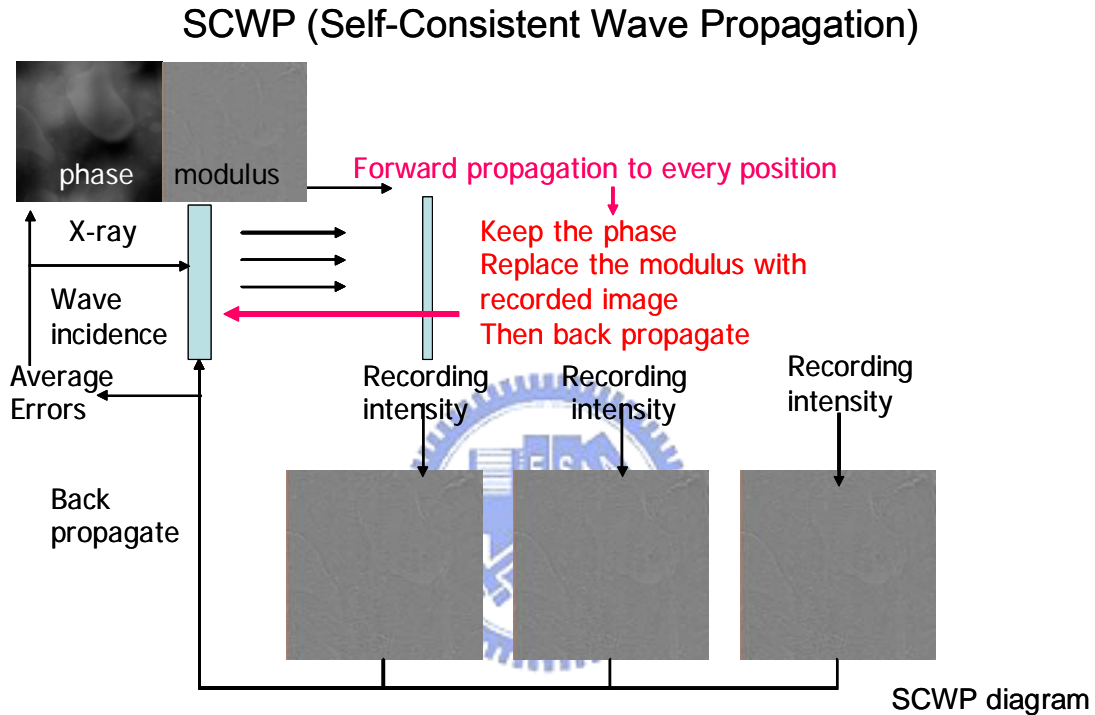

Figure 3-1 The scheme of the SCWP. The images are first recorded at different propagation position. With the initial guess of phase, each position generates an optical wave and then propagates to the position of exit wave. All propagates waves are averaged to get one averaged wave. The average wave then propagates forward to every position where these images are recorded. The phase of each wave is kept, and the modulus is replaced by the recorded image. This is the end of one loop. The scheme of SCWP is explained in detail in the text.

The process of the SCWP utilizes recorded intensities at different positions. The phase in the image plane is needed to transfer back to the sample plane. Thus, the first step of SCWP is to guess the initial phase of image waves in different positions. The zero value of phase is generally used in SCWP. However, exit wave deduced from back propagation of the image waves at different positions is not identical due to the noise and incorrectness of initial phases. All of the exit waves (including modulus and

61

phase) in the sample plane are averaged to be one wave. The averaged wave then propagates to the different position of image planes by different propagators. The modulus of image wave is then replaced by the square root of intensity which are recorded in the experiment. The error can also be calculated from the difference between the modulus of image waves and the square root of intensity of recorded images. The error at each image plane is first normalized by the pixel number and then averaged on all reconstructed images. This is one of iteration of SCWP. The loops repeat itself until the error is less than the preset value.

If iteration is converged, the error value will become smaller and smaller, and the converged phase is approaching one stable value. Otherwise, the error value becomes larger and larger and the phase is unstable.

3.3 Combination of TIE and SCWP for Phase Retrieval

The TIE and SCWP are different approaches for the phase retrieval, and they have different response in frequency space. In general, the TIE is good at low spatial frequency and SCWP is good at high spatial frequency. The details will be explained in the following sections.

3.3.1 The different response of TIE and SCWP

In general, SCWP is more efficient to recover the phase information for smaller object which has significant signal in higher frequency domain (larger q), since the phase factor of the propagator $\pi\lambda\Delta fq^2$ is larger in high frequency domain. For large object whose signal concentrating in the lower frequency regime (small q), the SCWP may not work well due to small phase factor in propagator. In this case, a sample contains objects of very different size such as those of the test zone plate; the efficiency of the phase recovery may vary the size of object in the sample. This deficiency can be clearly observed in our retrieval using SCWP alone.

On the contrary, TIE is suitable to process relative large objects whose signal concentrating in lower frequency regime. As we can see that the $1/q^2$ factor in TIE equation (3.17) amplifies the low frequency (small q) signal and suppresses the high frequency signal. The simulated sample is used to illustrate the idea easily. The simulation condition is at 8 keV, field of view of 15μm, and the phase advance is set to 0.17 radian, which is the same as the experiment, will be shown in the later section.

Simulation by the Contrast Transfer Function (CTF) for wave propagation

To analyze the phase contrast, the intensity for a weak phase and absorption object can be expressed by the approximation equation:

$$\psi(u,v,z) \approx \delta(u,v) + m(u,v)\cos(\pi\lambda z(u^2+v^2)) + \Phi(u,v)\sin(\pi\lambda z(u^2+v^2))$$

in the reciprocal space.

Where $\psi(u,v,z)$ is the Fourier transform of wave function at distance z. The $\pi\lambda z(u^2+v^2)$ is phase of the propagator, which will be explained later. In this formula, the contrast repeats itself with certain period in wavelength, Z (propagation distance) and frequency, which is in the order $q\sqrt{\lambda z}$. In the figure 3-2(a), we show a a zone plate like concentric pattern, which is used to simulate the wave front modulation with different spatial frequency. The wave is assumed to compose with uniform modulus and modulated wave front (phase). In figure 3-2 (b-d), the contrast varies with the spatial frequency and distance. In figure 3-2(b), the factor of $q\sqrt{\lambda z}$ is small, where z is 5 μm, and the contrast is mostly dominated by absorption contrast. The contrast of images becomes higher while the propagation distance increases, as shown in the figure 3-2 (c), where z is 100 μm and the period of the contrast can be seen. The period becomes half of the period in 100 μm for the z is 200 μm. This CTF give a hint that the best phase contrast can be found according to wavelength, the covered spatial frequency and the propagation distance. The simulation conditions are the field of view of 15 μm, pixel size 0.15 nm, wave length 0.155 nm and phase advance of 0.17 radian. In the free space, the Cs (coefficient of spherical aberration) is not considered. However, the aberration in the TXM is influenced by the structure of the zone plate and condenser.
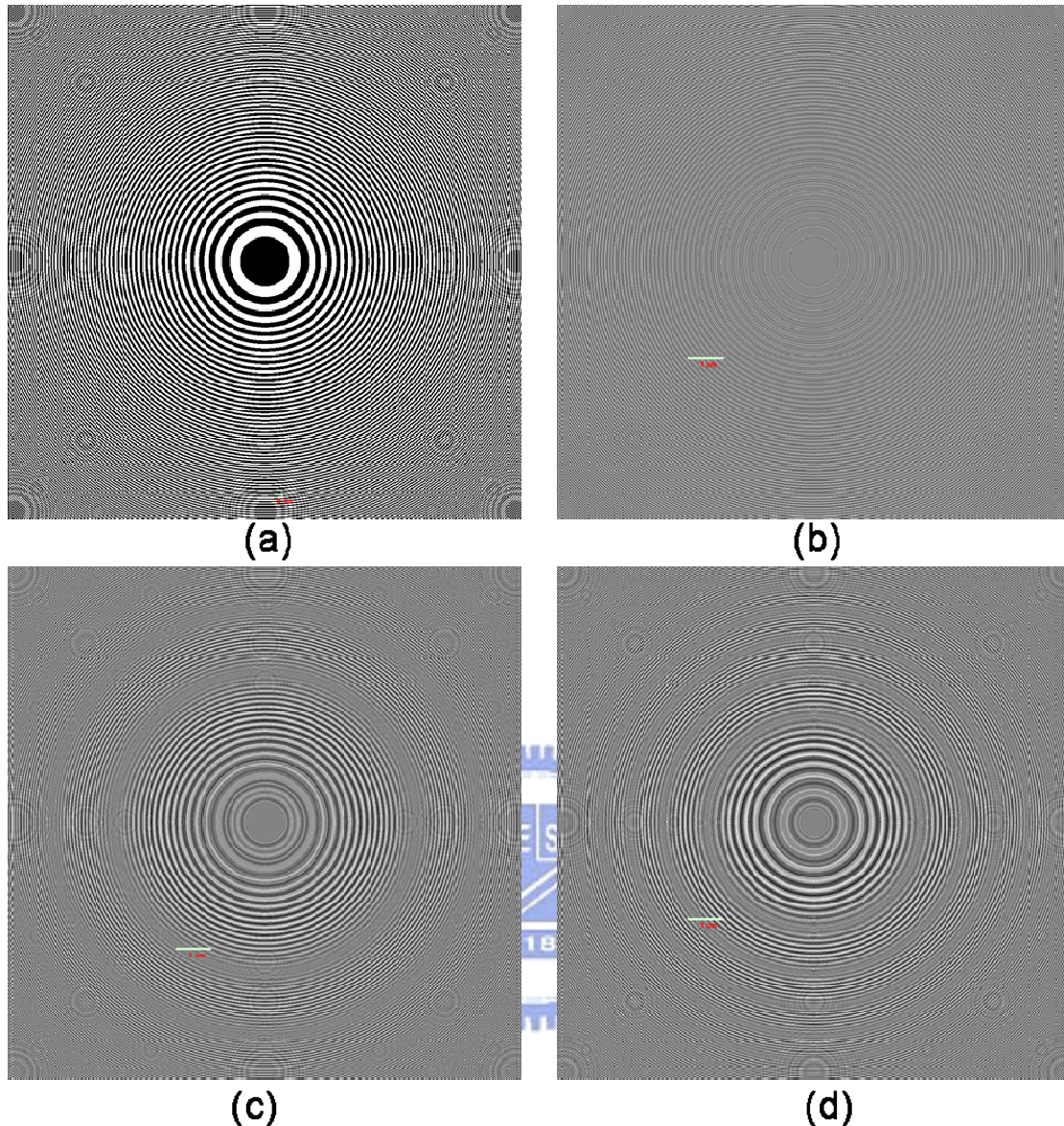
Figure 3-2 The intensity simulation of a wave concentric phase retardation with propagation different position. (a)initial phase front (b) propagation distance 5 μm (c) propagation distance 100 μm (d) propagation distance 200 μm**.**

The retrieved phases from simulated image by TIE and SCWP are compared. Figure 3-3 shows the retrieved phase map of the test phase plate using simulation image pairs at distances of ±400 μm. In figure 3-3, the failure of the TIE process to retrieve phase recovery at high frequency has been demonstrated, and the simulation using a zone-plate –like structure – it has variable line width/spatial frequency to test the frequency response of the phase retrieval methods– at the same condition in the experiment, and we found the cut-off frequency is around 2.7 line/um. The phase retrieved by SCWP and TIE is shown in figure 3-4. The red line indicates the retrieved phase by SCWP, and blue line indicates the retrieved phase by TIE. These

two methods have different response with spatial frequency. It verifies the different frequency response of TIE and SCWP. Here we have proposed a combined method to solve phase efficiently, the response of the combine method is as shown in the green in figure 3-4, and the details of the method will be explained later.
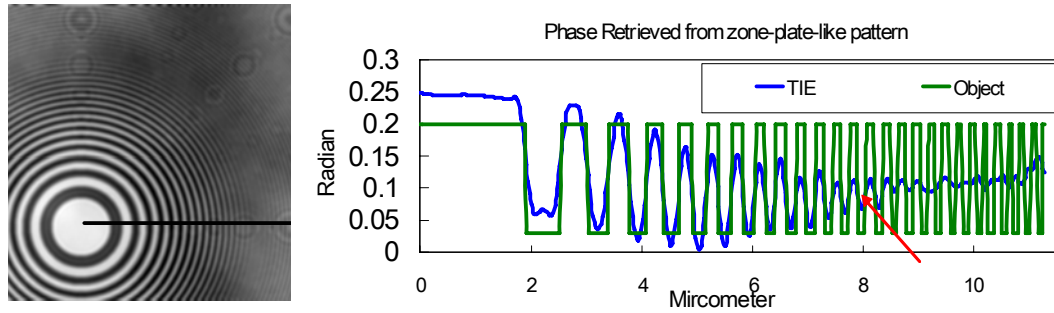

Figure 3-3 The retrieved phase by TIE for a zone-plate-like pattern. We have the small response around 0.3 μm period (position at 8 μm, as indicates by red arrow), which represents the incoherent upper bound of the TIE.
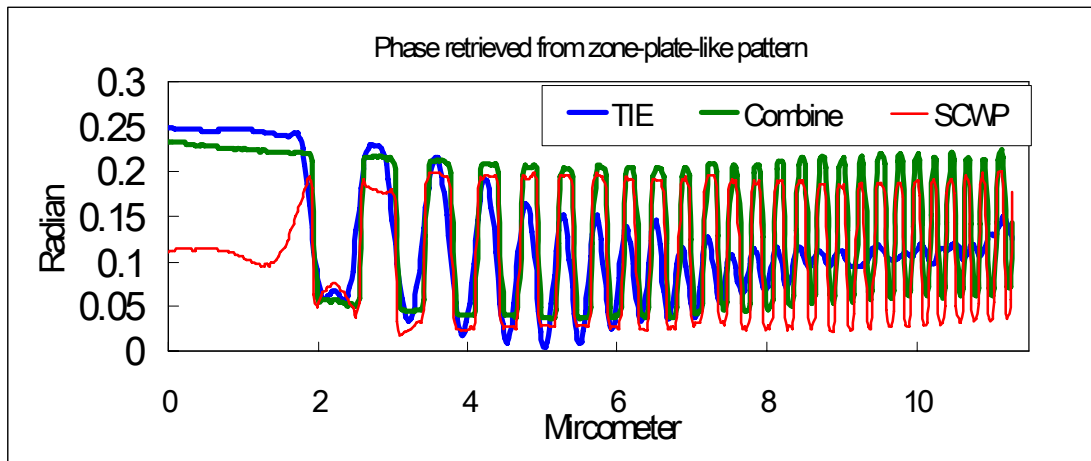
Figure 3-4 The retrieved phase by TIE (blue), SCWP (red), and Combine (green) methods for a simulated zone-plate-like pattern as depicted in figure 3-3. The SCWP has low response in the low frequency and TIE has higher frequency.

3.3.2 The Applicable range of TIE and SCWP

From the wave propagator (3.18), the parameters which affect the CTF are the propagation distance and field of view. Therefore, it is important to understand the applicable range for propagation distance and field of view (pixel size) with the specific wave length of the wave, which is shown in the figure 3-5. The horizontal and vertical axes in figure 3-5 are frequency and propagation distance, respectively. The parameters of this plot are the same as the experiment condition, which is at 8 keV, field of view of 15 μm, and the phase advance is set to 0.17 radian. Not all of the range is suitable for phase retrieval. For example, the longer propagation distance might fall into the range of the Fraunhofer range, which is not suitable for retrieve phase by SCWP and TIE because the phase is wrapped too many times as explained in the section of CTF. Moreover, if the propagation distance is too short, the change of intensity might be too small to make the intensity difference between two adjacent images.

For the applicable bounds in this figure, they are TIE upper bound, TIE lower bound, TIE incoherent upper bound, SCWP lower bound and SCWP incoherent upper bound. TIE and SCWP lower bound is mainly because the signal is not strong compare to the level of noise. TIE upper bound is due to the approximation of the TIE is failed while the propagation distance is too long. SCWP incoherent upper bound is because the spatial incoherence blurs the details while the propagation distance is too

long. The details of the description of the bounds can be found in the previous publish [16]. The applicable range for the TIE and SCWP is limited by the five bounds. For example, to choose the best condition, one has to find out the larges area that inside the applicable range (in green are in figure 3-5).

The error value is written as below.

$$Error = \frac{\sum_{ny=0}^{n} \sum_{nx=0}^{m} (P'_{original}(nx,ny) - P'_{solved}(nx,ny))^2}{m \times n} \tag{3.22}$$

The error is to calculate the difference between the solved phase ($P'_{solved}(nx,ny)$) and original phase ($P'_{original}(nx,ny)$). Thus, the $P'_{original}(nx,ny)$ is the phase at certain nx,ny in the digitized image $P'_{original}$, where the nx, ny are the integers. The $P'_{solved}(nx,ny)$ is the solved phase at image plane. "*m*" and "*n*" are the pixel number of the both digitized images of $P'_{original}$ and P'_{solved} in horizontal and vertical, respectively. The applicable region for the TIE and SCWP is different. The applicable range of TIE is suitable in the shorter propagation distance and smaller spatial frequency, while that of SCWP is in longer propagation distance and higher spatial frequency. For phase retrieve, it is important to have most of the spatial frequency in the image fitted in the applicable range. Thus, a new phase retrieval scheme is proposed and demonstrated in the next section.
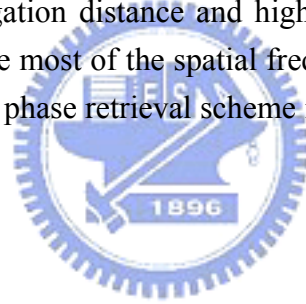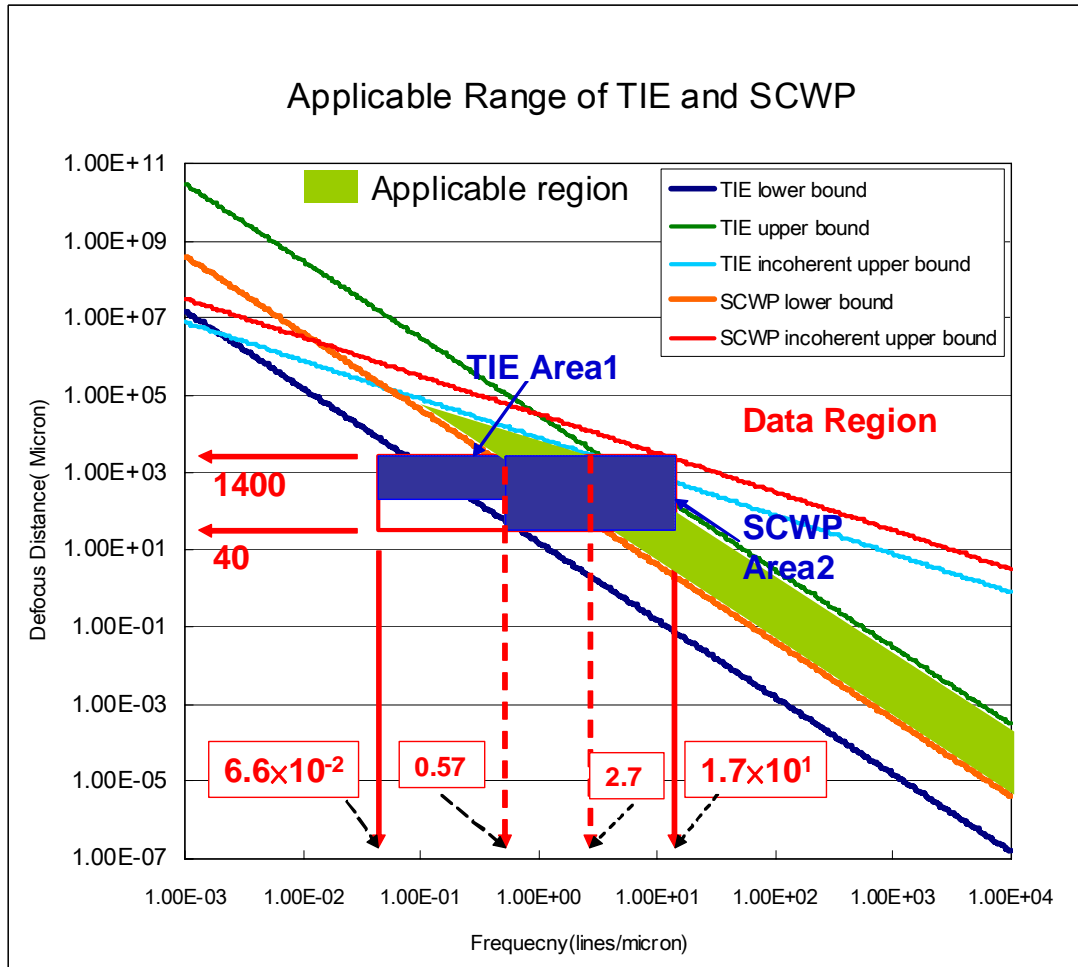
Figure 3-5 The applicable range for TIE and SCWP. For SCWP, the upper bound is set by the spatial incoherence, depicted as red line. The lower bound is set by the phase factor in propagator $\pi\lambda\Delta fH^2$, depicted as cyan line, where λ is the wavelength and Δf is the focal distance. For the TIE, the lower bound is determined by the noise, shown as dark blue, while the spatial incoherence, shown as the cyan line and the separation of image planes are responsible for the upper bounds, shown as the green lines, these lines are given by [Ref 12]. The applicable range is the light green area.

3.3.3 Phase retrieval by combination of TIE and SCWP

The proposed algorithm for new phase retrieved algorithm is to combine the TIE and SWCP. One advantage for this scheme is that most of the spatial frequency will locate in the applicable range. In figure 3-5, the object has the spatial frequency region from 6.6×10^{-2} to 1.7×10^{1} lines/μm. In order to cover the all the spatial frequency in the applicable region, both of the phase retrieval methods will be used in this scheme.

68

The combined algorithm is to retrieve the phase is to use the solution from TIE as the initial guess of SCWP which has low response to low frequency. In figure 3-4, the phase retrieved by SCWP in low frequency is unchanged compare to low frequency, thus, the phase of low frequency will not altered in SCWP and maintain its status. With this method, the low frequency and high frequency can be retrieved and preserved in the applicable region. In figure 3-5, the applicable lower limit for SCWP is 0.57 lines/μm, and the incoherent upper bounds for TIE is 2.7 lines/μm. After the combination, the applicable range can be extended and the profile of the retrieved phase by the integrated application of two methods is shown as green plot (the "combine") in the figure 3-4.

3.4 The Quantitative Phase Retrieval in Transmission X-ray Microscope

The focal length of our TXM is 27mm for the energy of 8 keV with a magnification of 45. The focal spot of the condenser lens is ~ 50 μm, and the convergence angle of the condenser is ~ 0.18 mrad. The field of view at the objective plane is 15 μm × 15 μm. The depth of focus is estimated from ~ 80 μm. By moving the sample along the x-ray propagation direction, a defocus series images can be recorded. However, moving sample is different from the theorem we have described in the previous section. In the subsection one (3.4.1) will prove that: this sequence is equivalent to the sequence that would be obtained by changing the distance of detector plane with a multiplication factor M^2, where M is the magnification of the TXM, if the defocus distance is small compare to object distance and image distance. In the subsection two (3.4.2), the experimental results will be demonstrated and analyzed.

3.4.1 Applying phase retrieval in TXM

According the wave theorem, a single lens system can be express as the following equations. The scheme of a single lens system is shown in figure 3-6.
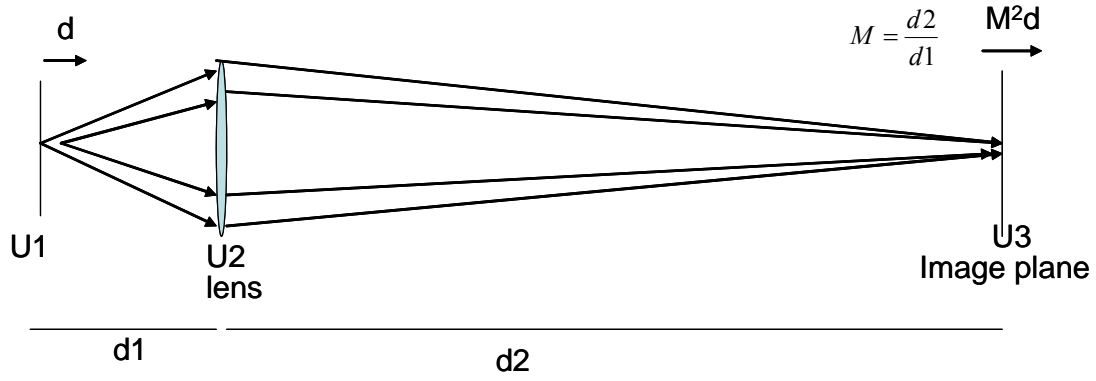
Figure 3-6 The optical system of a single lens system. U1 is the optical wave at the sample plane, U2 is the lens and U3 is the optical wave at detector plane.

The image in U3 can be written as the following equation, according to the Fresnel optics. The notation in (3.23) can be found in the figure 3-6. "d1" and "d2" are the distance from sample plane to the lens and from lens to the image plane, respectively.

$$U3(x_3, y_3) = \iint U1(x_1, y_1) U2(x_2, y_2) \exp(-i\frac{k}{2d_1}[(x_2 - x_1)^2 + (y_2 - y_1)^2]) \exp(-i\frac{k}{2d_2}[(x_3 - x_2)^2 + (y_3 - y_2)^2]) dx_1 dx_2 dy_1 dy_2$$

(3.23)

U2 is the single lens, with the spherical surface, as written in (3.24)

$$U2(x_2, y_2) = \exp(\frac{ik}{2f}(x_2^2 + y_2^2))$$

(3.24)

Substitute U2 into the (3.23), the $(x_2^2 + y_2^2)$ vanished because the lens formula. The equation is rewritten as:[17]

$$U3(x_3, y_3) = \exp(-i\frac{k}{2d_2}(x_3^2 + y_3^2)) \iint U1(x_1, y_1) e^{-i\frac{k}{2d_1}(x_1^2 + y_1^2)} e^{i\frac{k}{d_1}(x_2 x_1 + y_2 y_1) + i\frac{k}{d_2}(x_3 x_2 + y_3 y_2)} dx_1 dx_2 dy_1 dy_2$$

(3.25)

It can be treated as one Fourier transform and one inverse transform with different pixel size, as shown in (3.26)

$$U3(x_3, y_3) = \exp(-i\frac{k}{2d_2}(x_3^2 + y_3^2)) F^{-1}\{F\{U1(x_1, y_1) e^{-i\frac{k}{2d_1}(x_1^2 + y_1^2)}, f_{x1} = -\frac{x_2}{\lambda d_1}, f_{y1} = -\frac{y_2}{\lambda d_1}\}, f_{x2} = \frac{x_3}{\lambda d_2}, f_{y2} = \frac{y_3}{\lambda d_2}\}$$

(3.26)

Thus, we have the as written below

$$U3(x_3, y_3) \approx \exp(-i\frac{k}{2d_2}(x_3^2 + y_3^2)) U1(Mx_1, My_1)\Big|_{M = -\frac{d2}{d1}}$$

(3.27)

Here U3 is the wave in the detector plane.

In the deduction of the image theorem, the phase difference in the middle term
$\Delta P = (x_2{}^2 + y_2{}^2)(\frac{1}{d_1} + \frac{1}{d_2} - \frac{1}{f}) = 0$ makes the all integrals becomes two Fourier
transforms. The image is defocused because this term is not valid and phase
difference is estimate based on this formula. Recalling the phase retrieval theorem
described in pervious section, the image sequence is taken for different detector
positions instead of the different object position. Thus, the phase differences between
moving the detector and object are compared. The phase difference induced by
moving a distance "d" of detector is calculated as followings.

$$\frac{\Delta P_{d2}}{(x_2{}^2 + y_2{}^2)} = \frac{1}{d_2} - \frac{1}{d_2{}'} = \frac{1}{Md_1 + d} - \frac{1}{Md_1} = \frac{-(Md_1 + d - Md_1)}{Md_1(Md_1 + d)} = \frac{-d}{Md_1(Md_1 + d)} \approx \frac{-d}{M^2 d_1{}^2}$$

(3.28)

The phase difference induced by moving a distance "d" at the sample plane is

$$\frac{\Delta P_{d1}}{(x_2{}^2 + y_2{}^2)} = \frac{1}{d_1} - \frac{1}{d_1{}'} = \frac{1}{d_1 - d} - \frac{1}{d_1} = \frac{(d_1 - d_1 + d)}{d_1(d_1 - d)} = \frac{d}{d_1(d_1 - d)} \approx \frac{d}{d_1{}^2}$$

(3.29)

Form equation (3.28) and (3.29), the factor of M^2 for moving sample compare to
moving detector is proved. From equation (3.29), the phase difference is positive.

3.4.2 Experimental result and analysis

A plastic (PMMA) zone plate of 1μm thickness is used as the test sample for
phase retrieve, as shown in figure 3-7. An X-ray image of this zone plate recorded at
focus value is shown in figure 3-7 (a). The δ is -4.18×10^{-6} and β is 9.22×10^{-9} for the
plastic zone plate, which generates the phase advance about 0.17 radian at 8 keV. The
defocus images were aligned and normalized against background taken without
specimen. In order to quantitatively analyze the retrieved phase from the experimental
images, we compare the retrieved phase with that from simulated images of a model
zone plate. The model zone plate, shown in Fig. 1(b), has the same dimension as the
measured zone plate. The phase jump between the white (air gaps) and the dark (the
PMMA) bands is set at 0.17 radian.

Total 70 images were taken from -400 to 980 μm. The interval of each step is
20μm. Three experimental images recorded at the distance of -400, 20 and 980 μm are
shown as examples in figure 3-8 (a), (b) and (c), in which the resulting Fresnel fringes

from defocus can be clearly observed. As shown in figure. 3-8 (d), (e) and (f), the Fresnel fringes in the simulated images of the same optical conditions are in good agreement with experimental images. A 2% of noise in root-mean-square (rms) value was added in the simulated images to facilitate the visual comparison. The convergent angle of $\alpha=1.8\times10^{-4}$ is considered in the simulation.
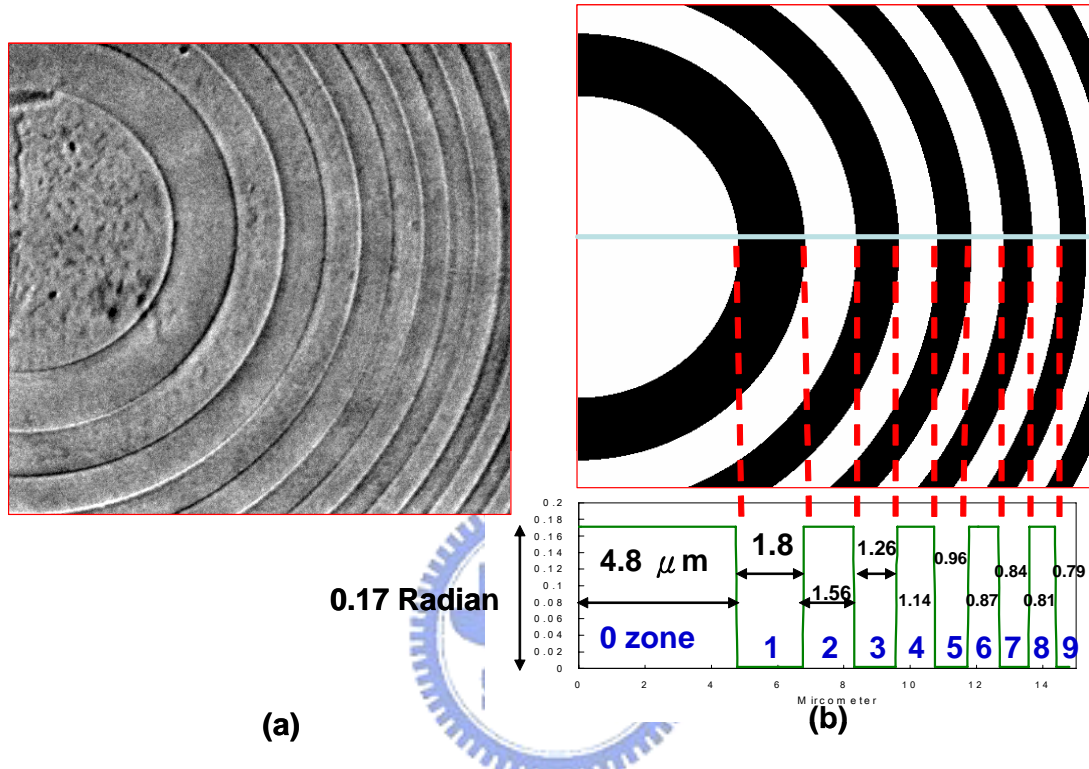

(a)

(b)

Figure 3-7 A plastic zone plate is used as the sample. (a), the TXM image of plastic zone plate recorded at zero focus. The illumination aperture already gives rise to and edge fringe, and therefore the image does not contribute completely from absorption. (b) A model zone plate, where the white and dark bands correspond to open and PMMA structures, respectively. The phase jump between the while and the dark band is calculated to be 0.17 radian. The width of each band is given in the figure. The visible field of view is 15 μm.
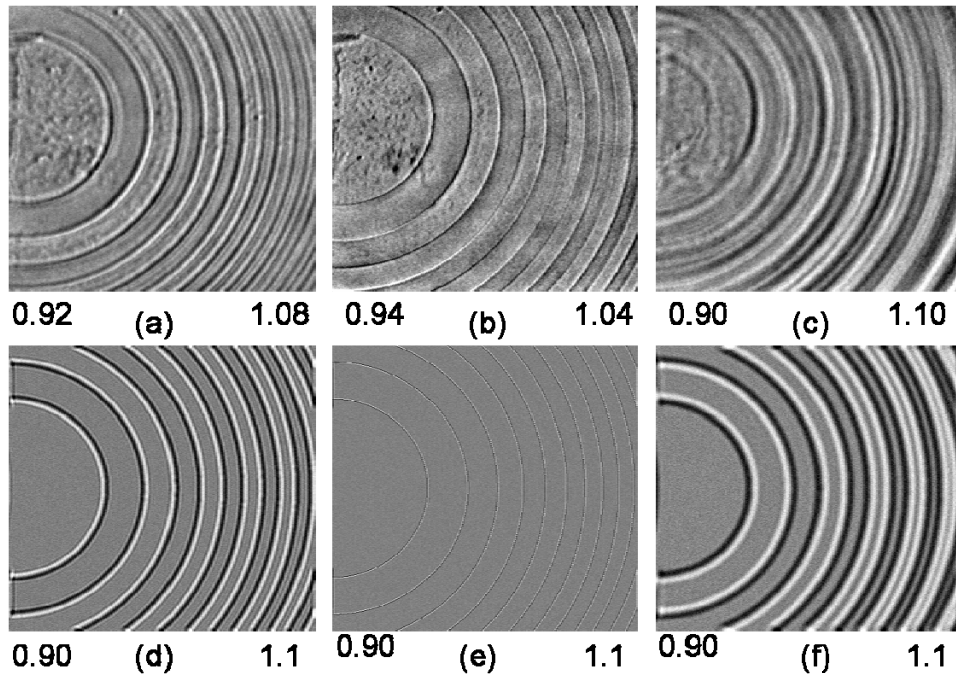
Figure 3-8 The experimental and simulated images of TXM. The images in top row (a), (b) and (c) are experimental images taken at position of -400μm, 20μm, 980 μm from left to right, respectively. The bottom row shows simulated images of the model zone plate at -400μm, 20μm, and 980 μm from left to right (d), (e) and (f). The simulation condition is with the convergent angle $\alpha=1.8\times10^{-4}$ with 2 % noise. The values in the bottom of the image are maximum and minimum of the image.

Both TIE and SCWP are algorithms to retrieve the phase from series of recorded intensities of image planes located at equal distance. The retrieved phase by the TIE using experimental image pairs at ± 400 μm served as an initial solution for SCWP to refine. The results of three method, SCWP, TIE and combined method are shown in figure 3-9. The red and blue lines are the line plots of the retrieved phase from the simulated and experimental images. The green plot is the ideal object phase from the model zone plate. In SCWP, the experiment result is agree well with simulation data, has lower response and lower frequency. In TIE, the result has better response for low frequency and in figure 3-9(c), the details of the image are blurred because lower response of high frequency. The result of combined is shown as figure 3-9 (e) and (f). The SCWP therefore improves the phase recovery in higher frequency, while it keeps the phase in lower frequency unaltered. The signal of higher frequency can also be seen from appearance of the fine features of nano-scale particles.
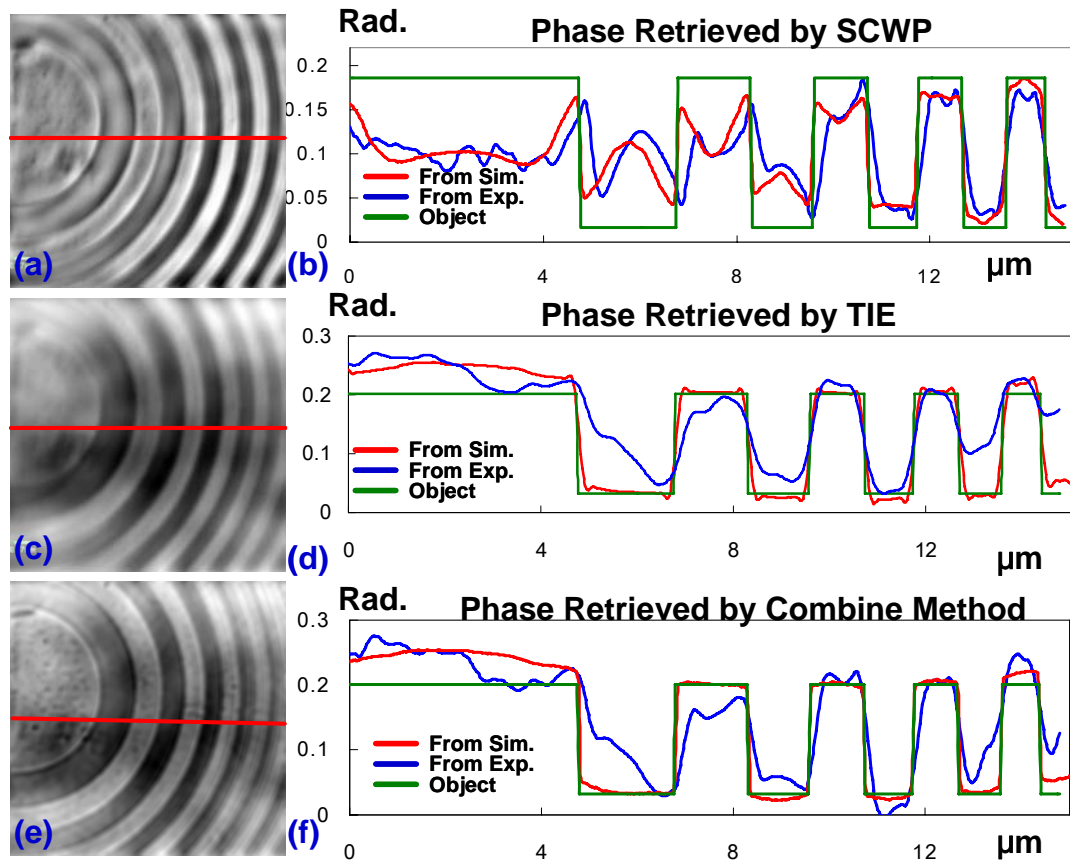
Figure 3-9 The results of three phase retrieval methods, (a)(b) the image and the line plots of phase retrieved by SCWP.(c)(d) the image and the line plots of phase retrieved by TIE. (e)(f) the image and the line plots of phase retrieved by combined method. For the combined method, the retrieved phase image by TIE, as shown in(c), from ±400 μm experimental image pairs was used as an initial solution for SCWP. The red and blue lines are the plot of retrieved phase using from the simulated and experimental images, respectively. The green plot is the ideal object phase from the plastic zone plate.

For SCWP only, plots of the retrieved phase from experimental and simulated images are shown as blue and red lines in figure 3-9 (b). It can be seen that the retrieved phase plots from experimental (blue) and simulated (red) images are almost the same. These two plots show the phase difference of the object size smaller than 1.14 μm, for example, phase difference of silicon nitride (at position of 14μm) and PMMA at 13 μm, match rather well with the ideal phase plot (green) in shape and produced a phase difference value ~0.15 rad. However, the phase difference around the center circle is not well recovered since the information associated with the circle concentrating in the low frequency where the phase factor is rather small. For example, the phase difference of silicon nitride (between 0 to 5μm) and PMMA (5 to 6.5μm) is only about 0.05 rad and is substantial lower than the ideal value 0.17rad.

74

Note that although the SCWP method has a clear advantage over TIE in preserving the high frequency image structures and reducing the noise, it also suffers from the necessity of acquiring many more images. This detrimental effect can be more serious in x-ray imaging when radiation damage is often of great concerns. Our approach can help to reduce the number of images needed in SCWP alone, by removing the most inefficient and inaccurate part of the retrieval of low frequency image structures with a better guess from TIE. It is also feasible that by knowing the feature sizes in the image a priori, the analysis show in figure 3-5 can help us determine the crossover easily and making a sensible division of image in Fourier space into high and low frequency. The TIE and SCWP can then apply separately to achieve a further reduction of image acquisition.

3.5 Summary

In this chapter, we have demonstrated that the methodology and principle of phase retrieval methods of TIE and SCWP, their principle and their application range image analysis. The combined method of TIE and SCWP is proposed and demonstrated that the applicable range can extend to cover large range in frequency domain. Our experiment showed that, with the combined method, quantitative phase retrieval can be achieved by zone plate type transmission X-ray microscope at a field of view of 15 μm with a resolution of sub-100 nm.
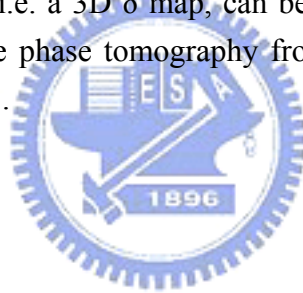
Chapter 4

Zernike Phase Imaging and Phase Tomography

The Zernike phase contrast is invented by Frits Zernike around 1930-40s [1]. The method is applied to observe the imaginary part of a wave to enhance the visibility of weak and thin objects that usually give only low contrast in the optical microscope. The Zernike phase contrast method is a direct way to visualize the contrast contributing from phase and was been used for over half century in various field. F. Zernike received Nobel prize in 1953 for the impacts of phase contrast imaging to science and medicine.

To further realize the phase tomography, the quantitatively phase retrieval which provides the value of wave shift from which the integration of real part of the reflectivity, δ, along the beam path can be deducted. The phase shift generated by the integration of δ is similar to the absorption which is associated with β in the material. Thus, the phase tomography, i.e. a 3D δ map, can be calculated by the filtered-back projection (FBP) method. The phase tomography from simulation and experimental data is discussed in section 4.3.

4.1 The Zernike Phase Contrast Imaging in TXM

In comparison to the phase retrieval method based on wave propagation as presented in chapter 3, Zernike phase contrast can achieve higher S/N ratio with single image. It greatly reduces the exposure time and the radiation dose, which is a promising way for imaging live biological cells. However, the Zernike phase contrast image does not directly give phase of the object wave. Thus, we develop a method based on phase plate with a known structure to quantitatively retrieve the pure phase information from the Zernike phase contrast image. The applicable range and limitation of this method are analyzed. A test sample of plastic zone plate was used to verify this phase retrieved method.

The Zernike phase contrast is generated by the interference between the diffracted and un-diffracted light. In this method, a phase plate inserted in the back focal plane in the system is used for retardation or advance of the phase of un-diffracted wave. The un-diffracted wave is a spot at the center of the back focal plane if the luminance is parallel into the system. In our x-ray microscope system, the luminance is cone-beam type, which results in a ring shape area for zero-frequency (DC) in the back focal plane.

A schematic drawing of Zernike phase contrast imaging of our TXM is shown in figure 4-1. The phase ring is covered with the first diffraction order of the zone plate as illustrated in the figure. In this scheme, only first order diffraction from the zone plate participates in the image for phase contrast. All other higher order diffraction of zone plate will be filtered out. The diffraction intensity of the zeroth and first order beam in the back focal plane is shown in the lower left inset. The un-diffracted beam from the sample is at the path of first order diffraction, and diffracted beam from the sample distribute along the path of first order. The further is the beam, the higher spatial frequency it has. The simplified intensity I(r) for thin phase object of Zernike phase contrast can be simply written as [2]:

$$I(r) = |C|^2 \, (a^2 + 2\{1 - a\cos\alpha - \cos[\phi(r)] + a\cos[\alpha - \phi(r)]\}) \qquad (4.1)$$

where $\phi(r)$ is the phase of the object, α is the phase retardation/advance of the phase ring, a is the transmission of the phase ring. It is understood simply that the maximum phase contrast occurs while the $\sin\alpha$ is equal 1 or -1. In other word, the optimized phase retardation/advance is $\pi/2$ or $3\pi/2$.
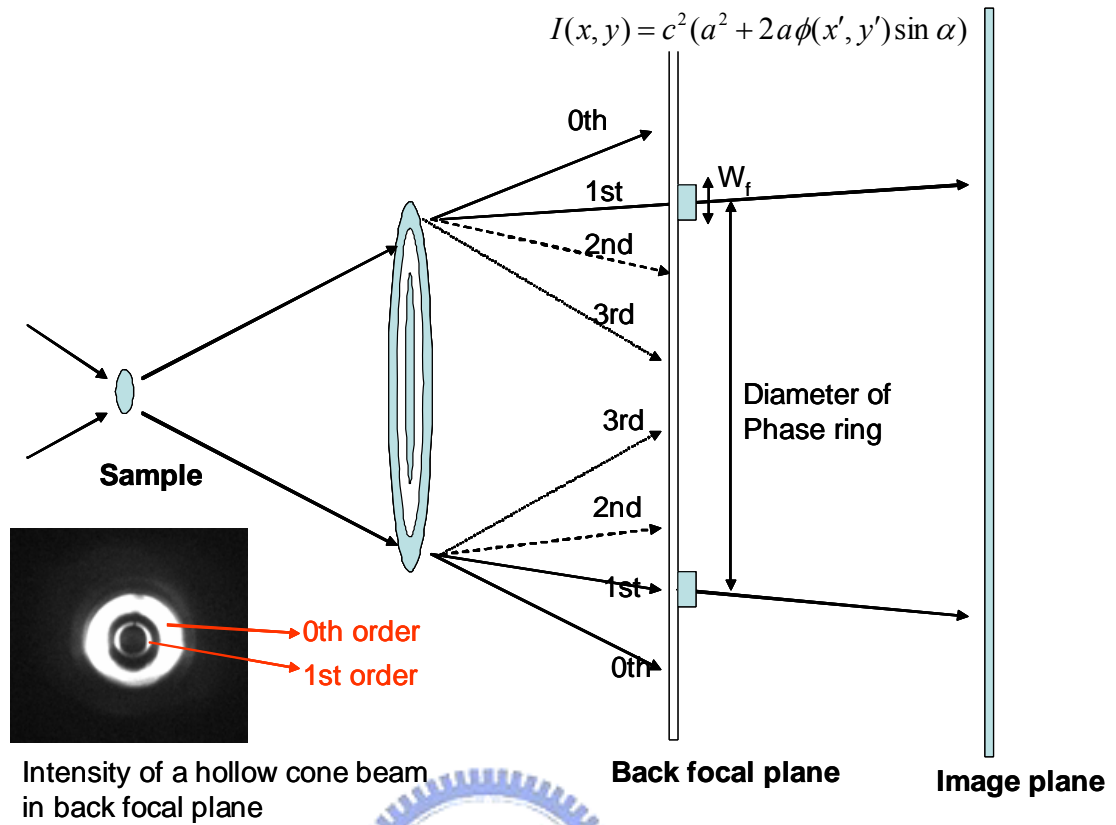
Figure 4-1 The schematic drawing of optics for Zernike phase contrast imaging in TXM.

The Phase Ring

In our TXM the key element of phase imaging is the phase ring, which is made of gold electroplated on silicon nitride membrane using e-beam or generally lithography technology.   The optimum thickness for negative phase shift ($\sin\alpha = -1$) for the phase plate/ring of gold for 8 keV X-rays ($\delta=4.7\times10^{-5}$ and $\beta=4.7\times10^{-6}$) is about 2.5 μm.   The structure of phase ring is shown in figure 4-2. The effect of width, thickness of the optics, and detail principle of Zernike phase ring will be explained in detail in the following sections.
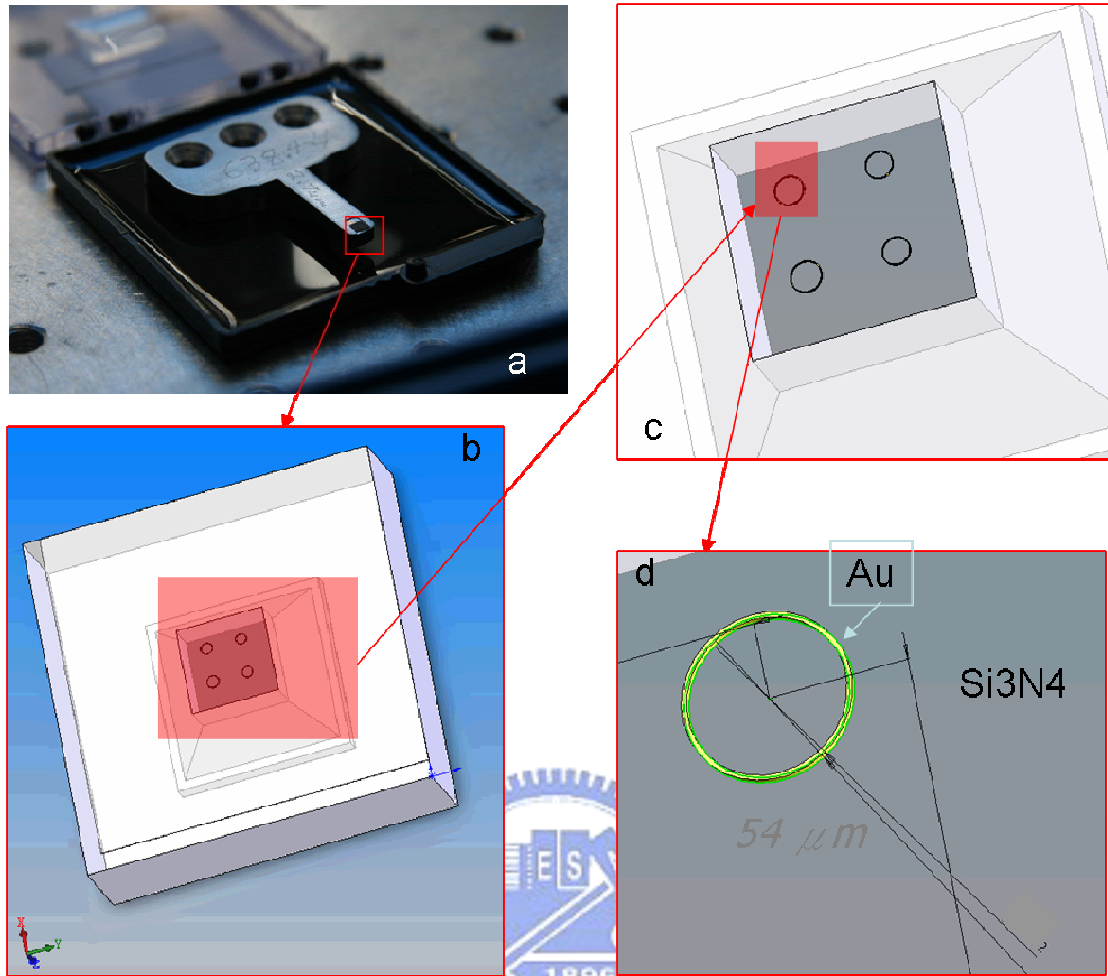
Figure 4-2 The out look of the phase ring. (a) The phase ring on the phase ring holder. (b) The drawing of a phase ring. The phase ring is made of gold, which is deposited on the substrate of silicon nitride (c) The enlarged view of (b). (d) The phase ring structure. The diameter of the phase ring is about 54 μm.

Cell Imaging

The enhancement of X-ray imaging in cell samples was studied using the above setup. We demonstrated that our microscope is able to image the cell with or without stain, as shown in the figure 4-3 (a) and (b). There is no absorption contrast for these samples.
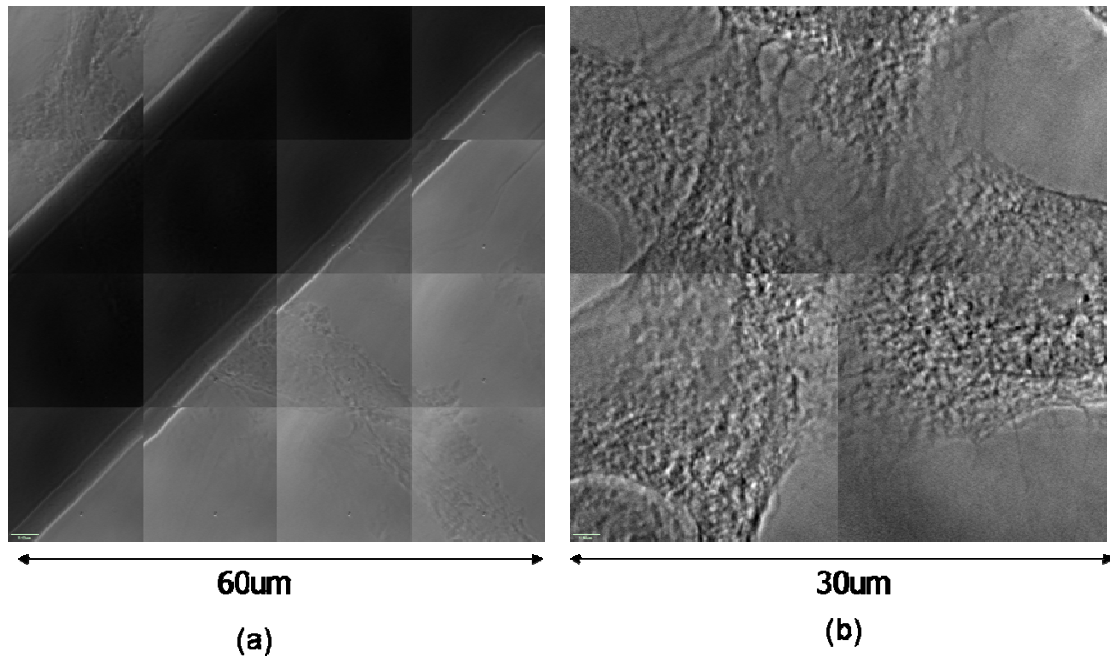
Figure 4-3 The phase contrast images in TXM at 8 keV. (a) The rabbit's muscle cell without stain. (b) The HeLa cell with Ni stained. The internal structures of HeLa cells are clearly observed.

4.2 Iterative Phase Retrieval for Common Path Interferometry (IPR-CPI)

The phase contrast imaging can be directly visualized by the common path interferometery (CPI), such as Zernike phase contrast plate (with phase shift of $\pm\dfrac{\pi}{2}$) [1], Henning phase contrast plate ($\pm\dfrac{\pi}{4}$) [3], or general phase contrast plate (π) [4]. The CPI also includes dark central ground [5] and field absorption interferometers [6]. The CPI was studied for visibility, irradiance, and also optimized methods in the publications [6]. The limitation for unambiguous phase-to-intensity mapping was also studied and method for covering a whole 2π range was proposed [7]. In these studies, η , the ratio of width of the Fourier plates and the distance to the first zero of the system Airy pattern, should be smaller or around 0.4~0.6 in order to have uniform illumination of reference beam and prevent the artifacts of interference pattern. However, it is hard to fabricate such phase plates in the electron microscope or hard x-ray microscope system, in which the η is several times larger than the required value. In this case, the phase to intensity mapping is no longer linear because the loss of the low frequency of phase information.

The motivation of this work is to provide a quantitatively stable method to

81

retrieve phase map from 2D intensity. The proposed method utilizes an iterative algorithm to retrieve the phase with a known structure of the Fourier plane and the recorded interference image. After the 2D phase information is retrieved, the information can be further processed in 3D if more projections of phase image are recorded. This work will be a stepping stone for the phase tomography. The main applications of this method are the phase retrieval in both transmission electron microscope (TEM) and transmission x-ray microscope (TXM).

4.2.1 The process of common path interferometer (CPI)

The process of quantitative phase retrieval with CPI is an iterative algorithm to retrieve the phase of in sample plane. With a known structure of the phase plate, the mathematic model of optical process can be approached as the following. According to the Abbe theorem in microscope, a perfect microscope does two Fourier transforms; one at back focal plane and the others is at the image plane [2]. The CPI in the general microscope is shown in figure 4-4. The CPI plays a role of alternating the modulus and phase of the wave at the back focal plane. Thus, in a 4f image system with assumption of unit magnification, the process of CPI can be written as the equation (4.2).

$$
\begin{aligned}
C\{E_{object}(r)e^{i\phi_{object}(r)}\} &= F^{-1}\{F\{E(r)e^{i\phi(r)}\} \times P(g)\} \\
&= E_{image}(r')e^{i\phi_{iamge}(r')}
\end{aligned}
\tag{4.2}
$$

The tranformation from the object plane to the image plane can be written as equation. (4.2) by ingoring the aberration arising from the defects of the zone plate. In equation (4.2), $E_{object}(r)e^{i\phi_{object}(r)}$ is the exit wave of the object. The $E_{object}(r)$ and $\Phi_{object}(r)$ are the amplitude and phase of the exit wave, respectively. The C is denoted as a CPI transformation, and F is the operation of Fourier transform (FT).

At the figure:

$r_{fbp}(q) = fA(q) \approx f\dfrac{\lambda}{d} = f\lambda q$

$angle = \dfrac{\lambda}{d} = \lambda q$

W_f

f

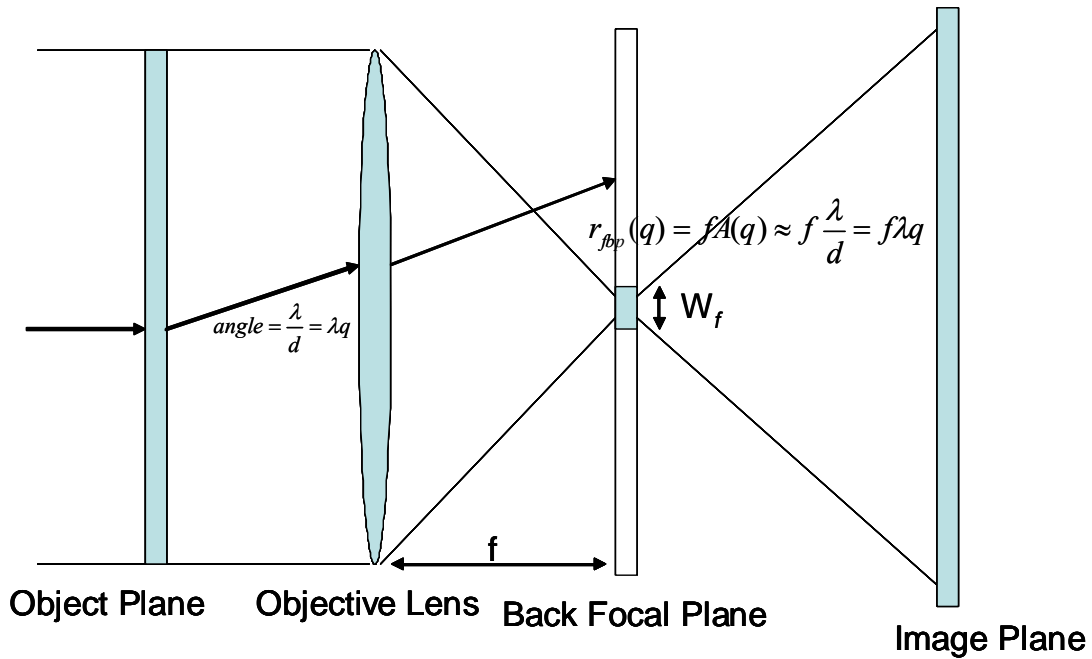**Object Plane**   **Objective Lens**   **Back Focal Plane**   **Image Plane**

Figure 4-4 The common path interferometer in the microscope. According to the Abbe's theorem, a perfect lens system dose two Fourier transforms. The phase plate is placed at the back focal plane, so that the image is the convolution of the object plane and the Fourier transformed of the phase plate.

As we can see from the equation (4.2), the wave in the back focal plane is the Fourier transformation of exit wave but is modified by the complex function of the Fourier plate. The wave in the image plane can be obtained by inverse Fourier transform of the wave in back focal plane and can be written as $E_{image}(r')e^{i\phi_{image}(r')}$,where the $E_{image}(r')$ and $\Phi_{image}(r')$ are the amplitude and phase of image, respectively. In the image plane, only the intensity can be detected, the phase information is lost, thus $I_{image}(r') = [E_{image}(r')]^2$. W_f is the width of Fourier plate which corresponds to a cut-off frequency g_c given by

$$g_c = W_f/2\lambda f \qquad (4.3)$$

The λ is the wavelength and f is the focal length of the objective lens.

The phase plate in our TXM is a Zernike phase ring as shown in figure 4-1. The phase ring is made of gold thin film of width W_f supported by the silicon nitride membrane. The function of a general phase plate can be expressed as follow.

83

$$
\begin{cases}
\left. P(g) \right|_{g \le \frac{w_f}{2\lambda f}} = a e^{i\phi(g)} \\[2em]
\left. P(g) \right|_{g > \frac{w_f}{2\lambda f}} = b
\end{cases}
\tag{4.4}
$$

The "a" and "b" in the equation (4.4) is an amplitude damping factor (transmission) that is related to the absorption of the gold and silicone nitride thin films that phase plate is made up, respectively. For example, the "a" is equal to 0.5646 which corresponds to transmission of gold having thickness of 3.0 μm. The "b" is the transmission of supporting membrane substrate which is made of 0.3 μm of silicon nitride and is approximated to be 1. $\Phi(g)$ represents the phase shift introduced by the Au film which is close to -1.8π in our case. The equation (4.4) suggests that both of the mplitude and phase of exit wave will be modified by the phase plate when frequency of exit wave is lower than g_c. The λ is the wavelength and f is the focal length of the objective lens.

This equation (4.5) also suggests that the exit wave of object can be recovered with a reverse CPI transformation, once the $e^{i\phi_{iamge}(r')}$ and $E_{image}(r')^2$ are known. The inverse CPI transform is denoted as C^{-1}, as written in equation (4.5). The "a" should be non-zero anywhere to insure the reverse transform.

$$
\begin{aligned}
C^{-1}\{E_{image}(r')e^{i\phi_{iamge}(r')}\} &= F^{-1}\{F\{E_{image}(r')e^{i\phi_{iamge}(r')}\} \times \frac{1}{a}e^{-i\phi(g)}\} \\
&= E_{sample}(x,y)e^{i\phi_{sample}(r)}
\end{aligned}
\tag{4.5}
$$

For example, a phase ring with the width of 2 μm, the thickness of 3 μm and the focal length with 2.7 cm can be approximated by the following modulation as shown in the figure 4-5.
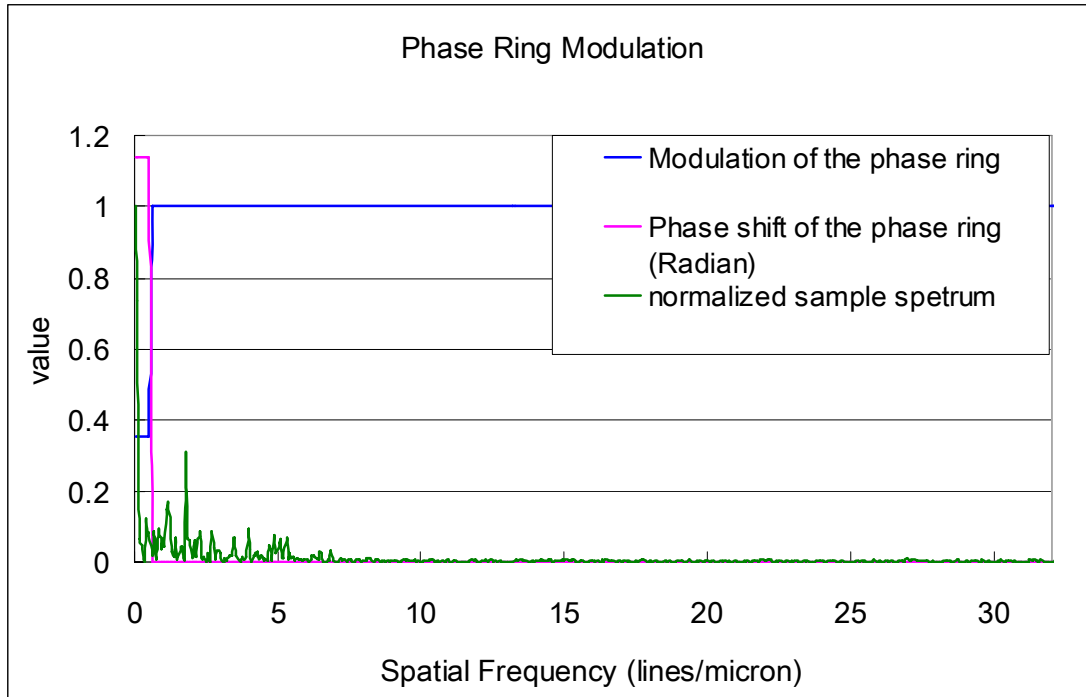
Figure 4-5 The modulation of the phase ring in the back focal plane (BFP). The blue and red lines are the intensity and phase modulation of the phase ring, respectively. The green line is the normalized spectrum. The parameters of the simulated phase ring are: the width is 4 μm (denoted as the W_f in figure 4.1), the thickness is 3.0 μm, and the phase ring is made of gold.

4.2.2 The iterative way of phase retrieval from CPI

An iterative phase retrieval process from phase images by cyclic operations of CPI and inverse CPI transformation is proposed here. Hereafter, we named this method as Iterative Phase Retrieval for Common Path Interferometer (IPR-CPI). Its process flow is given in the figure 4-6. This method is similar to the concept of self-consistent propagation and IWFR algorithms for exit wave reconstruction from through focal series images [8], but here a Fourier filter is used instead of the propagator. The algorithm involves cyclic operation of the inverse CPI and CPI transforms and substitution of the recorded intensities with and without phase plate at image plane. The algorithm of iteration loops is shown in the figure 4-6. The objective of this algorithm is to find an optimum exit wave that has the intensities at the image plane close to the experimental intensities recorded with a known phase plate structure.
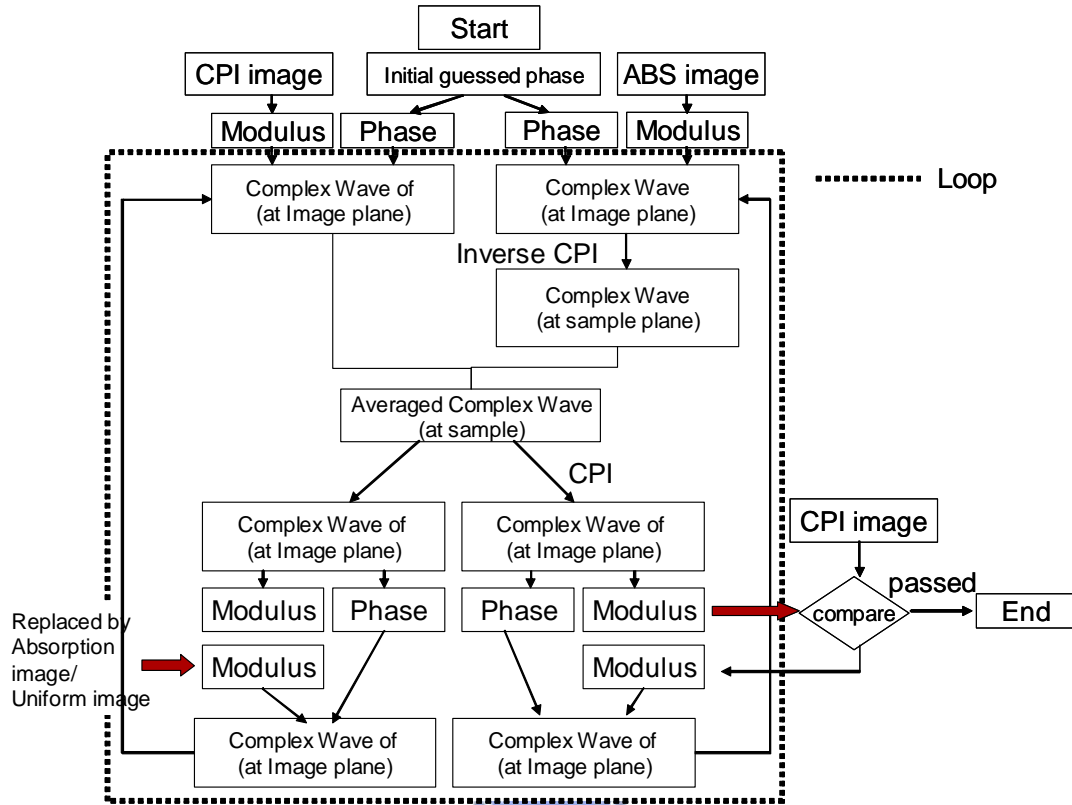
Figure 4-6 The process flow of the iterative phase retrieval form Zernike Phase contrast.

In figure 4-6, The loop begins with two starting images formed by the combination of the guessed phases with the recorded intensities with and without phase plate. Since the recorded intensity for bio-sample usually exhibits very low contrast, it is reasonable we can assume the intensity is unity in the recorded intensity without phase plate. We will show later the initial guessed phases can be zero, random or any value. Complex waves at exit surface of sample position can then be deduced, after the starting complex waves are processed by the inverse CPI transform. We take the average of two exit waves that are reconstructed from the two starting images. This is the first constraint in the iteration loop. The averaged exit wave is then processed by the forward CPI transform with and without phase plate that leads to new image waves at image plane. The new image waves are then decomposed and the square root of experimental intensities recorded with and without phase plate is substituted into the modulus part of new image waves. This is the end of one iteration loop. This loop cyclically repeats until an error is less a preset small value (typically around 50 iterations). The error value is defined in equation (4.6) which calculates the mean-square value of each pixel. The I^{exp} and I_p^{ret} are the experimental images recorded with phase plate and the image and I_p^{ret} are the intensity of image waves in the iteration times of P, respectively.

$$Error_P = \frac{\sum_{i=0}^{n} \sum_{j=0}^{m} (I_{i,j}^{exp} - I_{Pi,j}^{ret})^2}{m \times n} \qquad (4.6)$$

86

The m and n in equation (4.6) are the number of pixels of the image in width and height.

4.2.3 Analysis of IPR-CPI.

In the analysis of IPR-CPI, we simulate a plastic zone plate as described in the figure 3-7 of chapter 3. The image is recorded with a phase ring of diameter of 54 μm and the width is 4 μm as shown in figure 4-1, which is the same as we simulated in figure 3-7. Hereafter we discuss the iteration scheme by several different approaches. (1) the applicable range (2) the initial condition (3) the phase ring width and the phase ring thickness.

The applied range of IPR-CPI and choice of the CPI

The intensity is given as (4.1) [2] by assuming the width of phase plate is under ideal condition (η<0.6, where η is the ratio of width of phase plate and the theoreitcal diffraction spot size of objective lens, [6]), and the coherent luminance.

The one to one corresponding from phase to the intensity is the key to have avoid ambiguous solution of IPR-CPI. Thus, the derivatation of intensity in equation (4.1) gives a turning point, which puts a limit to the intensity mapping to the phase. This range of the phase retrieval of IPR-CPI is shown as equation (4.7).

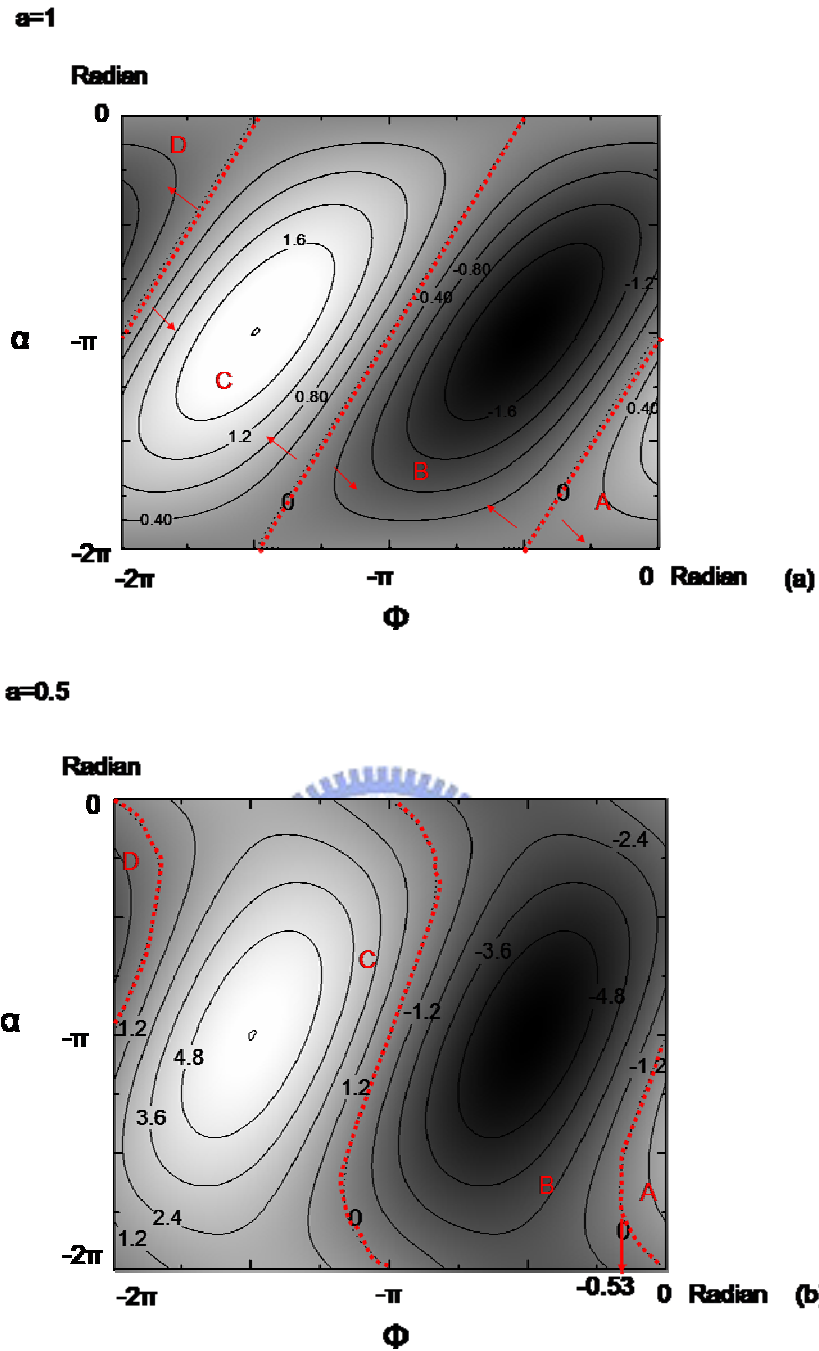$$\frac{\partial I}{\partial \phi} = 2|c|^2 (\sin \phi + a \sin(\alpha - \phi)) = 0 \tag{4.7}$$

Figure 4-7. The derivation of normalized intensity of the CPI, plotted in input phase Φ and the phase shift of Phase plate α. The four pictures represent the conditions for four different absorptions coefficient was considered: a=1 and 0.5. The dash line shows the tuning points of the intensity value, which represents the boundaries of the IPR-CPI.

For the region of applicable range of IPR-CPI with negative phase shift, the applicable range in the plot is only in "A" area in figure 4-7. The horizontal axis is the input phase φ_{object} and the vertical axis is for the phase shift of the phase plate, α. The

region "A", "B", "C" and "D" are separated by the red dotted lines, which are the derivatation of the intensity equals to zero. "A" and "C" are for the intensity and phase in propotional; B and D area is for the intensity and phase in inverse propotional. Region "A" and "B" are for general X-ray application, becuase the phase shift in phase plate and the phase of the object are both negative for X-rays. The applicable range for the transmission of phase plate is 0.5 is plotted in figure 4-7(b). The region A is shrunken, and in our case, the applicable range is from 0 to -0.53 radian.

The width and thickness of the phase ring

The contrast of the CPI image given in equation (4.7) is for the case that phase plate W_f is sufficiently small. In reality, a phase plate has finite width of W_f, which gives the cut off g_c as mentioned in equation (4.3). To simplify the explanation of the cut off frequency of the phase plate, we assume a weak absorption object. It is reasonable that the normalized exit wave of the bio-sample can be approximated as equation (4.8) by neglecting the square terms.

$$\psi_e(r) = e^{-\beta'(r)}e^{i\delta'(r)} \approx 1 - \beta'(r) + i\delta'(r) \tag{4.8}$$

Noting that $\delta'(r) = \int_{path} \frac{2\pi}{\lambda}\delta(r,z)dz$ and $\beta'(r) = \int_{path} \frac{2\pi}{\lambda}\beta(r,z)dz$. The $\delta(r,z)$ and $\beta(r,z)$ are the complex refractivity of the object in keV energy range ($n=1-\delta+i\beta$). The "z" is the direction of beam path. The $\delta'(r)$ and $\beta'(r)$ are the path integrals of the refractive index in sample along the beam path. The $\delta(r)$ and $\beta(r)$ are small than one and $\delta(r) >> \beta(r)$. If we ignore the square term, for a perfect lens and without phase plate, the intensity in the image plane can be written as $I \sim 1-2\beta'(r)$, which is expected to have low contrast because the $\beta'(r)$ is expected to be around 10^{-5} if the dz is 1000 times larger than the wavelength and $\beta(r)$ is 10^{-9} for soft material. In the back focal plane, the wave is ψ_d, which is the Fourier transform of the ψ_e. Where the operator $\Im$ is Fourier transform.

$$\psi_d = \Im\{\psi_e(r)\} \approx delta(0) - \Im\{\beta(r)\} + i\Im\{\delta(r)\} \tag{4.9}$$

The phase plate changes the phase of diffracted beam by α (in radian) within the spatial frequency of g_c. The wave in the diffraction plane can be expressed as

multiplication of equation (4.10) with $ae^{i\alpha}$, where a and α are the same notation as equation (4.1) and (4.7) for phase plate.

$$\psi_d = \Im\{\psi_e\} = \Im\{ae^{i\alpha}\langle delta(0) - \Im\{\beta'(r)\} + i\Im\{\delta'(r)\rangle_{g \le g_c} + \langle -\Im\{\beta'(r)\} + i\Im\{\delta'(r)\}\rangle_{g > g_c}\}$$

(4.10)

If we ignore the square term of β'(r) and the cross term of δ'(r) and β'(r), the intensity of image plane can then approximated as equation (4.9) (The δ'(r) is about 1000 times larger than β'(r))

$$I = \Im\{\psi_d \psi_d^*\}$$
$$\approx a^2 - 2a^2\beta'(r)_{g < g_c} + 2a(\delta'(r)_{g > g_c}\sin(\alpha) - \beta'(r)_{g > g_c}\cos(\alpha)) + \delta'(r)^2_{g > g_c} + a^2\delta'(r)^2_{g < g_c}$$

(4.11)

In equation (4.11), we ignore the square term of β'(r) and the cross term of δ'(r) and β'(r) that are relatively small to the linear term of δ'(r), β'(r) and δ(r)^2. As we can see that the image intensity I_{image}(r') recorded with a phase plate contains contribution from both low (g<g$_c$) and high (g>g$_c$) frequencies of the object wave. From equation (4.11), the image intensity coming from low frequency part, in general, is weaker than that of the high frequency, since the low frequency intensity has the same image behavior as that given in equation (4.11) consisting of the β'(r) and δ'(r)^2 that are much smaller than linear term of δ'(r) from high frequency. Furthermore, the intensity from low frequency was damped with transmission coefficient of the phase plate a^2. As a result, the phase signal from high frequency component dominates the image intensity recorded with a phase plate of finite size W$_f$. However, as we can see from equation (4.11), the phase of high frequency phase bares more complex relationship with the intensity than equation (4.7). The pure phase Φ$_{object}$(r)~δ'(r) can not be solved from the recorded CPI intensity I_{image}(r') analytically and still it requires IPR-CPI method. Another advantage of this process is the iteration process eliminates the low frequency noise.
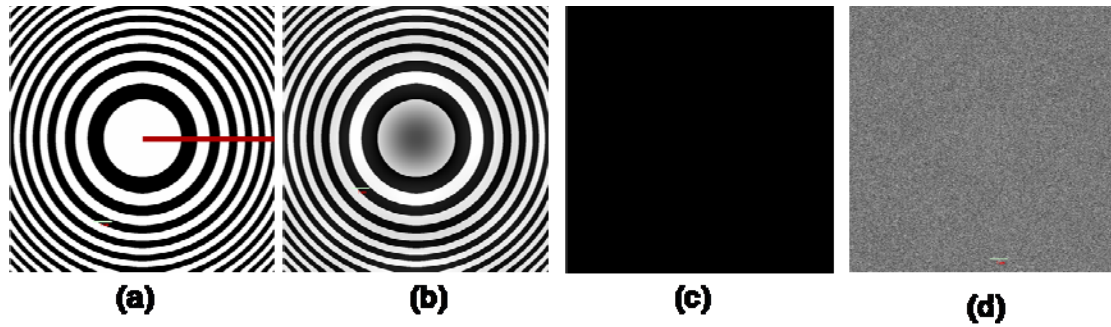
Figure 4-8 The initial condition of IPR-CPI.(a) The original phase (b) the image of Zernike phase contrast (c) The initial condition of the iteration of zero. (d) The initial condition of the iteration of random.

In order to investigate the effect of the cut-off frequency on the retrieved phase value for the IPR-CPI iterative algorithm, we have used a simulated zone-plate-like pattern as a testing example. The original phase of this testing ring pattern, as shown in figure 4-8, has the phase difference of 0.17 radian from the dark strip to bright strip. Different widths of strips are simulated to understand the frequency response of IPR-CPI. As the figure 4-6 shows, the iteration mainly depends on the difference phase advance and amplitude modulation in difference range of frequency, which is determined by the width of the Fourier plate. The portion of modulated power spectrum and the portion of un-modulated power spectrum determine the cut-off frequency of the retrieved phase. The lowest recovery frequency in Zernike phase contrast method is also restricted by the width of the phase ring. A test sample of 0.17 radian phase shift is used to test the different intensity response of the width of the phase plate from 1.0 μm to 6.0 μm. The simulated wavelength is about 1.55Å, and f is 2.7 centimeter. Thus we have the cut off frequency is around 0.5 lines/micron according the equation (4.2). The retrieved phases versus different width of the strips are plotted in figure 4-9. From the figure 4-9, we conclude that the retrieved phase is better while the width of phase ring becomes smaller especially for low frequency parts.
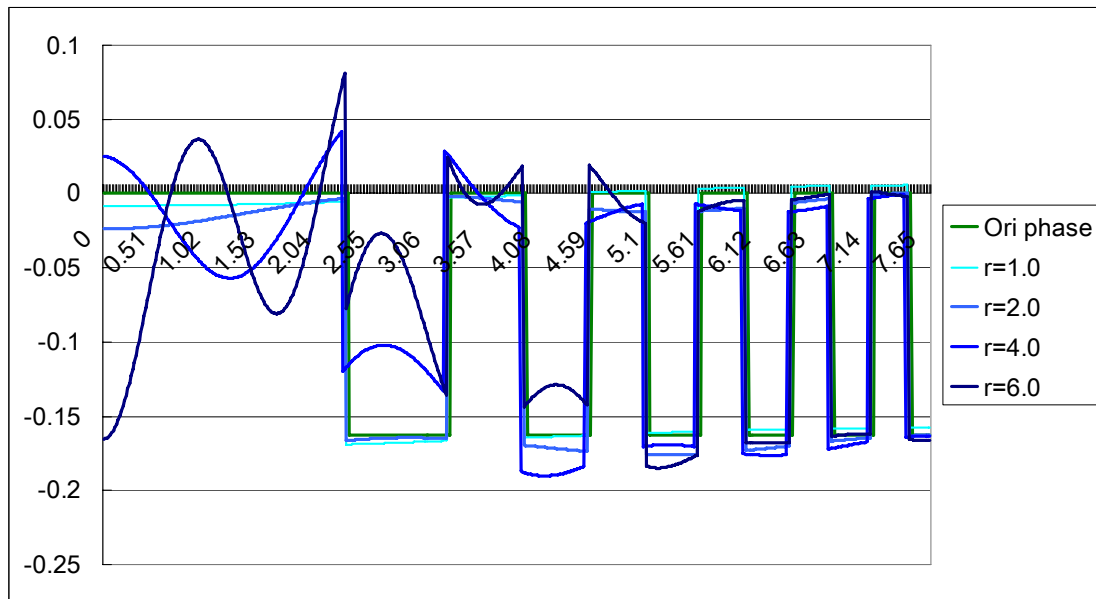
Figure 4-9 The phase is retrieved with different width of phase ring. The phase retrieved by width from 0.5 μm to 3 μm is plotted from light blue to dark blue. It is obvious that the retrieved phase is better while the width of phase ring is smaller. The initial condition of phase is reciprocal of Zernike phase contrast with iteration times of 100. The thickness of the phase ring is 3.0 μm.

The thickness determines the phase shift while the wave passes through the back focal plane in the transmission x-ray microscope. The thickness also determines the amplitude that is attenuated by the phase ring. Generally, at hard x-ray region, the phase ring is made of some high Z material which is gold or nickel as explained. However, in the simulation, the thickness is even important for the convergence of the iteration as shown in the figure 4-10. The retrieved phase convergences while the thickness of the phase ring is from 2.5 μm to 3.4 μm. However, while the phase shift of the phase ring approaches to the -2π, the value of retrieved phase is far from the original phase. In this simulation, it concludes that the retrieved phase is converged in some applicable range; otherwise, the retrieved phase is far from the original phase.
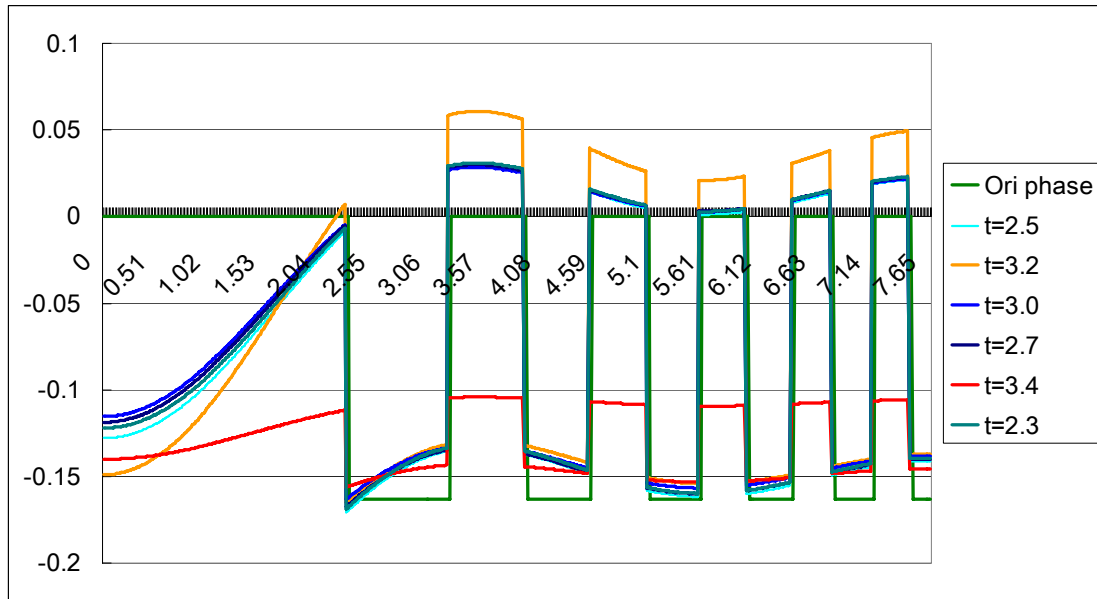
Figure 4-10 The phase is retrieved with different thickness of phase ring. In this figure, the phases retrieved by thickness from 2.3 μm to 3.4 μm are plotted, which are the phase retardation from - 1.4π to -2.1π, in which the convergence of the iteration is valid. However, the value of retrieved phase is different from the original phase while the thickness increases to 3.2. The initial condition of phase is the Zernike phase contrast with iteration times of 20. The width of the phase ring is 2.0 μm.

The initial condition of IPR-CPI

The simulation parameters are: the wave length is 1.55 Å, and the field of view is 15 μm. The simulation parameter for the phase ring which is made of gold with width of 2 μm and the thickness of 3 μm which is the real factor we used in the transmission x-ray microscope. The phase plate gives the $a = 0.5646$ and the phase shift of -5.72 radian (-1.8π), which is close to negative Zernike phase contrast. The test initial condition used in the simulation is zero and random phase with the range of 0 to 2π, which is the most common guess, as shown in the figure 4-7 (c) and (d).

In figure 4-8(a) is the original phase, which has the difference of 0.17 radian from the dark strip to bright strip. The spatial frequency of the simulation phase is from 2.5 μm to 0.4 μm in its half-pitch period, which is used to determine the cutoff frequency. Figure 4-10 (b) is the image acquired by the CPI according the Fourier plate describe above. (c) and (d) are the two initial condition applied in the iteration, which is the most common guess. The error values defined in equation (4.6) in the iteration loop with the different initial conditions are shown in figure 4-11. The convergences of error value shows in the different initial conditions are all stable in
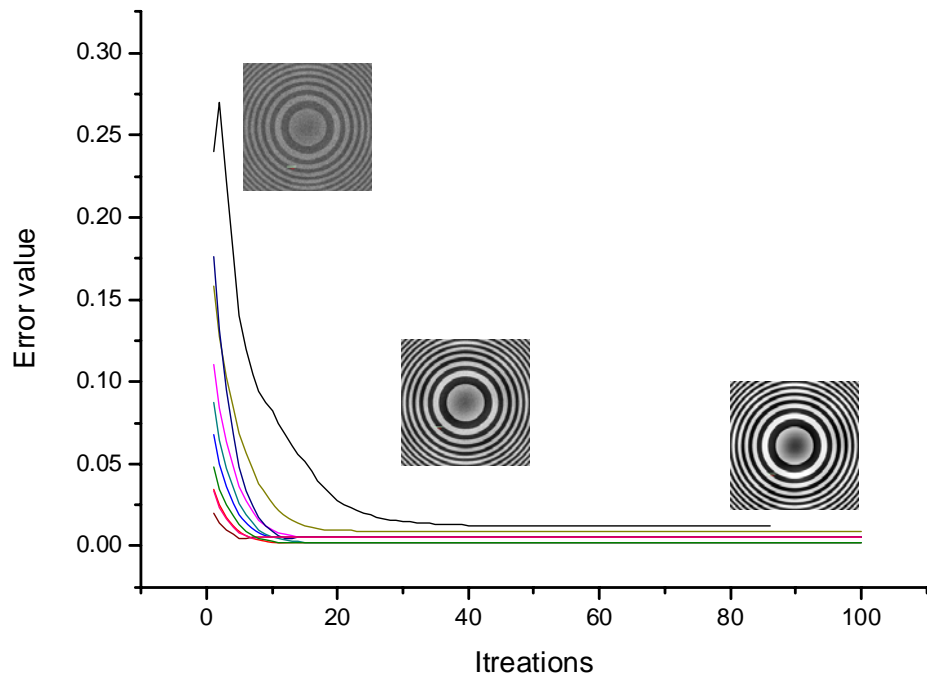
IPR-CPI.

Figure 4-11 The error value in the iteration in IPR-CPI. the iteration with initial phase of random. The images are the retrieved phase at the iteration of 10, 30 and 100, from left to right.
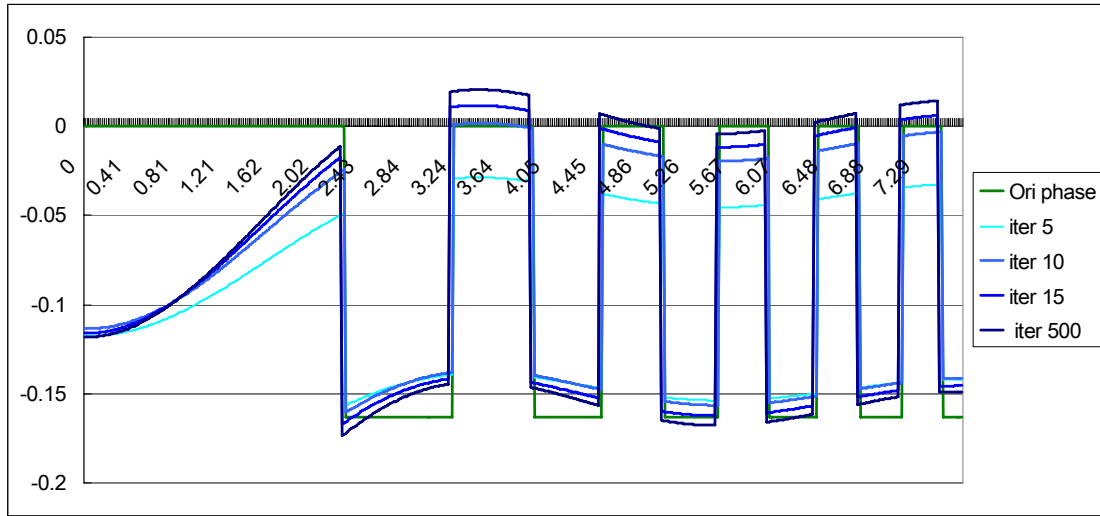
Figure 4-12 This is plot of cross-section of the red line in figure 4-9. The initial condition is zero value. Horizontal axis is for the position, and vertical axis is for the retrieved phase in radian. Green line indicates the original phase, while the light blue line to dark blue line shows the retrieved value with 5, 10, 15 and 500 iterations.

A cross section plot along the red line is shown in the figure 4-12, comparing the value of original phase and the retrieved phase for different iterations. The result shows that retrieved value is reached within 30 iterations. From the simulation result from the initial condition of zero value, we notice that the iteration is converged to a value, which can be proved by the value of 15th iteration is close to the value of 500th iteration as shown in figure 4-12. We also notice that the iteration converges fast in the first 10 iterations. By comparing the recovered phase and the original phase, the retrieved phase in high frequency is seen to be close to the original phase.

4.2.4 The experimental result

A plastic zone plate is used as a testing sample to estimate the performance of the phase contrast. The plastic zone plate is a pre-product before real gold zone plate. The thickness of the plastic zone plate is about 1.0 μm. A Zernike phase contrast image of the plastic zone plate is shown in figure 4-13. The result indicates the contrast up to 15% of Michelson visibility, while the theoretically value give the 30% of Michelson visibility. The Michelson visibility is defined as: $V = \dfrac{I_{max} - I_{min}}{I_{max} + I_{min}}$. Where the I_{max} is the maximum counts of the image and I_{min} is the minimum counts of the image. The details of the calculation are in the following sections. The theoretically value of the image of phase plate is given by the equation (4.6), which will be explained in the
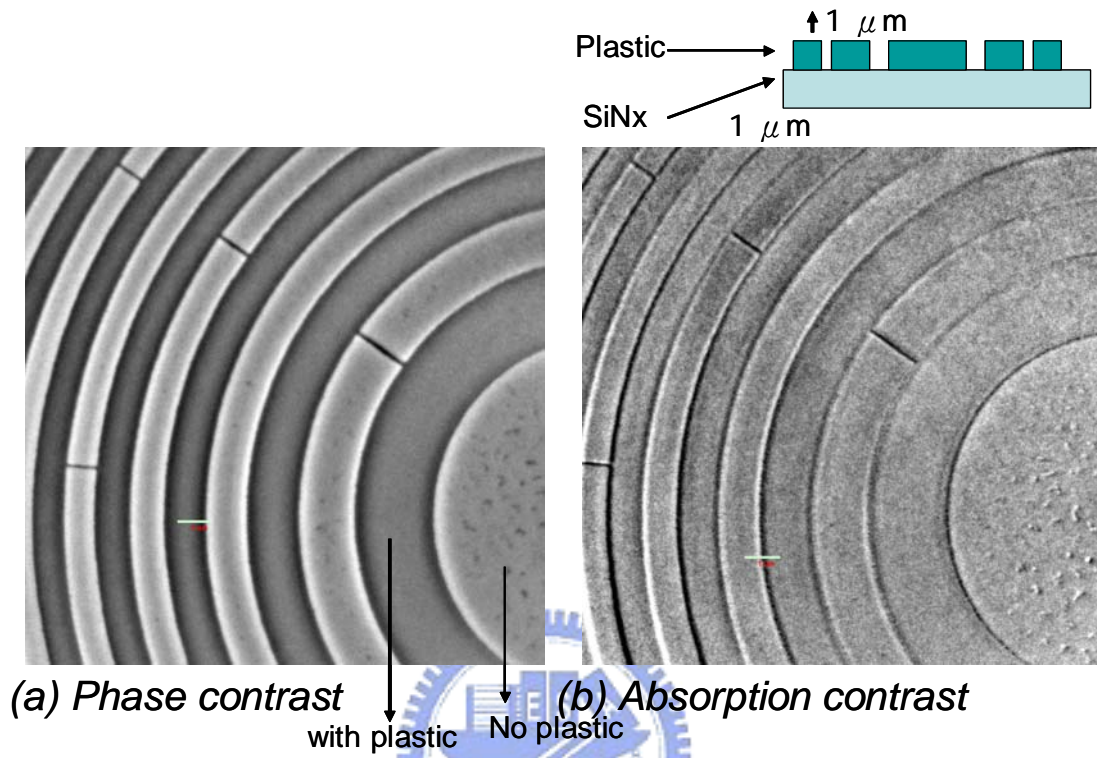
later section.

Figure 4-13 (a) Plastic zone plate image with Zernike phase contrast (b) Plastic zone plate image without Zernike phase contrast (absorption contrast). The cross section plot of the plastic zone plate is shown at the up-ring corner.

A phase sample of plastic zone plate was used to demonstrate the IPR-CPI. The sample thickness is 1.6 μm, which is made of PMMA. The δ is -4.1×10^{-6} and β is 4×10^{-9} at 8 keV. Therefore, the phase difference between the reconstruction zones and destruction zone is 0.27 radian and the absorption between the zones can be ignored. The x-ray image is taken by the transmission x-ray microscope (TXM) [9] at NSRRC, which has a phase ring of 4 μm width and 3 μm of thickness. The phase ring is made of gold, which has the δ= -4.7×10^{-5} and β=4.5×10^{-6} at 8 keV. The phase advance is about 1.8π. The phase image of this plastic zone plate is shown in figure 4-12. The experimental data is in the left and the simulation image for different width of Fourier plate is shown at right. The cross-section plot is as shown in below.

The width of the phase ring determines the lowest frequency passing the system. In our transmission x-ray microscope, the width of the phase ring is 4 μm (± 2 μm), λ is

1.55Å, and f is 2.7 cm. The thickness of the phase ring is 3.0 um, which gives the transmission coefficient a=0.5646, and the phase shift is around -5.71 radian. The cut off frequency g_c of phase is around 1 lines/micron which can be calculated by equation $g_c=W_f/2\lambda f$, which corresponds to the coherent length of this system given by λ/θ, where the θ is the divergence angle of the hollow cone, 1.8×10^{-4} [9]. The coherent length is around 0.86 μm. We have tested the phase recovery of IPR-CPI by using a plastic zone plate which is made of 1.6 μm thick of plastic. The result is shown as the figure 4-15.
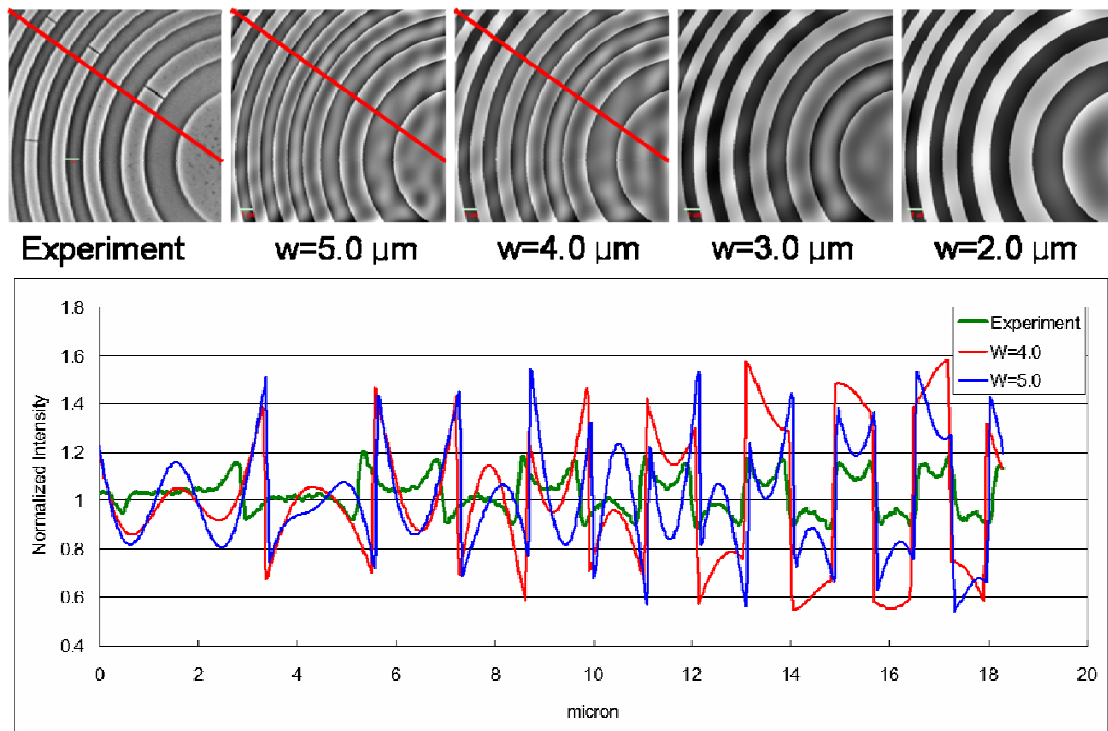

Figure 4-14. The Zernike phase contrast image and its simulation image. The upper-left is the image by Zernike phase contrast at 8 keV. The other images are the simulation images with different phase ring width. The plot is the cross plots of the red line indicating in the upper image. The trend of the plot indicates the ring width is close 4.0~5.0 μm, by judging the frequency response.

From the figure 4-14, we estimate that the experimental contrast is not reach the theoretical value which is only about half of its theoretical value, which is due to the incoherence of source and illumination conditions. Thus, the phase retrieved is hard to accurately recover from this experimental data. However, the retrieved phase can be rescaled according to the ratio between theoretical value and experiment result with the same phase ring. The phase retrieved result is shown as the figure 4-14. The upper-left image is the Zernike phase contrast, and the upper-right image is the

retrieved phase. The parameters for phase retrieval are that the width of phase ring is 4 μm and the thickness of the phase ring is 3μm. Comparing the two images, the retrieved phase image has better response in the low spatial frequency and smooth edge than the image of Zernike phase contrast. The value of retrieved phase is about 0.13 radian, i.e. half of the value as expected. The phase shift for a PMMA of 1.6 μm in thickness is 0.27 radian, only 50% converge for this region. However, from the figure 4-16, the phase retrieved value can be 63% for the ideal value for smaller line width.
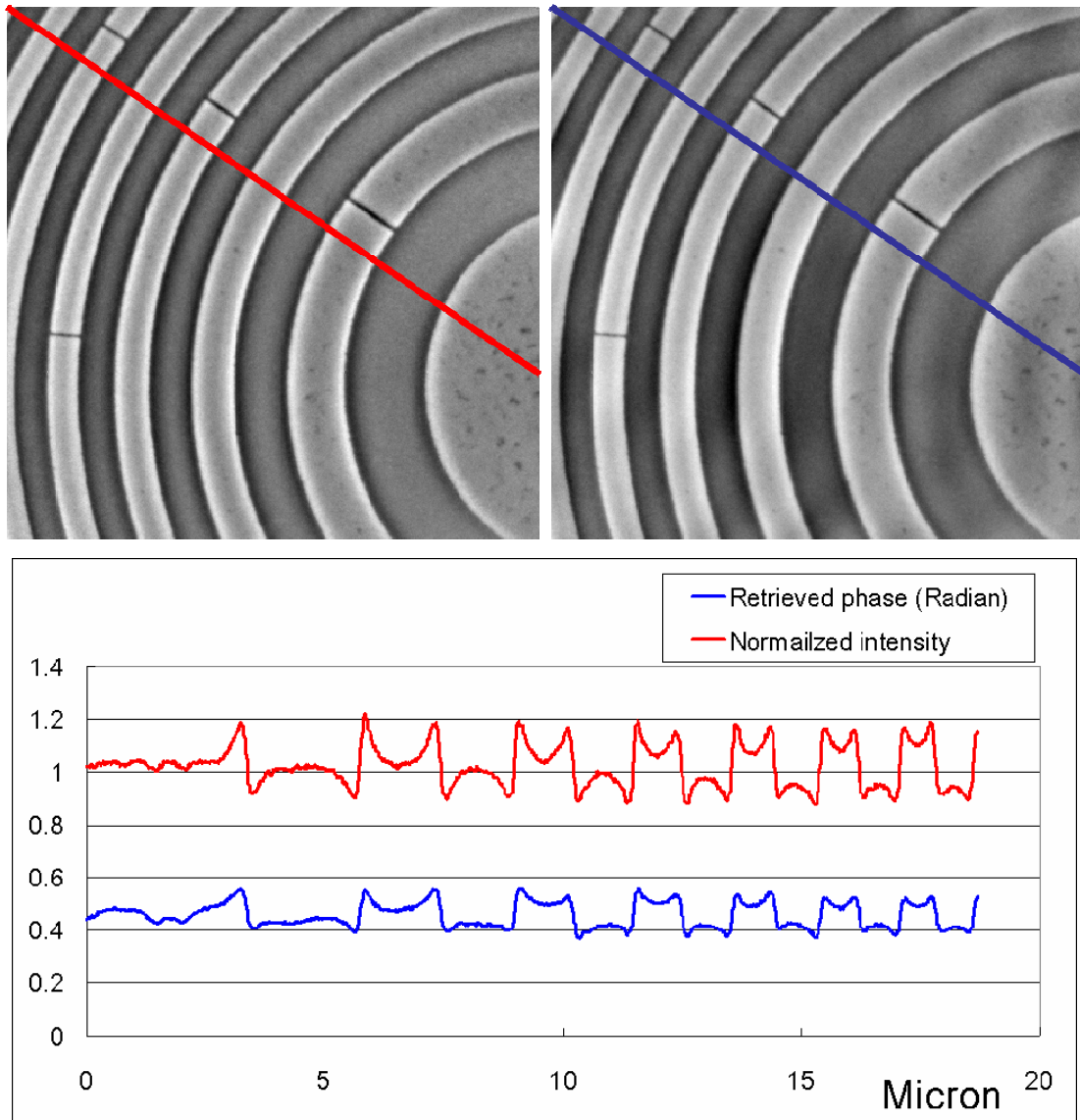
Figure 4-15. Zernike phase contrast image and its retrieved phase image. The upper left is the image from Zernike phase contrast method. The upper right is the retrieved phase from Zernike phase contrast method. The plots below are the cross-section plots of the red line in the above images. It can be told that the cross-section plot of the retrieved phase is smooth and less over shoot than Zernike phase contrast method. The retrieved phase value is around 0.13 radian, less than the expected value.
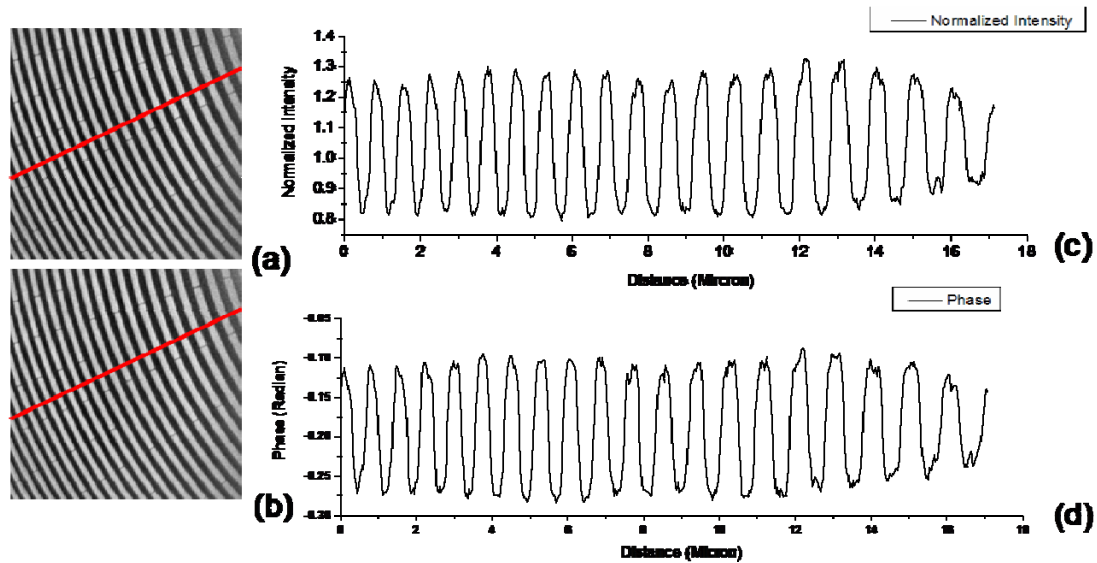
Figure 4-16 The plastic zone plate for verifying the IPR-CPI method for smaller line width (a) The recorded image of zernike phase contrast. (b) the retrived phase by IPR-CPI.(c) cross-section of red line in (a). (d) cross-section of red line in (b).

4.2.5 Summary for IPR-CPI

The IPR-CPI for quantitatively phase retrieval is presented. The convergence of IPR-CPI is tested by the simulation data. The effect of initial guess value of phase, the thickness and the width of phase ring are discussed. In general, this method can be converges within 50 iterations, and the retrieved phase has different response for different phase ring, the narrower the width of phase ring, the better low frequency response. The limitation of retrieved phase range is also discussed. The retrieved phase based on the simulation data has good agreement with the simulated phase. The experimental results also confirmed with this iteration method by retrieving phase of an image of a plastic zone plate. The retrieve phase value agrees with the value of Zernike phase contrast in this experiment, which is half of the theoretical value of Zernike phase contrast. The retrieved phase is also half of the phase shift of the plastic zone plate. Therefore, we conclude that this method, IPR-CPI, can be used to quantitatively retrieve phase with single image of Zernike phase contrast within limited phase range. This method also suppresses the artifacts generated by Zernike phase contrast method.

4.3 The Phase Tomography

To enhance the phase contrast, we can use Zernike phase contrast as we described in pervious sections. However, Zernike phase contrast method is just an enhancement instead of a quantitatively phase retrieval. Thus the phase tomography by using the image which taken by Zernike phase contrast method is not correct in most case.

The phase tomography [10-13] is known as the tomography which deals with real part of the reflection index, while the general tomography (i.e. absorption tomography) deals with the imaginary parts of the reflection index. Thus, the tomography is not only the image in 3D but a quantitatively description of the optical properties of a sample. The phase tomography requires the quantitatively phase value for the reconstruction just as general tomography needs the accurate absorption data. However, a major different in phase tomography from general absorption tomography is that the phase range can only be from $-\frac{\pi}{2}$ to $+\frac{\pi}{2}$. We define the phase wrap as the phase is over this range. The procedure for the data processing is even easier than the general tomography by assuming that the phase is not wrapped in the sample. The phase is added, thus, the value of phase image is already the sum of the phase at certain angle. Therefore, the FBP can be applied to the phase tomography without modification.

Since we have already introduced the phase retrieval methods in the chapter 3, we will discuss the phase tomography by these methods, which are Zernike phase contrast, the combine method of TIE and SCWP and IPR-CPI.

4.3.1 Phase contrast tomography by Zernike phase contrast

As we analysis in pervious section, the general Zernike phase contrast enhance mostly the contrast with higher frequency parts of the image. The Zernike phase contrast gives a background intensity distribution which may also confuses the tomography reconstruction. In experiment, the only difference in a phase tomography from a general tomography is to put the phase ring at the back focal plane. It has the advantage to be the easiest way to obtain the phase tomography, since it has the same procedures as the general tomography. We demonstrate these features in simulation and experiment in the following.

The simulation parameters are that the energy is 8 keV, the field of view is 15 μm and the thickness of phase ring is 3.0 μm. The test object is a face center cubic (FCC) cell of plastic balls. The reconstruction procedure is just the same as the general tomography. However, because of the uneven response for different spatial frequency and the limitation of the phase range, the values in phase imaging are not always proportional to phase values in the sample plane.

The reconstructed slices of the tomography by Zernike phase contrast are shown below with the simulated phase ring width from 1.0 μm to 4.0 μm, The artifacts are generated in the reconstruction, as shown in the figure 4-17. As seen in the simulation, for narrow phase ring, the image contains more signal of low frequency. For the wider phase ring, more artifacts are found. The reconstructed ball in center becomes hallow under phase ring of 4.0 μm. It shows that the low frequency signal of the object is hard to retrieve from wide phase ring. However, despite of the artifacts, this method is still able to get meaningful information (but not quantitative result) as demonstrated by the experiment below.

The reconstruction procedure is just the same as the general tomography. However, because of the uneven response for different spatial frequency and the limitation of the phase range, the relation between the values in phase imaging are not always proportional to phase values in the sample plane. The artifacts are generated in the reconstruction, which are shown in the figure 4-17. The simulation conditions are the energy is 8 keV, the field of view is 15 μm and the thickness of phase ring is 3.0 μm. The test object is a face center cubic (FCC) balls, which is assumed to be plastic material. The simulated phase ring width is from 1.0 μm to 4.0 μm, the reconstructed slice of the tomography by Zernike's phase contrast is shown below.
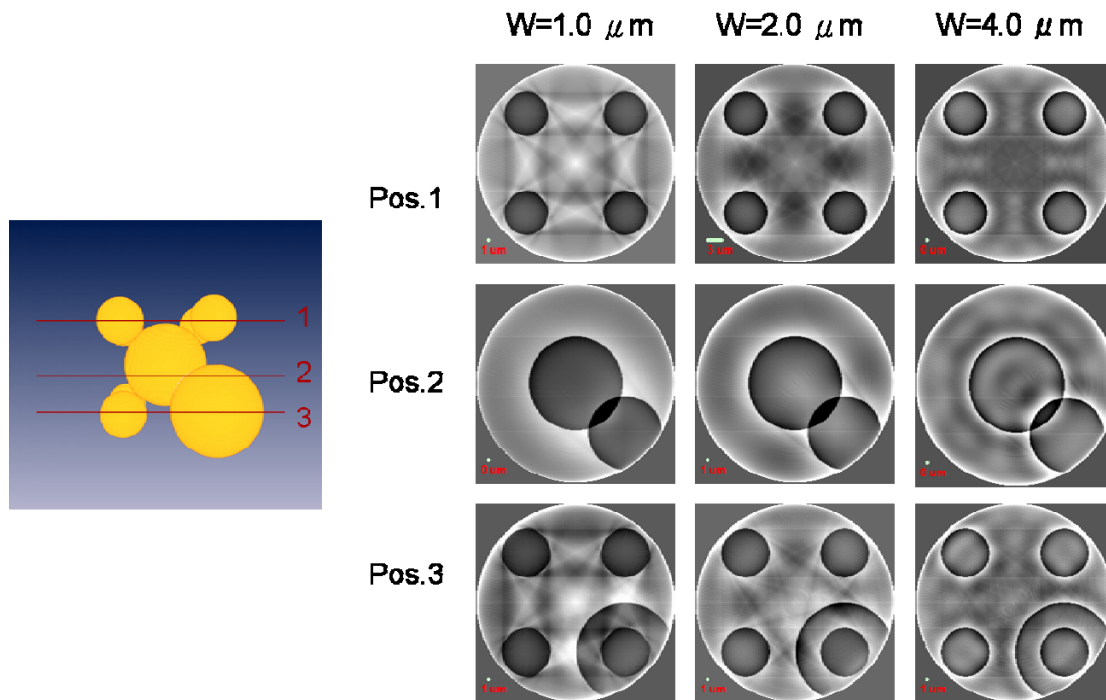
Figure 4-17 The reconstructed slice of tomography from the object shown in the left. The phase tomography is done by the FBP and Zernike phase contrast. The dark area indicates the strong phase because the Zernike phase contrast is negative type. The images in the same row are the slice in the same position. The images in the same column are with the same width of phase ring.

From the simulation, for the wider phase ring, more artifacts are found. For the thinner phase ring, it contains more signal of low frequency. The reconstructed ball in center becomes hallow under phase ring of 4.0 μm. In this simulation, we understand that the low frequency signal for the object is hard to retrieve for wide phase ring. Despite of artifacts, this method is still able to get meaningful result but quantitative result as the experiment described below.

The experimental result of phase tomography by Zernike phase contrast is demonstrated by the polymer sample, which is the filter material with about 0.4 um holes inside. It is stained with Os to increase the contrast. The experimental conditions are at 8 keV, -70 to 70 degrees, and total 141 pages for reconstruction. The images for 3D rendering and slice are shown in the figure 4-18. The interconnection of holes in the material can be observed because the dimension of these holes is small. The artifacts at the edge of hole can be observed due to the effects of the Zernike phase contrast.
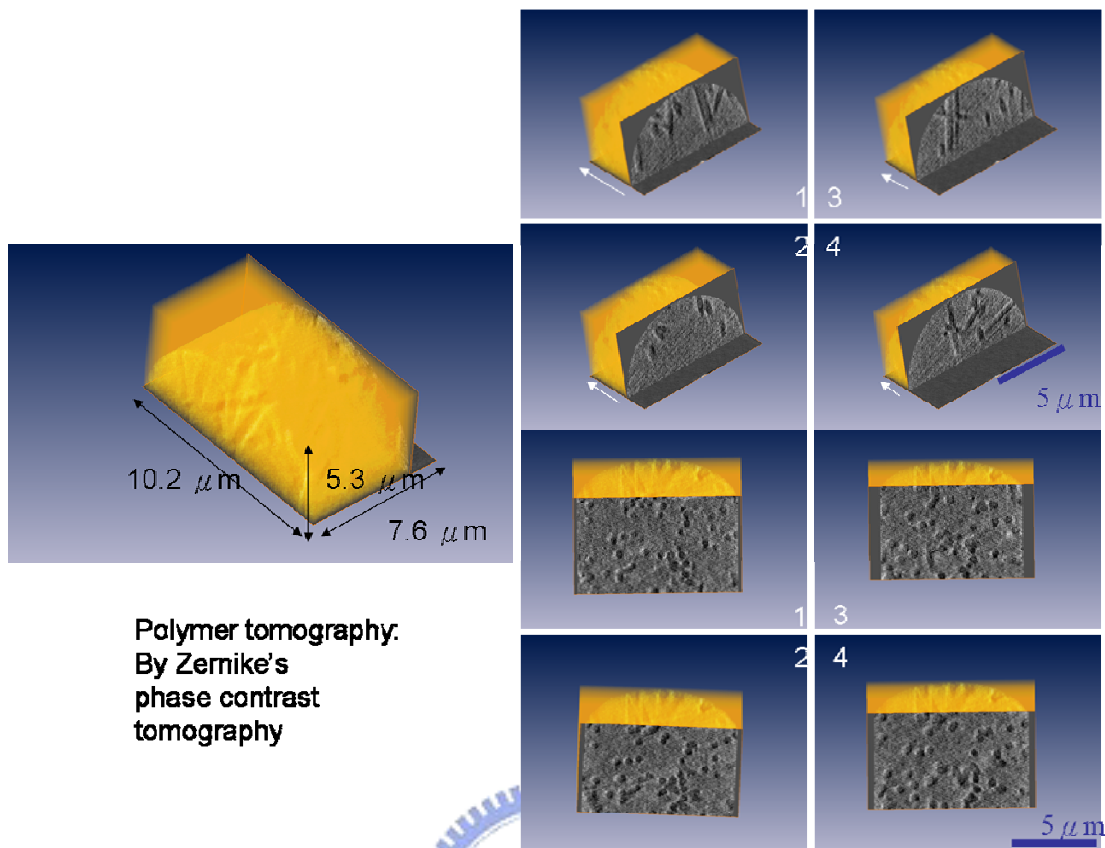
Figure 4-18 The phase tomography by the FBP and Zernike phase contrast of the filter material with Os stained. The dark area indicates the holes because the contrast is reversed in this tomography. The hole and their interconnection can be observed clearly. However, the halo around the holes suggested that the existence of the artifacts.

4.3.2 Phase tomography by combined method of TIE and SCWP

From the simulation, the phase retrieval has the accurate phase recovery other than Zernike phase contrast or IPR-CPI. In theorem, the phase retrieval from the combined method TIE and SCWP should be good for the phase tomography and it was estimated experimentally done for a low resolution setup and TIE based solution [8]. However, the phase tomography by phase retrieval in TXM is hard to perform because the low contrast and alignment of images for different angles. The experimental phase tomography by TIE and SCWP is currently not been implemented because the above reasons.

In general, the SCWP has shorter phase range than that of TIE. The tolerance for the IPR-CPI is even smaller than SCWP, the suitable range is only the small region before the contrast reverse, as explained in the previous section. However, experimentally, the phase image is hard to obtain for different degrees in the TXM. We compare the phase retrieved by two different schemes as shown in the figure 4-19.
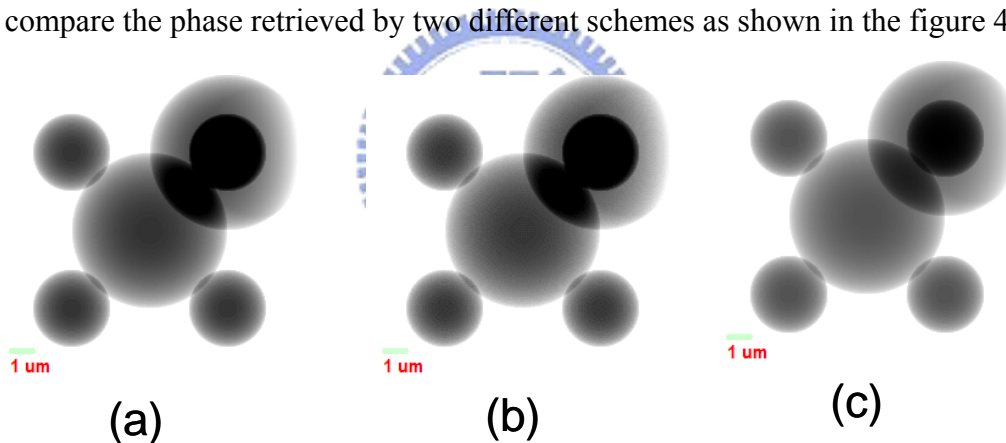
Figure 4-19 (a) The original phase (b) The phase retrieved from combined method. (c) The phase retrieved from Zernike phase contrast in ideal case.

The two phase retrieval result in figure 4-13 (b) and (c) has slightly different. The contrast in (c) is less. In fact, the IPR-CPI is not as good as the phase retrieval because the range of the phase is limited as describe before. In this comparison, the phase retrieval is a better method than IPR-CPI; however, this method in TXM is not easy to implement because the alignment and noise problem. This is a part of the future work.

4.3.3 Phase tomography by IPR-CPI

The phase tomography by IPR-CPI gives the quantitative value compare to directly reconstruct the phase tomography from the Zernike phase contrast, as shown in the figure 4-20. Comparing the two sets of slices, the slices of reconstructed by Zernike phase contrast has more defects then the one reconstructed IPR-CPI. Furthermore, the value of the δ is incorrect, which can be told by the fact that reconstruction of outer zone is lower than the value of middle parts. The δ value should be all negative. The values of reconstructed slice of IPR-CPI are accurate and with fewer defects than the tomography for Zernike phase contrast. The IPR-CPI method has improved the phase tomography from the Zernike phase contrast. The simulation condition is the same as previous section, with phase plate thickness of 3 μm and width of 2 μm. The experimental result is used to confirm this simulation as described below.
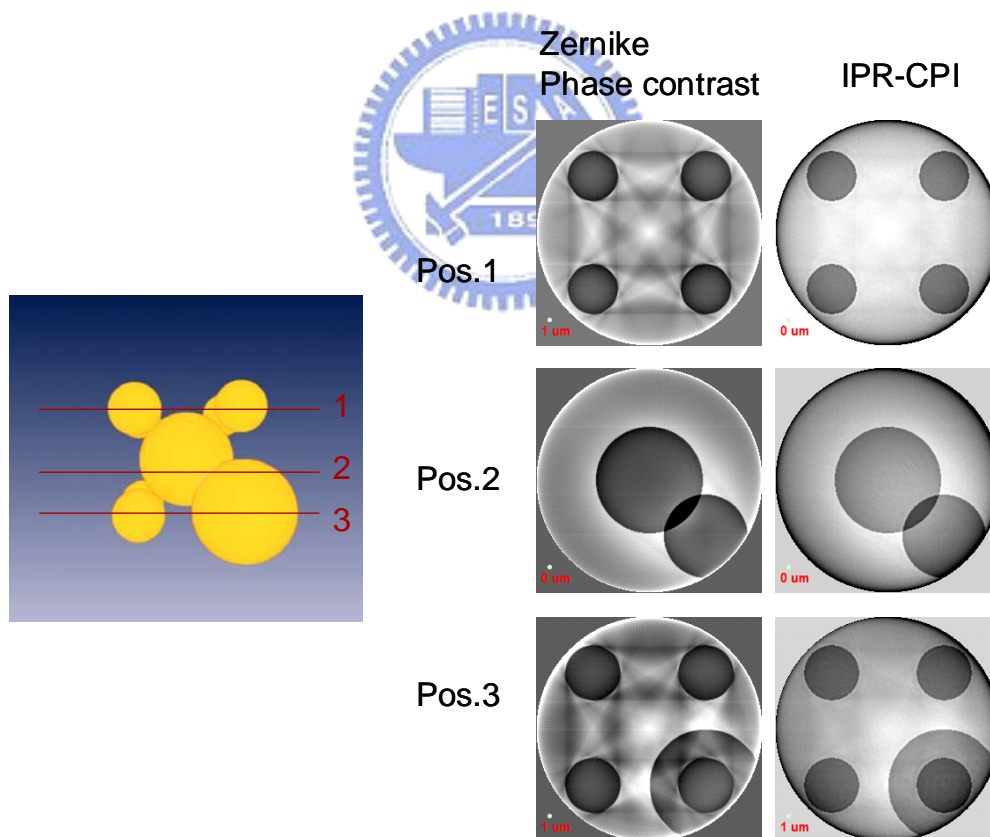

Figure 4-20 The reconstructed slice from Zernike phase contrast is shown in the left column, and the reconstructed slice from IPR-CPI is shown in the right column.

Application in cell imaging

A gastric adenocarinoma cell (AGS) with Osmium and Uranium stained was used as a test example for the phase tomography. The cell was first immersed in 1% Osmium tetroxide and 0.1% Uranyl acetate solution before being dehydrated by alcohol. The dehydrated cell is fixed in shape and dried. The stained part is only the grooves on the surface of the cell. The sample is chosen to demonstrate the phase tomography because the size of the stained groves is below 1 μm which is good range for our TXM setup. The thickness of the Osmium and Uranium can be estimated by the similar protocol used in the biology sample for TEM study.   A typical range of the thickness of stained metal is around several nanometers. We prepared the sample by using longer immersion time than the protocol in TEM, thus we expected that the metal thickness of our sample should be thicker than that in TEM.

The TXM was operated at 8 keV, with zone plate of 85 μm in diameter and its outmost zone width of 50 nm. The field of view is around 15 μm. The effective thickness of the gold phase ring is 3.0 μm, which generates a phase shift of -1.8π radian, i.e. in the negative Zernike phase contrast method. The transmission of the phase ring is 0.357 and a=0.5646. From equation (4.7) the maximum phase for IPR-CPI is 0.53 radian, which correspond to around 300 nm thick of Osmium or Uranium. According the previous discussion, the phase retrieval is in the applicable range of IPR-CPI.

After the sample is placed on a silicon nitride film of 500 nm thick, the images were recorded from projection angles from -70 degree to 70 degree, all together 141 images were collected. The images were processed by IPR-CPI to obtain the pure phase information. The results are shown in figure 4-21 for (a) the Zernike phase contrast image of zero degree and (b) the retrieved phase of exit wave. The cross section plots of (a) and (b) are shown in (c) and (d), respectively.
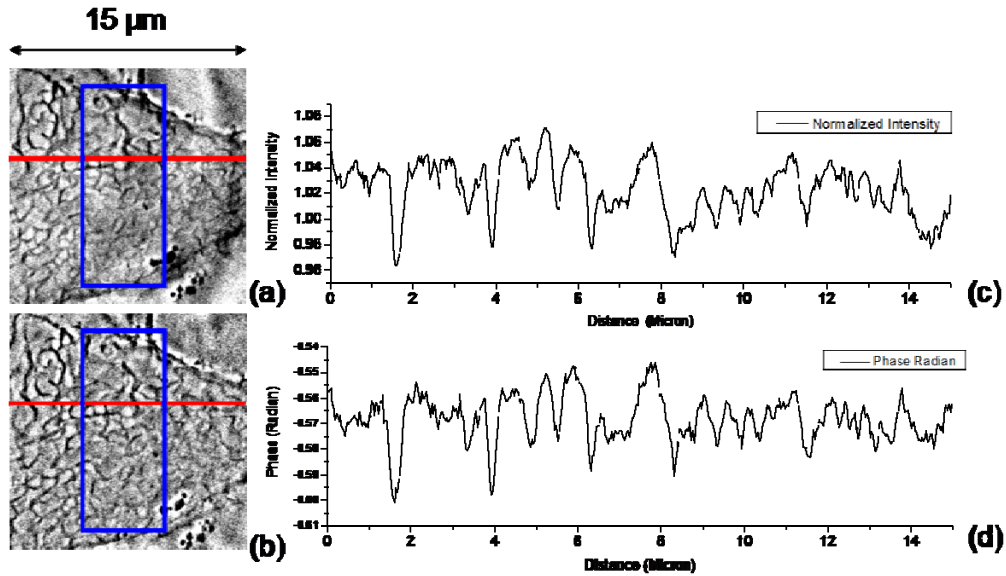
Figure 4-21 The image of Zernike phase contrast of the AGS cell (a) and its retrieved phase (b). The plots of the cross sections of the red line in (a) (normalized intensity) and (b) (Retrieved Phase) are plotted as (c) and (d), respectively. The retrieved phase is in the range of -1.125 to -1.155, with in the range of 0.05 radian. The blue squares indicates the area for tomography reconstruction.

The low frequency information in figure 4-21 are supressed after the IPR-CPI processes as shown in the figure 4-21(b). According to equation (4.11), there is no low frequency information in the Zernike phase contrast image in this system if this object is weakly absorbed. The low frequency noise is mainly comes from the unproper of flat field process(reference image correction). Thus, the IPR-CPI surpress the low frequency noise and give more flexibility for the raw data quality. However, the high frequency artifacts, from the edge of large objects, are still unavoidable.

The images were first aligned and processed for setting a zero point of the phase and then reconstructed by the Filtered-Back Projection (FBP). The reason of zero point setting is that the phase is a relative value. It is nessaray to set one common point in each projections that we assume the phase shifts are the same in this point. Generally, we set this point where is no objective there. The rendering of the reconstructed 3D voxels is shown as figure 4-22(a). The tomography slices of tomography are as shown in the figure 4-22(c) and (d). Noting that the reconstuction portion is only the center part of the cell, as indicating in the blue area in figure 4-21(a) and (b). It is because that the mechincal vibration and rotation center shift shrinks the common area of the reconstrcution area of tomography. The size of rendering and reconstruction area in

figure 4-22(a) is x=4.46 μm, y=2.81μm, z=12.9μm. The size of figure 4-22(b) and (c) is x=y=9 μm and z=12.9μm.

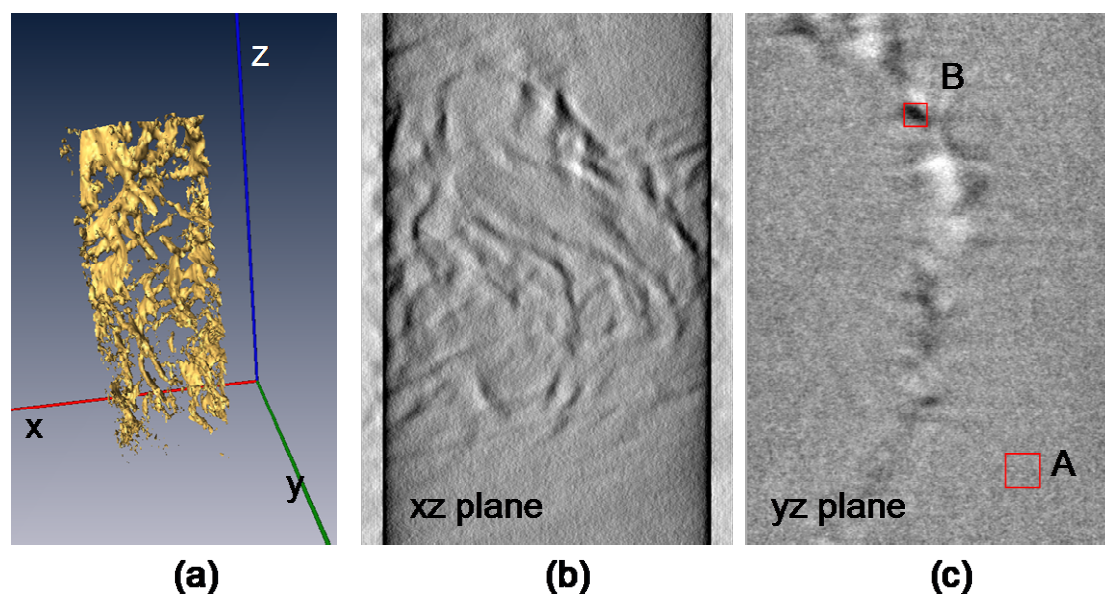

(a)   **(b)**   **(c)**

Figure 4-22 (a) The 3D rendering of the phase tomography of the outer shell of the stained AGS cell (b) the slice in XZ plane (c) the the slice in yz plane. The dark region represents the negative phase.

The dark region represents the negative phase, which is agreed with the negative value of the index of reflection of the sample in X-ray region. In figure 4-22 (c), the phase shift in the dark area B is about -1×10^{-3} radian/pixel while the background area A is around -1×10^{-4}/pixel. Where the pixel size is 17.6 nm. The phase shift from a 17.6 nm Osmium or Uranium is about -2.85×10^{-2} radian. Thus, the value of -1×10^{-3} radian/pixel can be refered to the about 3.5% concentration of Osmium or Uranium. The concentration range estimaged is in agreement with the normal TEM sample preparation for TEM.

In conclusion, a method is proposed for quantitative retrieval of the phase in three demension within hundered nanometer to tens nanometer resolution. The principle and appilcable range of this method is discussed. Finally a biological sample with heavy metal stain is studied to demonstrate this retrieval method with obtained value falling in the expected range.

4.4 Summary

In this chapter, we have demonstrated the phase retrieval method with Zernike phase contrast. We have stated the algorithm and simulated this algorithm. We also prove this algorithm with a test sample.

The tomography principle and FBP are introduced. The experiment for the nano tomography is demonstrated to reach the spatial resolution close to 60 nm. Followed with the principle of phase tomography, three different ways of implementing the phase tomography, the Zernike phase contrast, the combine method of TIE and SCWP and the IPR-CPI, are studied with simulation done under realistic experimental condition. The pros and cons are discussed. The feasibility of implementing the phase tomography by IPR-CPI is demonstrated both in simulation and in imaging a real biological cell.

Chapter 5

Conclusions

A zone plate based transmission X-ray microscope was installed at NSRRC in September 2004 on beamline 01B with a superconducting wavelength shifter source, which is the first microscope of such type operated at synchrotron facilities world wide. Using this TXM, several important features in X-ray imaging have been studied, which include spatial resolution, absorption imaging, phase imaging, tomography, and different image process methodologies. We give a brief conclusion of these key features in the following.

Image Resolution

At the time this thesis is written, the TXM has reached a resolution below 50 nm using first order image in absorption imaging with photon energy of 8 keV (section 2.3.2). The resolution by the Zernike phase contrast is also close to half of the ideal value (section 4.2.4). The low-Z material such as plastic or biological sample of 1 μm thickness can be imaged at 8 KeV with about 20% of Michelson visibility. A sub 100nm particle of low Z material can be detected by phase imaging. For tomography, the TXM is able to reach 60nm resolution using absorption contrast. However, there is no total solution for the phase tomography because the phase wrap for large object and some other practical issues.

Phase Tomography

Regarding the phase tomography, three different ways of implementing, the Zernike phase contrast, the combined method of TIE and SCWP and the IPR-CPI, are studied. Currently, the phase tomography done by IPR-CPI is regarded as the most feasible way of phase tomography.

For different phase retrieval methods, each method has their pros and cons. For the combined TIE and SCWP, which have problems of alignment, low contrast compared to the Zernike phase contrast and multi-images, is not practical for taking phase tomography. However, in theorem, there is no limitation on the value of phase both in TIE and SCWP, which is good for the extending the application of the phase tomography. Another phase retrieval method, IPR-CPI, is proposed and studied by the simulation and experiment. One advantage of this phase retrieval method is it needs

only one image, which has high contrast compare to the pure absorption contrast. However, IPR-CPI has some drawbacks that the phase recover range is limited by the phase ring thickness and the frequency response is limited by the width of the phase ring.

Feasibility of Live Tomography

We should make some remarks the phase tomography for a living cell as we asked at the very beginning of the work. For a single cell frozen in the capillary tube as an example, the absorption contrast is too low even for the alignment. Using the Zernike phase contrast as already been setup, the contrast of the cell in a frozen capillary can be simulated. (The simulation parameter is shown in chapter 1.) The results are summarized in figures 5-1 and 5-2.

The answer to question on whether a living cell can be imaged is not obvious. Both of the phase contrasts in figure 5-1 are noisy and hard to recognize. The combine method of TIE and SCWP also failed in this case because TIE does not give the initial guess correctly. The Zernike phase contrast gives a better image but still noisy. However, after the tomography, because of the addition of the signal, the image quality is greatly improved as shown in figure 5-2. We conclude that it is possible to visually observe a cell with 8 keV x-rays without metal stain if a stable cyro-stage and X-rays with coherent length larger than the object size are employed. Currently, the coherent length in our X-ray system is only about 0.86 μm.
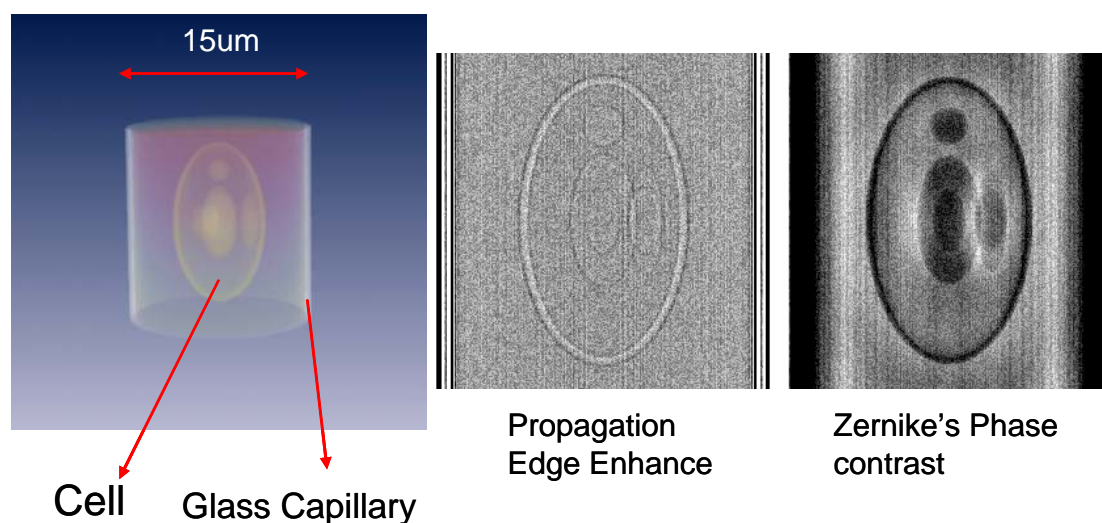

Figure 5-1 The phase image of the biology cell in the capillary. (Left) the schematic of cell in

the glass capillary. (Middle) The phase image enhanced by the edge enhancement. (Right) The phase image enhanced by Zernike phase contrast. Noise of 1 % of RMS value is added in to facilitate the real image in TXM.

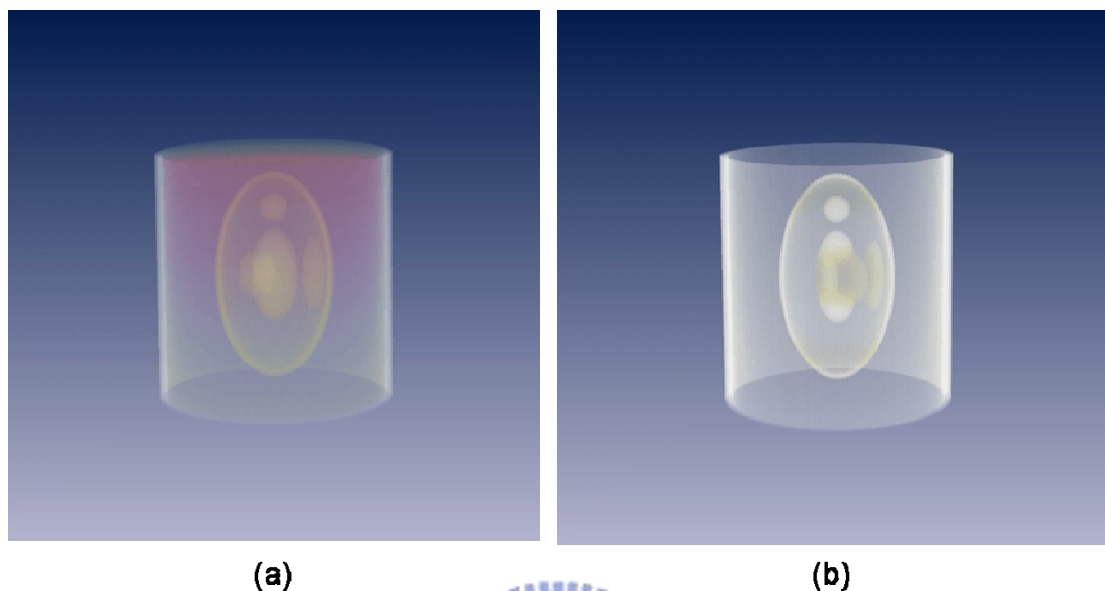<center>(a)   (b)</center>

Figure 5-2 (a) the 3d rendering of the original cell in the capillary (b) the 3d rendering of the reconstruct phase tomography of cell in the capillary.

Future Work

The contrast of Zernike phase contrast can be further improved. The increase the beam coherency can reduce the required width of the phase ring, which mostly depends on the improvement of the source and condenser. By doing so, the artifacts of Zernike phase image will be less and the quality of phase image will be increased, especially in the low frequency response.

Following the simulation work given in previous sections, to achieve the simulation condition requires a stable rotation stage. A robotic cryo-system is the desirable solution for future application on biology. It also is important to enhance the contrast for desirable function/mechanism in biology sample by labeling the living cell for X-ray contrast. If the alignment is no longer an issue, the phase retrieval by the combined method of TIE and SCWP will becomes an important way to find out the phase in a wide phase range. However, this technique is good for two dimensional images but still time consuming for tomography.

Features of high penetration and high resolution have made TXM a unique and

irreplaceable tool. The phase imaging in TXM is also unique to observe the low-Z soft matter. We believe that the phase imaging technique will become mature and serve in the microscope community for wide applications.

REFERENCES

Chapter 1.

[1] Jens Als-Nielsen and Des McMorrow, *"Elements of Modern X-ray Physics"*, John Wiley & Sons, New York (2001).

[2] Weilun Chao, Bruce D. Harteneck, J. Alexander Liddle, Erik H. Anderson and David T. Attwood, *"Soft X-ray microscopy at a spatial resolution better than 15nm"*, Nature,**435**, 1210 (2005).

[3] G.-C. Yin, Y.-F. Song, M.-T. Tang, F.-R. Chen, K. S. Liang, F. W. Duewer, M. Feser, W. Yun, and H.-P. D. Shieh, *"30 nm Resolution X-ray Imaging at 8 keV Using Third Order Diffraction of a Zone Plate Lens Objective in a Transmission Microscope"* Appl. Phys. Lett. **89** , 221122 (2006).

[4] G. C. Yin, M. T. Tang, Y. F. Song, F. R. Chen, K. S. Liang, F. W. Duewer, W. Yun, C. H. Ko, and H. P. D. Shieh , *"Energy-tunable Transmission X-ray Microscope for Differential Contrast Imaging with Near 60 nm Resolution Tomography"*, Appl. Phys. Lett. **88** , 241115 (2006).

[5] David Attwood. "*Soft x-rays and ultraviolet radiation: principles and applications*."Cambridge University Press, first edition, (2000).

[6] J.D. Jackson, *"Classical Electrodynamics"*, Wiley, New York, third edition, (1998).

[7] Max Born and Emil Wolf, *"Principles of optics"*, Cambridge, seven edition, (2003).

[8] R. W. Gerchberg and W.O. Saxton, Optik **35**, 237 (1972).

[9] J.R. Fienup, "Reconstruction of an object from the modulus of its Fourier transform", optics letter,3,27 (1978).

[10] M. R. Teague, *"Deterministic phase retrieval: a Green's function solution"* J. Opt. Soc. Am. **73**, 1434 (1983).

[11] T. E. Gureyev, A. Roberts, and K. A. Nugent, *"Partially coherent fields, the transport-of-intensity equation, and phase uniqueness"*, J. Opt. Soc. Am. **12**,1942 (1995).

[12] K. A. Nugent, T. E. Gureyev, D. F. Cookson, D. Paganin, and Z. Barnea, *"Quantitative Phase Imaging Using Hard X Rays"* Phys. Rev. Lett. **77**, 2961 (1996).

[13] A. Barty, K. A. Nugent, D. Paganin, and A. Roberts, "Quantitative optical phase microscopy",Opt. Lett. **23**, 817 (1998).

[14] P. Cloetens, W. Ludwig, J. Baruchel, D. Van Dyck, J. Van Landuyt, J. P.Guigay, and M. Schlenker,*"Holotomography: Quantitative phase tomography with*

Micrometer resolution using hard synchrotron radiation x rays" Appl. Phys. Lett. **75**, 2912 (1999).

[15] L.J. Allen, W. McBride, N.L. O'Leary, M.P. Oxley, *"Exit wave reconstruction at atomic resolution"*, ultramicroscopy **100**, 91 (2004).

[16] G.-C. Yin, F.-R. Chen, Y. K. Hwu, H.-P. D. Shieh, and K. S. Liang, *"Quantitative phase retrieval in transmission hard x-ray microscope"*, Appl. Phys. Lett. **90** , 181118 (2007).

[17] I.-H. Hong, T.-H. Lee, G.-C. Yin, D.-H. Wei, J.-M. Juang, T.-E. Dann, R. Klauser, T.-J. Chuang, C.-T. Chen, and K.-L Tsang, "*Performance of the SRRC Scanning Photoelectron Microscope*", Nucl. Instr. Meth. A **467**, 905 (2001).

[18] D.H. Wei, I. H. Hong , Ruth Klauser, Y. J Hsu , G-C. Yin , T. J. Chuang, *"Photoelectron Microscopy Project at SRRC"*,   Surface Review and Letters **10(4)** 617-624 (2003).

[19] http://www.xradia.com

[20] W. Yun, B. Lai, Z. Cai, J. Maser, D. Legnini, and E. Gluskin, "Nanometer focusing of hard x rays by phase zone plates", Review of Scientific Instruments **70**, 2238,(1999).

[21]G. Schmahl, D. Rudolph, B. Niemann, O. Christ, Q. "Zone-plate X-ray microscopy", Rev. Biophys. **13**, 297. (1980).

[22] Janos Kirz *"Phase zone plates for xrays and the extreme uv"*, JOSA. **64**,301(1985).

[23] E. Di Fabrizio, F. Romanato, M. Gentili, S Cabrini, B. Kaulich, J. Susini, R. Barrett *"High-efficiency multilevel zone plates for keV X-rays"*, *Nature* **401**, 895.(1999).

[24] A. Snigirev V. Kohn I. Snigireva & B. Lengeler, *"A compound refractive lens for focusing high-energy X-rays"*, Nature **384**, 49 (1996).

[25] M. Awaji, Y. Suzuki, A. Takeuchi, H. Takano, N. Kamijo, S. Tamura and M. Yasumoto, *"Zernike-type X-ray imaging microscopy at 25 keV with Fresnel zone plate optics"* J. Synchrotron Rad. **9**, 125-127(2002).

[26] C. G. Schroer, J. Meyer, M. Kuhlmann, B. Benner, T. F. Günzler, B. Lengeler, C. Rau, T. Weitkamp, A. Snigirev, and I. Snigireva. *"Nanotomography based on hard x-ray microscopy with refractive lenses"* Appl. Phys. Lett. **81**, 1527 (2002).

[27] Yan Feng, Michael Feser, Alan Lyon, Steve Rishton, Xianghui Zeng, Sharon Chen,Simone Sassolini, and Wenbing Yun *"Nanofabrication of high aspect ratio 24 nm x-ray zone plates for x-ray imaging applications"*, J. Vac. Sci. Techonl. B **25**,2004(2007).

[28] B. Lengeler, C. G. Schroer, M. Richwin, and J. Tummler, M. Drakopoulos, A. Snigirev, and I. Snigireva, *"A microscope for hard x rays based on parabolic*

compound refractive lenses", Appl. Phys. Lett.**74**,3924,(1999).

[29] Janos Kirz and Harvey Rarback, *"Soft x-ray microscopes"*, Rev. Sci. Instrum, **56**,1(1985).

Chapter 2.

[1] David Attwood, *"Nanotomography comes of age"*, Nature, **442**,642(2006).

[2] Y. F. Song, C. H. Chang, C.Y. Liu, L. J. Huang, S. H. Chang, J. M. Chuang, S. C. Chung, P. C. Tseng, J. F. Lee, K. L. Tsang, and K. S. Liang, X-ray Beamlines on a Superconducting Wavelength Shifter, *SRI2003 proceedings.*

[3] Weilun Chao, Bruce D. Harteneck, J. Alexander Liddle, Erik H. Anderson and David T. Attwood, *"Soft X-ray microscopy at a spatial resolution better than 15nm"*, Nature,**435**, 1210-1213 (2005).

[4] C. J. Buckley. *"The Fabrication of Gold Zone Plates and their use in Scanning X-ray Microscopy"*. PhD thesis, Department of Physics, King's College, London, (1987).

[5] G. C. Yin, M. T. Tang, Y. F. Song, F. R. Chen, K. S. Liang, F. W. Duewer, W. Yun, C. H. Ko, and H. P. D. Shieh , *"Energy-tunable Transmission X-ray Microscope for Differential Contrast Imaging with Near 60 nm Resolution Tomography"*, Appl. Phys. Lett. **88** , 241115 (2006).

[6] http://www.xradia.com

[7] B. Murphy, D. L. White, Alastair A. MacDowell, and Obert R. Wood, *"Synchrotron radiation sources and condensers for projection x-ray lithography"*, Appl.Opti. 32(34), 6920 (1993).

[8] D.H. Bilderback, D. J. Thiel, R. Pahl and K. E. Brister, *"X-ray Applications with Glass-Capillary Optics"*, J. Synchrotron Rad.**1**, 37(1994).

[9] David Attwood. "*Soft x-rays and ultraviolet radiation: principles and applications.*"Cambridge University Press, first edition, 2000.

[10] A. Takeuchi, Y. Suzuki and H. Takano, *"Characterization of a Fresnel zone plate using higher-order diffraction"*,J. Sync. Rad,**9**,115(2002).

[11] Yan Feng, Michael Feser, Alan Lyon, Steve Rishton, Xianghui Zeng, Sharon Chen,Simone Sassolini, and Wenbing Yun *"Nanofabrication of high aspect ratio 24 nm x-ray zone plates for x-ray imaging applications"*, J. Vac. Sci. Techonl. B **25**,2004(2007).

[12] Y. Suzuki, A. Takeuchi, H. Takano and H. Takenaka, *"Performance Test of Fresnel Zone Plate with 50nm Outermost Zone Width in Hard X-ray Region"*, J.Jour. of Appl.Phys.**44**,(1994).

[13] Gerd Schneider, *"Cryo X-ray microscopy with high spatial resolution in*

amplitude and phase contrast", ultramicroscopy, 75, 85-104 (1998)

[14] http:// www-cxro.lib.gov, Center of X-ray optics.

[15] C. Jacobsen, S. Williams, E. Anderson **,** M.T. Browne , C.J. Buckley , D. Kern, J. Kirz, M. Rivers and X. Zhang, Optic. Comm., **86**, 351(1991).

[16] H. N. Chapman, C. Jacobsen, S. Willams. *"A characterization of dark-field imaging of colloidal gold labels in scanning transmission X-ray mircoscope"*, Ultramicroscopy **62**,191. (1996).

[17] S.Vogt, .H.N Chapman, C. Jacobsen, R. Medenwaldt,*" Dark field X-ray microscopy: the effects of condenser/dector aperture"*, Ultramicroscopy **87**,25. (2001).

[18] G. Hounsfield, *"A method of an apparatus for examination of a body by radiation such as x-ray or gamma radiation,"* Patent specifcation 1283915, The Patent Office (1972).

[19] G Di Chiro and RA Brooks," *The 1979 Nobel prize in physiology or medicine*," Science, **206**,1060 (1979).

[20] J. Radon, "*Uber due bestimmung von funktionen durch ihre intergralwerte langsgewisser mannigfaltigkeiten (on the determination of functions from their integrals along certain manifolds,"* Berichte Saechsische Akademie der Wissenschaften, **29**, 262 (1917).

[21] R.H. Bracewell and A.C. Riddle, "Inversion of fan beam scans in radio astronomy,"Astrophysics Journal, **150**, 427 (1967).

[22] http://www.sv.vt.edu/xray_ct/parallel/Ref.html

[23] A.C. Kak and M. Slaney, Principles of Computerized Tomographic Imaging. IEEE,Inc., New York: IEEE Press, (1988).

[24] H.H. Barrett and W. Swindell, Radialogical Imaging: The Theory of Image Formation,Detection and Processing. New York: Academic Press,(1981).

[25]G.N. Ramanchandran and A.V. Lakshminarayanan, *"Three dimensional reconstruc-tions from radiographs and electron micrographs: Application of convolution instead of fourier transforms,"* Proceedings of the National Academy of Sciences, **68**, 2236 (1971).

[26] A.V. Lakshminarayanan, *"Reconstruction from divergent ray data,"* tech. rep., Dept.Computer Science, State University of New York at Buffalo, (1975).

[27] Jun-Yuan Chen, David J. Bottjer, Eric H. Davidson, Stephen Q. Dornbos, Xiang Gao, Yong-Hua Yang, Chia-Wei Li, Gang Li, Xiu-Qiang Wang, Ding-Chang Xian,Hung-Jen Wu, Yeu-Kuang Hwu, Paul Tafforeau *"Phosphatized Polar Lobe-Forming Embryos from the Precambrian of Southwest China".* Science 312 (5780), 1644-1646,(2006).

[28] Gonzalez R C and Woods R E, Digital Image Processing , **109** (Addison-Wesley)

(1992).

[29] C.D Kuglin and D. C. Hines *"The phase correlation image alignment method"*. In proceedings of IEEE International Conference on Cybernetics and Society, **163**.(1975).

Chapter 3.

[1] A. Barty, K. A. Nugent, D. Paganin, and A. Roberts, "*Quantitative optical phase microscopy"*, Opt. Lett. **23**, 817 (1998).

[2] K. A. Nugent, T. E. Gureyev, D. F. Cookson, D. Paganin, and Z. Barnea, *"Quantitative Phase Imaging Using Hard X Rays"* Phys. Rev. Lett. **77**, 2961 (1996).

[3] L.J. Allen, W. McBride, N.L. O'Leary, M.P. Oxley, *"Exit wave reconstruction at atomic resolution"*, ultramicroscopy **100**, 91 (2004).

[4] W. Hsieh, F. Chen, J. Kai, A.I. Kirkland, *"Resolution extension and exit wave reconstruction in complex HREM"* Ultramicroscopy **98**, 99 (2004).

[5] G. C. Yin, M. T. Tang, Y. F. Song, F. R. Chen, K. S. Liang, F. W. Duewer, W. Yun, C. H. Ko, and H. P. D. Shieh , *"Energy-tunable Transmission X-ray Microscope for Differential Contrast Imaging with Near 60 nm Resolution Tomography"*, Appl. Phys. Lett. **88** , 241115 (2006).

[6] G.-C. Yin, Y.-F. Song, M.-T. Tang, F.-R. Chen, K. S. Liang, F. W. Duewer, M. Feser, W. Yun, and H.-P. D. Shieh, *"30 nm Resolution X-ray Imaging at 8 keV Using Third Order Diffraction of a Zone Plate Lens Objective in a Transmission Microscope"* Appl. Phys. Lett. **89** , 221122 (2006).

[7] G.-C. Yin, F.-R. Chen, Y. K. Hwu, H.-P. D. Shieh, and K. S. Liang, "*Quantitative Phase Retrieval in Transmission Hard X-ray Microscope*" , Appl. Phys. Lett. **90** , 181118 (2007).

[8] Michael Reed Teague, *"Deterministic phase retrieval: a Green's function solution"* J. Opt. Soc. Am. **73**,1434 (1983).

[9] D. Paganin and K. A. Nugent, *"Noninterferometric Phase Imaging with Partially Coherent Light"*, Phys. Rev. Lett. **80**, 2586(1998).

[10] Jun-Yuan Chen, David J. Bottjer, Eric H. Davidson, Stephen Q. Dornbos, Xiang Gao, Yong-Hua Yang, Chia-Wei Li, Gang Li, Xiu-Qiang Wang, Ding-Chang Xian,Hung-Jen Wu, Yeu-Kuang Hwu, Paul Tafforeau *"Phosphatized Polar Lobe-Forming Embryos from the Precambrian of Southwest China"*. Science 312 (5780), 1644-1646,(2006).

[11] B.D. Arhatari, A. P. Mancuso, A. G. Peele, and K. A. Nugent, *"Phase contrast radiography: Image modeling and optimization"*, Rev. Sci. Inst.,**75**,5271(2004).

[12] R. W. Gerchberg and W. O. Saxton. Optik, **35**, 237(1972).

[13] T. E. Gureyev, A. Roberts, and K. A. Nugent, *"Partially coherent fields, the transport-of-intensity equation, and phase uniqueness"*, J. Opt. Soc. Am. **12**,1942 (1995)

[14] M. R. Teague, *"Deterministic phase retrieval: a Green's function solution"* J. Opt. Soc. Am. **73**, 1434 (1983).

[15] K. A. Nugent, T. E. Gureyev, D. F. Cookson, D. Paganin, and Z. Barnea, *"Quantitative Phase Imaging Using Hard X Rays"* Phys. Rev. Lett. **77**, 2961

[16] A.V. Martin, F.-R. Chen, W.-K. Hsieh, J.-J. Kai, S.D. Findlay, L.J. Allen, *"Spatial incoherence in phase retrieval based on focus variation"*, ultramicroscope,**106**,914(2006).

[17] M. Born and E. Wolf. *"Principles of Optics"*. Pergamon Press, Oxford, sixth edition, (1980).

Chapter 4.

[1] F. Zernike, *"How I discovered phase contrast"*, Science **121,** 345–349 (1955).

[2] M. Born and E. Wolf. *"Principles of Optics"*. Pergamon Press, Oxford, sixth edition, (1980).

[3] H. B. Henning, *"A new scheme for viewing phase contrast images,"* Electro-Opt. Syst. Des. **6**, 30 (1974).

[4] J. Gluckstad, *"Phase contrast image synthesis,"* Opt. Commun.**130**, 225 (1996).

[5] S. F. Paul, *"Dark-ground illumination as a quantitative diagnostic for plasma density,"* Appl. Opt. **21,** 2531 (1982).

[6] C. S. Anderson, *"Fringe visibility, irradiance, and accuracy in common path interferometers for visualization of phase disturbances"* Appl. Opti. **34**,7474.(1995).

[7] J. Gluckstad and P. C. Mogensen, *"Optimal phase contrast in common-path interferometry"* Appl. Opti,**40**, 268 (2001).

[8] K. A. Nugent, T. E. Gureyev, D. F. Cookson, D. Paganin, and Z. Barnea, *"Quantitative Phase Imaging Using Hard X Rays"* Phys. Rev. Lett. **77**, 2961 (1996).

[9] G. C. Yin, M. T. Tang, Y. F. Song, F. R. Chen, K. S. Liang, F. W. Duewer, W. Yun, C. H. Ko, and H. P. D. Shieh , *"Energy-tunable Transmission X-ray Microscope for Differential Contrast Imaging with Near 60 nm Resolution Tomography"*, Appl. Phys. Lett. **88** , 241115 (2006).

[10] P. Cloetens, W. Ludwig, J. Baruchel, D. Van Dyck, J. Van Landuyt, J. P.Guigay, and M. Schlenker,*"Holotomography: Quantitative phase tomography with*

Micrometer resolution using hard synchrotron radiation x rays" Appl. Phys. Lett. **75**, 2912- 2914 (1999).

[11] P. J. McMahon, A. G. Peele, D. Paterson, and K. A. Nugent A. Snigirev, T. Weitkamp, and C. Rau, *"X-ray tomographic imaging of the complex refractive index"* Appl. Phys. Lett. **83**,1480 (2003).

[12] F. Pfeiffer, C. Kottler, O. Bunk, and C. David, *"Hard X-Ray Phase Tomography with Low-Brilliance Sources"*, Phys. Rev. Lett., **98**,108105 (2007).

[13] A. V. Bronnikov, *"Theory of quantitative phase-contrast computed tomography"* J. Opt. Soc. Am. A, **19**, 472 (2002).